# Magnetization Transfer Imaging Using Steady-State Free Precession MR Sequences

von

Monika Gloor
aus Birrwil AG

Basel, 2010

Genehmigt von der Philosophisch-Naturwissenschaftlichen Fakultät
auf Antrag von

Dr. Oliver Bieri
    *Experte*
Prof. Dr. Klaus Scheffler
    *Dissertationsleiter*
PD Dr. Stefan Ropele
    *Korreferent*

Basel, den 21. September 2010

Prof. Dr. Martin Spiess
*Dekan*

# Abstract

Magnetic resonance imaging (MRI) benefits from an exceptional soft tissue contrast and is therefore an important tool for medical diagnosis. While contrast in conventional MRI is generated by protons with free mobility, magnetization transfer (MT) imaging generates contrast from protons bound to macromolecules. This contrast is based on tissue microstructure and tissue integrity. Additional information about tissue changes is desirable for better understanding, for early diagnosis, and for monitoring treatment response of many pathologies. However, most MT imaging techniques are still not suitable for application in the daily clinical routine due to long acquisition times. In contrast, steady-state free precession (SSFP) sequences offer short acquisition times and high signal-to-noise ratios (SNR) in combination with their inherent MT-sensitivity. In this thesis, new MT imaging methods are developed using SSFP sequences.

In Chapter 2, a quantitative MT imaging technique is implemented based on balanced SSFP (bSSFP). The derived analytical solution is used to determine quantitative MT parameters, such as the bound proton fraction $F$ and the forward exchange rate $k_f$ as well as the relaxation times in human brain. In Chapter 3, a protocol is introduced that benefits from an even shorter acquisition time and from the possibility to incorporate phase-cycled acquisitions to reduce banding artifacts. In the second part of this chapter, the effect of finite RF pulses is accounted for by a modification to the two-pool bSSFP signal equation.

While bSSFP techniques are well applicable in targets with low susceptibility variations such as the human brain, targets of the musculoskeletal system, such as cartilage and muscle cause signal loss from off-resonance effects. As a result, in Chapter 4, the proposed qMT imaging principle is adapted to nonbalanced SSFP. Quantitative MT parameters are derived from human femoral muscle and human patellar cartilage. In addition to quantitative MT imaging, bSSFP-based magnetization transfer ratio (MTR) measurements are performed in significantly shorter times and with an improved SNR compared to conventional methods. In Chapter 5, the reproducibility of bSSFP-MTR is analyzed in brain tissue of healthy subjects. In order to establish bSSFP-based qMT imaging in a clinical setting, a reference data set of normal appearing brain structures is analyzed in Chapter 6. First experiences of the new qMT technique in imaging of tumor and ischemia patients are presented.

# Publications Arising from this Thesis

## Jounal Papers

- **M. Gloor**, K. Scheffler, O. Bieri. Quantitative Magnetization Transfer Imaging Using Balanced SSFP. *Magn Reson Med*, 60(3):691-700, 2008.

- **M. Gloor**, K. Scheffler, O. Bieri. Nonbalanced SSFP-Based Quantitative Magnetization Transfer Imaging. *Magn Reson Med*, 64(1):149-156, 2010.

- **M. Gloor**, K. Scheffler, O. Bieri. Intra- and Inter-Scanner Variability of MT-Sensitized Balanced Steady-State Free Precession. *Magn Reson Med*, submitted.

- **M. Gloor**, S. Fasler, A. Fischmann, T. Haas, O. Bieri, K. Heinimann, S. Wetzel, K. Scheffler, D. Fischer. Quantification of Fat Infiltration in Oculopharyngeal Muscular Dystrophy: Comparison of Three MR Imaging Methods. *J Magn Reson Imaging*, submitted.

- M. Garcia, **M. Gloor**, S.G. Wetzel, E.W. Radue, K. Scheffler, O. Bieri. Characterization of normal appearing brain structures using high-resolution quantitative magnetization transfer steady-state free precession imaging. *Neuroimage*, 52:532-537, 2010.

- H.J.A. Crooijmans, **M. Gloor**, O. Bieri and K. Scheffler. Influence of MT effects on T2 quantification with 3D balanced steady-state free precession imaging. *Magn Reson Med*, in press.

- M. Garcia, **M. Gloor**, O. Bieri, S.G. Wetzel, E.W. Radue, K. Scheffler. MTR variations in normal adult brain structures using balanced steady-state free precession. *Neuroradiology*, in press.

- A. Fischmann, **M. Gloor**, S. Fasler, T. Haas, O. Bieri, S. Wetzel, K. Heinimann, K. Scheffler, D. Fischer. Muscular involvement assessed by MRI correlates to motor function measurement values in oculopharyngeal muscular dystrophy. *Neuromuscular Disorders*, submitted.

## Conference Abstracts

- **M. Gloor**, K. Scheffler, O. Bieri. Quantitative Magnetization Transfer Imaging Using Balanced SSFP. Proceedings of the 16th Annual Meeting ISMRM, Toronto, 2008, Talk.

- **M. Gloor**, K. Scheffler, O. Bieri. Quantitative Magnetization Transfer Imaging of the Brain within 10 Minutes. ISMRM White Matter Workshop, Krakow, 2008, Talk.

- **M. Gloor**, K. Scheffler, O. Bieri. Accelerated Quantitative Magnetization Transfer Imaging Using Balanced SSFP. Proceedings of the 25th Annual Meeting ESMRMB, Valencia, 2008, Talk.

- **M. Gloor**, O. Bieri, C. Mamisch, G. Welsch, S. Trattnig, K. Scheffler. Quantitative Magnetization Transfer SSFP Cartilage Imaging. ISMRM Musculoskeletal Workshop, San Francisco, 2009, Talk.

- **M. Gloor**, K. Scheffler, O. Bieri. Quantitative Magnetization Transfer Imaging Using Non-Balanced SSFP. Proceedings of the 17th Annual Meeting ISMRM, Honolulu, 2009, E-Poster (1st Place Poster in Physics and Pulse Sequences).

- **M. Gloor**, K. Scheffler, O. Bieri. Intra- and Inter-Scanner Variability of Magnetization Transfer Ratio Using Balanced SSFP. Proceedings of the 17th Annual Meeting ISMRM, Honolulu, 2009, E-Poster.

- **M. Gloor**, K. Scheffler, O. Bieri. Quantitative Magnetization Transfer Imaging Using Balanced SSFP. CEST Workshop, Torino, 2010, Talk.

- **M. Gloor**, A. Fischmann, S. Fasler, T. Haas, O. Bieri, K. Scheffler, D. Fischer. Quantification of Fat Infiltration in Thigh and Calf Muscles in Oculopharyngeal Muscular Dystrophy: Comparison of Three MRI Methods. Proceedings of the Joint Annual Meeting ISMRM-ESMRMB, Stockholm, 2010, Talk.

- **M. Gloor**, K. Scheffler, O. Bieri. Finite RF Pulse Effects on Quantitative Magnetization Transfer Imaging Using Balanced SSFP. Proceedings of the Joint Annual Meeting ISMRM-ESMRMB, Stockholm, 2010, E-Poster.

- D. Fischer, K. Scheffler, K. Heinimann, M. Tolnay, R. Rodoni, A. Fischmann, **M. Gloor**. Evaluation of In-Phase and Out-Of-Phase and FISP MRI to Quantify Muscle Fat Content in OPMD. Proceedings of the 14th International Congress WMS, Geneva, 2009.

- M. Garcia, **M. Gloor**, S. G. Wetzel, F. Jax, E.-W. Radue, K. Scheffler, O. Bieri. Is MTR a Reliable Parameter for the Assessment of Myelination in the Brain? Analysis of MTR Regarding QMT Parameters with High Resolution BSSFP Imaging. Proceedings of the 34th Annual Meeting ESNR, Athens, 2009.

- F. Jax, O. Bieri, **M. Gloor**, G. Sommer, K. Scheffler, E.-W. Radue, S. G. Wetzel. Advanced Imaging of Acute and Subacute Stroke by Magnatization Transfer Ratio Applying a BSSFP-Protocol. Proceedings of the 34th Annual Meeting ESNR, Athens, 2009.

- M. Garcia, **M. Gloor**, C. Stippich, F. Jax, K. Scheffler, O. Bieri. Analysis of Brain Tumors and Metastases by Quantitative MT Imaging with BSSFP: Initial Experiences. Proceedings of the Joint Annual Meeting ISMRM-ESMRMB, Stockholm, 2010.

- F. Jax, **M. Gloor**, O. Bieri, M. Garcia, S. Engelter, F. Fluri, K. Scheffler, E.-W. Radue, S. G. Wetzel. Quantitative Magnetization Transfer Imaging in Acute Stroke: A Follow Up Study Correlating Quantitative MRI with Respect of Severity of Stroke. Proceedings of the Joint Annual Meeting ISMRM-ESMRMB, Stockholm, 2010.

- M. Soellinger, C. Langkammer, T. Seifert-Held, N. Krebs, **M. Gloor**, E. Scheurer, K. Scheffler, F. Fazekas, S. Ropele. Quantitative Magnetization Transfer Imaging in Postmortem Brain at 3T Using BSSFP. Proceedings of the Joint Annual Meeting ISMRM-ESMRMB, Stockholm, 2010.

- M. Garcia, **M. Gloor**, O. Bieri, F. Jax, K. Scheffler, C. Stippich. Analysis of brain tumors and metastases by quantitative MT imaging with bSSFP: Initial experiences. Proceedings of 48th Annual Meeting ASNR, Boston, 2010.

# Contents

# Chapter 1

# Introduction

## 1.1   Introduction to Magnetization Transfer

In conventional magnetic resonance imaging (MRI), tissue contrast is generated from variations in proton density and relaxation times of water protons. Longitudinal and transverse components of the magnetization in homogeneous samples relax monoexponentially with characteristic decay times $T_1$ and $T_2$. In biological tissues, however, there are protons with free mobility (water protons) and protons with restricted mobility due to bonds to macromolecules or membranes. These restricted protons have a $T_2$ relaxation time that is too fast to allow their detection by conventional proton MRI techniques.

Magnetization transfer (MT) imaging generates tissue contrast depending on the magnetization exchange between free and restricted protons. Exchange between spin systems in different chemical environments has been known since the 1950s [1–5]. The term magnetization transfer was introduced by Wolff and Balaban in 1989 to describe the exchange rate in kidney and skeletal muscle in vivo [6]. Magnetization transfer imaging thus offers a characterization of the macromolecular protons invisible in standard MRI. Besides improving the contrast, magnetization transfer provides quantitative information about tissue structure and pathological changes beyond conventional $T_1$, $T_2$ and $T_2^*$ contrast [6]. For this reason, MT methods add specificity to diagnostic imaging.
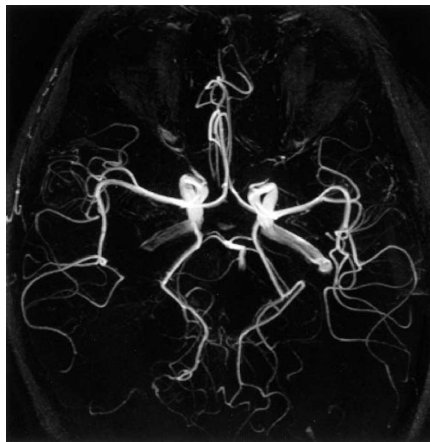


Figure 1.1: MR angiogram with MT suppression at 3 T. Brain tissue is suppressed by 7-16 % across the image, while flowing blood gives full signal [7].

In a clinical setting, MT imaging is predominantly used to suppress background signals from tissues in MR angiography. While restricted protons are selectively saturated, the signal from flowing blood is unaffected, leading to superior angiogram quality (Fig. 1.1) [8]. Another main application of magnetization transfer is in the field of demyelinating diseases. Restricted protons in brain white matter are largely associated with myelin. Hence, demyelination in multiple sclerosis (MS) becomes visible in terms of a reduced MT effect in lesions [9].

## 1.2    Molecular Mechanism of Magnetization Transfer

The basis of magnetization transfer is the interaction between free water protons and macromolecular protons. In addition to these two proton populations, exchangeable protons in a solvation layer around the macromolecule play an important role in the transfer process [10–12]. Two different pathways of magnetization exchange between macromolecules and water have been proposed (Fig. 1.2):

1. In the first pathway, magnetization is transferred between nonexchangeable protons and exchangeable protons of hydroxyl (OH) or amine (NH) groups of the macromolecular phase by magnetic dipole-dipole interactions (also known as Nuclear Overhauser Effect (NOE)). The intermediate protons exchange rapidly with the bulk water.

2. In the second pathway, nonexchangeable protons interact with hydration layer water molecules, which exchange rapidly with the bulk water.
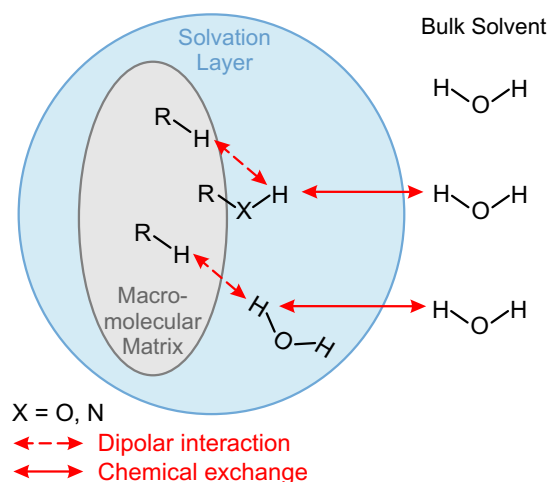


Figure 1.2: Molecular model for magnetization transfer. In the first pathway, magnetization is transferred via exchangeable protons of hydroxyl or amine groups. In the second pathway, MT is mediated by hydration layer molecules [11, 12].

Magnetization transfer between lipid membrane models and water has been shown to depend on the presence of sites with exchangeable hydroxyl and amino protons [13]. Also, for small globular proteins and DNA molecules the predominant MT pathway was found to be via exchangeable protons, especially those of hydroxyl and amine groups [11]. These protons have exchange rates that are sufficiently fast for not being rate limiting for the overall magnetization transfer, and sufficiently slow for optimum dipolar interaction with the nonexchangeable protons. On the other hand, hydration water is less effective in transferring magnetization via dipolar interactions [11].

It is known that the magnetization transfer effect is more pronounced in brain white matter than in gray matter [14]. This was attributed to the higher content

of myelin-bound cholesterol, which contains OH and NH groups [15]. All these results suggest that exchangeable protons play a dominant role for magnetization transfer. This is of particular importance for the interpretation of clinical MT studies of demyelinating diseases.

### 1.2.1   Chemical Exchange Saturation Transfer

While MT contrast is based on magnetization exchange between cellular solid or semisolid protons and water protons, chemical exchange saturation transfer (CEST) contrast originates from chemical exchange between labile protons and water protons. Small molecules in solution are saturated by selective RF irradiation. The saturation is transferred to the water pool via labile protons of the solute (e. g. hydroxyl, amine, amide, or imino protons), as first demonstrated by Wolff and Balaban in 1990 [16–18]. Saturated solute protons are repeatedly re-
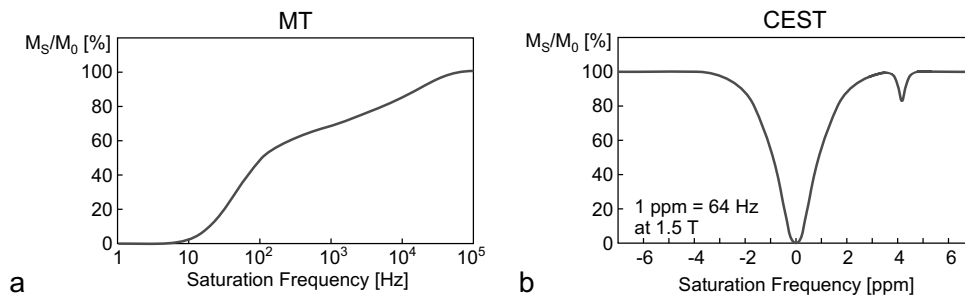


Figure 1.3: Typical spectra (also known as Z-spectra) for MT and CEST. (a) The MT spectrum is broad and symmetric with respect to the water resonance. (b) The CEST effect appears at a very narrow frequency range and asymmetrically around the water resonance.

placed by non-saturated water protons, leading to an accumulation of saturated protons in the water pool. After a few seconds of RF irradiation, this gives rise to an observable signal reduction in the water pool. Highest sensitivity to proton transfer is achieved if the exchange rate from solute to water $k_{sw}$ is large and the solute has a high concentration. The chemical exchange rate is of great physiological interest, as it depends on the pH and the molecular environment, such as salt and metal content [19].

Chemical exchange, in addition to dipolar magnetization exchange, contributes significantly to MT contrast. An MT spectrum, Z-spectrum [20], or CEST spectrum [18] displays RF saturation effects on water as a function of saturation frequency offset relative to water, which is assigned to be at 0 ppm. Magnetization transfer can be detected over a large frequency range of about ±100 kHz (Fig. 1.3 a) [6, 21]. In contrast, CEST is usually observed in a small chemical shift range of less than 5 ppm from water (Fig. 1.3 b), but may also be registered at several 100 ppm depending on the type of CEST agent. The different types of CEST agents can be grouped into paramagnetic CEST (PARACEST) [22, 23] and diamagnetic CEST (DIACEST) agents. Furthermore, it is possible to detect endogenous mobile proteins and peptides in biological tissue via chemical

exchange, an approach that is known as amide proton transfer (APT) imaging [24, 25]. Another research direction is CEST on polymers [26, 27].

## 1.3 Quantitative Description of Magnetization Transfer

### 1.3.1 Two-Pool Model

The signal of restricted protons in tissue decays too fast ($T_{2,r} \approx 10\,\mu\text{s}$) to be detected by conventional proton MRI. However, exchange processes between the restricted and free protons allow an indirect observation. As displayed in Fig. 1.4,
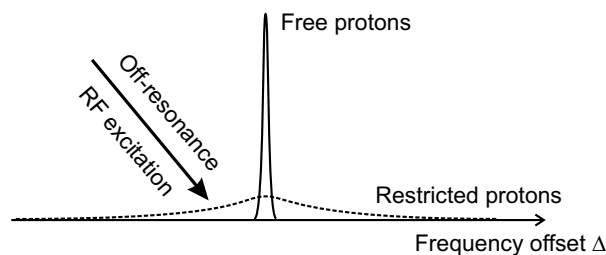


Figure 1.4: The macromolecular protons exhibit a broader absorption lineshape than the free protons and can be selectively saturated using an off-resonance RF pulse.

the macromolecular spins exhibit a broader absorption lineshape than the liquid spins. Therefore, it is possible to selectively saturate the macromolecular spins without affecting free protons, e.g. with an off-resonance radio frequency (RF) pulse [9]. The saturation of macromolecular spins is then transferred to the liquid spins in the free water environment and yields a signal attenuation that is visible with MRI.

A simple model to analyze magnetization transfer experiments is shown in Fig. 1.5 [28]. The model consists of two pools, a pool of free water protons ($f$) and a pool of protons restricted in motion ($r$). Each pool is divided into a fraction of longitudinal magnetization (unshaded) and a fraction of other magnetization (shaded). The equilibrium magnetization of the free pool $M_{0,f}$ is normalized to 1, and the equilibrium magnetization of the restricted pool is given by $M_{0,r}$. Longitudinal relaxation is characterized by the relaxation rates $R_{1,f} = 1/T_{1,f}$ and $R_{1,r} = 1/T_{1,r}$, whereas the rate of loss of longitudinal magnetization is governed by $R_{RF,f}$ and $R_{RF,r}$. The magnetization exchange between the two pools is characterized by the rate constant $R$. To describe directional exchange, pseudo-first order rate constants $k_f = RM_{0,r}$ (exchange $f \rightarrow r$) and $k_r = RM_{0,f}$ (exchange $r \rightarrow f$) are used.

### 1.3.2 Coupled Bloch Equations

The Bloch equations with exchange for a coupled two-pool system have been first presented by McConnell in 1958 [29] and further analyzed by Forsén and Hoffman
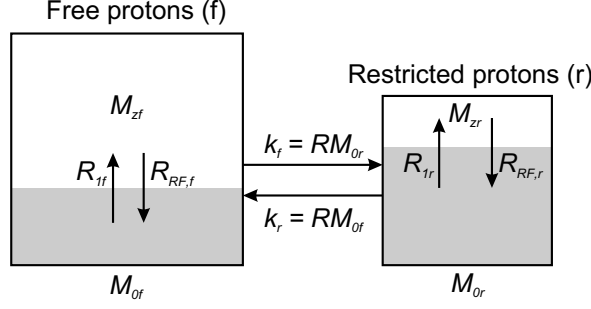
Figure 1.5: Two-pool model of magnetization transfer [28]. The shaded area represents saturated spins. Variables are defined in the text.

[3], Edzes and Samulski [5], Wu [30] and Henkelman et al. [28]. In a general form, they can be written as follows:

$$\frac{dM_{x,f}}{dt} = -\frac{M_{x,f}}{T_{2,f}} - k_f M_{x,f} + k_r M_{x,r} + 2\pi \Delta M_{y,f}, \tag{1.1a}$$

$$\frac{dM_{y,f}}{dt} = -\frac{M_{y,f}}{T_{2,f}} - k_f M_{y,f} + k_r M_{y,r} - 2\pi \Delta M_{x,f} + \omega_1(t) M_{z,f}, \tag{1.1b}$$

$$\frac{dM_{z,f}}{dt} = R_{1,f}(M_{0,f} - M_{z,f}) - k_f M_{z,f} + k_r M_{z,r} - \omega_1(t) M_{y,f}, \tag{1.1c}$$

$$\frac{dM_{x,r}}{dt} = -\frac{M_{x,r}}{T_{2,r}} - k_r M_{x,r} + k_f M_{x,f} - 2\pi \Delta M_{y,r}, \tag{1.1d}$$

$$\frac{dM_{y,r}}{dt} = -\frac{M_{y,r}}{T_{2,r}} - k_r M_{y,r} + k_f M_{y,f} - 2\pi \Delta M_{x,r} + \omega_1(t) M_{z,r}, \tag{1.1e}$$

$$\frac{dM_{z,r}}{dt} = R_{1,r}(M_{0,r} - M_{z,r}) - k_r M_{z,r} + k_f M_{z,f} - \omega_1(t) M_{y,r}, \tag{1.1f}$$

where the subscripts $x$, $y$, $z$ denote the various spatial components of the magnetization vector $\mathbf{M}$, subscripts $f$ and $r$ denote free and restricted pool magnetization, $\omega_1(t) = \gamma |\mathbf{B}_1(t)|$ corresponds to the shape and $\Delta$ to the frequency offset of the RF pulse. Exchange between transverse magnetization components can be neglected, since any transverse coherence between the two pools will be destroyed due the very short $T_2$ of the macromolecular pool [5, 28]. In the steady state, all time derivatives are zero and Eqs. (1.1a)-(1.1f) can be rewritten as:

$$0 = -\frac{M_{x,(f,r)}}{T_{2,(f,r)}} + 2\pi \Delta M_{y,(f,r)}, \tag{1.2a}$$

$$0 = -\frac{M_{y,(f,r)}}{T_{2,(f,r)}} - 2\pi \Delta M_{x,(f,r)} + \omega_1(t) M_{z,(f,r)}, \tag{1.2b}$$

$$0 = R_{1,f}(M_{0,f} - M_{z,f}) - k_f M_{z,f} + k_r M_{z,r} - \omega_1(t) M_{y,f}, \tag{1.2c}$$

$$0 = R_{1,r}(M_{0,r} - M_{z,r}) - k_r M_{z,r} + k_f M_{z,f} - \omega_1(t) M_{y,r}. \tag{1.2d}$$

This simplified set of equations can be solved to yield an expression for the free pool magnetization $M_{z,f}$.

$$M_{z,f} = \frac{R_{1,f}R_{1,r} + k_r R_{1,f} + k_f R_{1,r} + R_{RF,r}R_{1,f}}{(R_{1,r} + k_r + R_{RF,r})(R_{1,f} + k_f + R_{RF,f}) - k_f k_r} \qquad (1.3)$$

Additionally, the equations describe the saturation of the free and restricted pools in terms of a Lorentzian absorption lineshape:

$$R_{RF,(f,r)} = \frac{\omega_1^2 T_{2,(f,r)}}{1 + \left(2\pi\Delta T_{2,(f,r)}\right)^2} \qquad (1.4)$$

However, a Lorentzian lineshape is not appropriate for the semisolid pool, and alternative lineshapes were proposed, such as a Gaussian [28], Super-Lorentzian [31], "Kubo-Tomita" [32], and flexible [32] lineshape. It has been found from continuous wave (CW) measurements in fresh bovine brain that a Super-Lorentzian lineshape fits the data best [31]:

$$R_{RF,r} = \int_0^1 \sqrt{\frac{2}{\pi}} \frac{T_{2,r}}{|3u^2 - 1|} \exp\left[-2\left(\frac{2\pi\Delta T_{2,r}}{3u^2 - 1}\right)^2\right] du \qquad (1.5)$$

Several approaches were made to derive MT parameters from the two-pool model. For the case of CW irradiation, complete saturation of the restricted pool is achieved, and Eq. (1.3) can be used to fit five model parameters: $R$, $R_{1,r}$, $T_{2,r}$, $RM_{0,r}/R_{1,f}$, and $1/(R_{1,f}T_{2,f})$ [31]. A measurement of the observed $R_{1obs}$ yields $R_{1,f}$. For the case of pulsed MT saturation, the two-pool equations has been solved with simplifying assumptions [33–36]. Other groups calculated a CW power equivalent for the pulsed irradiation [37, 38].

## 1.4 Magnetization Transfer Imaging Techniques

In all magnetization transfer experiments, the magnetization of the liquid pool is indirectly manipulated by saturating the macromolecular pool. By doing this, some direct saturation of free protons is unavoidable.

Off-resonance CW irradiation was first used to demonstrate MT effects in tissue [3, 6]. Typically, irradiation is applied with $0.5\,\mathrm{kHz}$ to $10\,\mathrm{kHz}$ off-resonance. Direct saturation is minimized by the narrow bandwidth of CW irradiation. On the other hand, these experiments are not feasible on clinical systems, since the RF transmitters are not designed for CW operation.

Pulsed irradiation of shorter duration can be applied either on-resonant or off-resonant. On-resonant saturation is achieved by binomial (or "transparent") pulses, such as $1\,\overline{1}$ or $1\,\overline{2}\,1$. These pulses have no net effect on the mobile protons, while the short $T_2$ spins are saturated [39, 40]. Despite their easy implementation and strong signal attenuation, the use of binomial pulses was not established due to their intrinsic large direct saturation [37].

Off-resonance RF pulses are most popular to perform MT imaging. They are usually Gaussian or sinc pulses with a bandwidth of a few 100 Hz at frequency

offsets between 50 Hz and 50 kHz from the free proton resonance frequency. The pulses are applied before each excitation. High energy deposition in tissue, as measured by the specific absorption rate (SAR), may be a problem.

### 1.4.1   Magnetization Transfer Ratio Imaging

The term magnetization transfer ratio (MTR) was introduced by Dousset et al. in 1992 [9]. It describes a way to quantify the amount of magnetization transfer. Two sets of images are acquired: one without saturation (signal $S_0$) and one with saturation (signal $S_{sat}$) of the macromolecular protons. The ratio of transfer is then calculated according to

$$\text{MTR} = \frac{S_0 - S_{sat}}{S_0}. \tag{1.6}$$

Dousset et al. produced the first clinical MTR images using a three-dimensional spoiled gradient echo (SPGR) sequence with a 2 kHz off-resonance pulse (Fig. 1.6 a) [9] and showed that MTR values can be used to assess demyelinating processes. A three-dimensional SPGR sequence with higher resolution was used by Finelli et
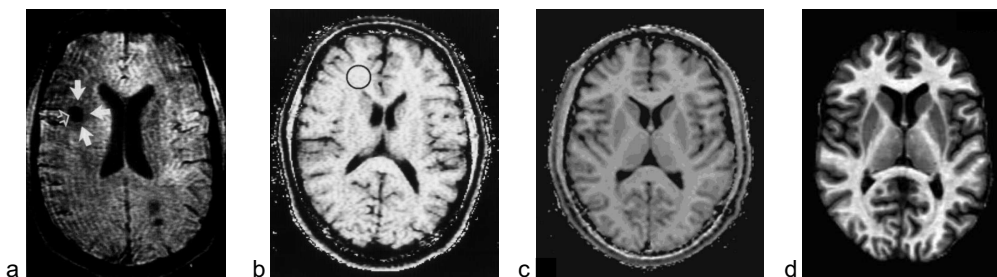


Figure 1.6: Exemplary magnetization transfer ratio (MTR) images at 1.5 T in chronological order (a)-(c). (a) The first MTR study on MS patients was presented by Dousset et al. in 1992 [9]. They proposed that MTR can be used to assess the extent of myelin loss. (b) An MTR image of the multicenter comparison published by Berry et al. in 1999 [41]. (c) MTR calculated from a $T_{1sat}$ map by Ropele et al. in 2000 [42]. (d) MT saturation map according to Helms et al. at 3 T [43] in 2008.

al. with a 4 kHz off-resonance pulse [44]. Other implementations of MTR imaging sequences were presented by Barker et al. and Berry et al. (Fig. 1.6 b) [41, 45]. They used interleaved dual spin echo and two-dimensional multislice gradient echo sequences for multicenter comparisons.

The MTR value at a fixed saturating power is proportional to the product $k_f T_{1sat}$, where $T_{1sat}$ denotes the apparent $T_1$ under full saturation of the macromolecular spins [3, 28], or proportional to the product $F T_{1obs}$, where $F$ denotes the fractional size of the bound proton pool and $T_{1obs}$ is the observed $T_1$ of the free protons, which includes exchange between the pools [46]. This means that the forward exchange constant $k_f$ can be obtained via measurement of the MTR and $T_{1sat}$. However, these relations only hold for full saturation of the bound

pool, a condition that is practically limited by safety regulations. Measurements have also been made using incomplete saturation [42, 47].

The main application of MTR imaging is in MS, where it has been widely utilized to describe lesions, normal-appearing white and gray matter abnormalities [48], and has revealed tissue changes that are invisible in conventional MRI. Furthermore, MTR has been applied on tumor [49, 50] and ischemia [51, 52] patients.

### 1.4.2   Quantitative Magnetization Transfer Imaging Using Continuous Wave Irradiation

Instead of performing only two measurements, one without and one with saturation of macromolecular protons for MTR calculation, a whole range of measurements at different frequency offsets $\Delta$ can be performed. These experiments did not only validate the two-pool model described above, but also represented the first quantitative magnetization transfer (qMT) imaging experiments in vitro and in vivo [28, 31, 53]. Figure 1.7 a displays representative MT data for human
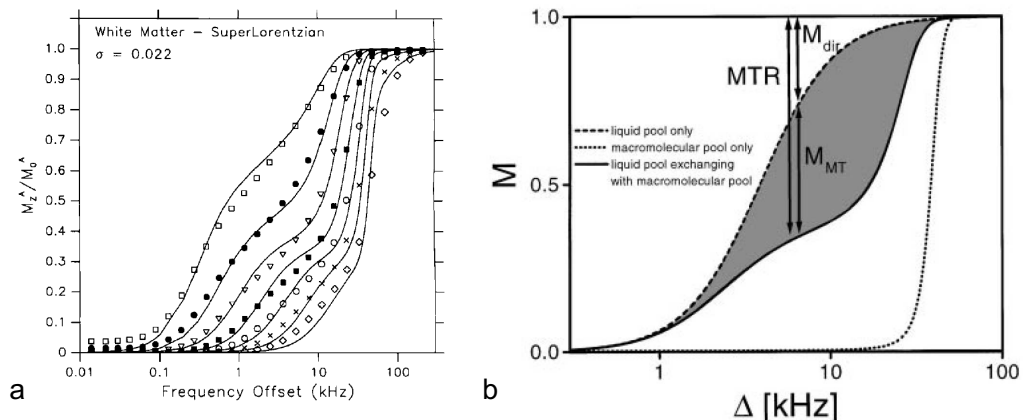


Figure 1.7: (a) Magnetization transfer data for human white matter are shown for 27 different offset frequencies $\Delta$ and for different RF amplitudes $\omega_1/2\pi = 83$, 170, 330, 670, 1340, 2670, and 5340 Hz. Solid lines represent a two-pool model fit with a Super-Lorentzian absorption lineshape [31]. (b) Longitudinal magnetization of the liquid and semisolid pool. The dashed line shows saturation due to the direct effect ($M_{dir}$), the dotted line saturation of the macromolecular pool only, and the solid line saturation of the liquid pool exchanging with the macromolecular pool. Saturation from magnetization transfer ($M_{MT}$) is given by the shaded area [7].

white matter, showing the fraction of longitudinal magnetization $M_{z,f}/M_{0,f}$ remaining after CW irradiation versus frequency offset $\Delta$ [31]. A two pool model fit to the data yields quantitative MT parameters as described in Section 1.3.2. Figure 1.7 b shows MT data for 4 % agar. Curves without and with exchange between the two pools are plotted.

### 1.4.3   Quantitative Magnetization Transfer Imaging Using Pulsed Irradiation

In 2001 and 2002, three different approaches for estimating qMT parameters based on pulsed RF irradiation were applied in vivo.

Sled and Pike described a model for pulsed MT sequences, where they introduced the transition rate $W$ for the saturation of the restricted protons [36]. For shaped MT pulses this transition rate can be approximated as

$$W(t) = \pi \omega_1^2(t) G(\Delta), \tag{1.7}$$

where $G$ denotes the lineshape function for the restricted pool and $\Delta$ the off-resonance irradiation frequency. With several approximations, a closed form expression for the signal from a pulsed MT experiment was derived [36] and restricted to spoiled gradient echo sequences [54].
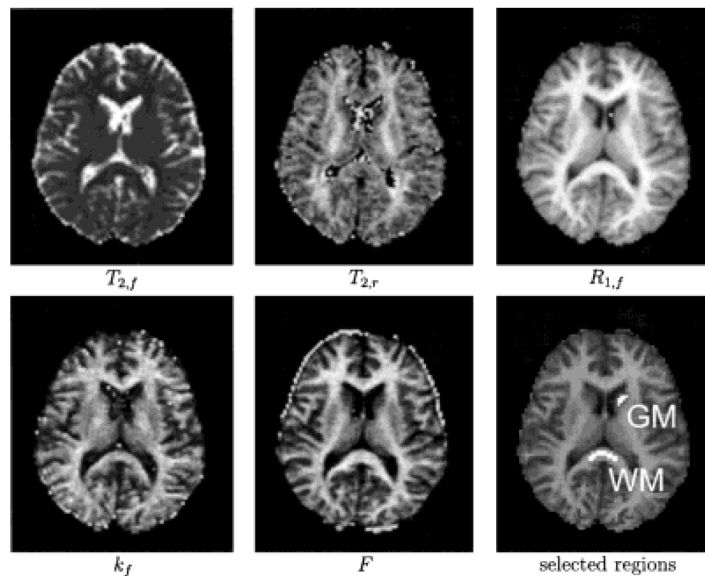


Figure 1.8: Quantitative magnetization transfer parameter images of a healthy volunteer derived from fitting a signal equation for pulsed MT experiments to a series of MT-weighted spoiled gradient echo sequences [54].

First, $T_{1,obs}$ and $T_{2,obs}$ were measured using a Look-Locker sequence [55], and a multi-echo spin echo sequence [56], respectively. Corrections for $B_0$ and $B_1$ inhomogeneity were made. Then five parameters were estimated from 60 data points with various offset frequencies and saturation power: the fractional size of the macromolecular pool $F = M_{0,r}/M_{0,f}$, the forward exchange rate $k_f = R M_{0,r}$, and the relaxation properties $R_{1,f}$, $T_{2,f}$, and $T_{2,r}$. Parameter images were given for two healthy volunteers (Fig. 1.8) and an MS patient. The acquisition time for a single 7 mm thick slice with 2 mm in-plane resolution was 35 min.

Yarnykh derived a solution of the two-pool model using a CW approximation during the MT pulse, assuming that the direct effect is negligible [57]. Separate

$T_{1,obs}$ images were obtained from the variable flip angle method [58]. Data points at nine different off-resonance frequencies were collected using an SPGR sequence and a two-parameter fit with fixed $T_{2,r} = 8.5\,\mu s$ yielded $f := M_{0,r}/(1 + M_{0,r})$ and $k := k_f$ maps. Images were acquired from two healthy subjects, two MS patients, and one tumor patient (Fig 1.9). About 40 min were required for the whole data collection with eight slices of 6 mm thickness and 1.7 mm in-plane resolution.
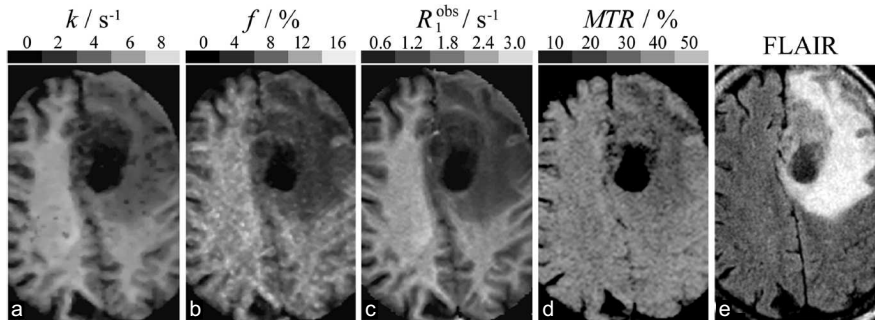


Figure 1.9: Quantitative magnetization transfer parameter images of a glioma patient [57].

Ramani et al. developed another model for pulsed MT using a CW power equivalent [38]. The CW power equivalent is defined as the root mean square value of the saturating field, averaged over the duty cycle of the MT pulse. Thus, the MT pulse is treated as having the same effect as a CW irradiation with the same average power. After independent $T_{1,obs}$ measurements, ten combinations of saturation power and offset frequency were chosen. The total scan time for one slice with a pixel size of $0.94 \times 1.88\,cm$ amounted to 34 min.

Three-dimensional acquisitions of qMT parameters were presented for the first time by Yarnykh et al., who achieved a $1.4 \times 2.3 \times 2.8$ resolution in about 30 min [59]. Compared to the previous formulation [57], direct saturation of the free pool was included. Based on the model of Ramani et al. [38], another 3D approach to fit five qMT parameters was published by Cercignani et al. [60]. Within a total imaging time of less than 20 minutes, a whole brain coverage of $1 \times 2 \times 5\,mm$ was obtained.

### 1.4.4   Other Magnetization Transfer Imaging Techniques

In 1978, Edzes and Samulski measured the recovery of longitudinal relaxation after a train of low power pulses, which disturbs either the free or the restricted pool protons [5]. Gochberg et al. used a similar principle based on the fact that the evolution to steady state after selective irradiation of the free pool runs much faster than $T_1$ relaxation [61]. They applied pulses that are temporally separated by more than $1/k_r$ and have durations shorter than $1/k_r$. A train of these pulses is used to selectively invert the magnetization of the free water protons. Subsequently, an analytic expression for the longitudinal magnetization of the free protons is fitted to the measured biexponential decay curve. The pool size ratio is calculated from the exchange rates according to $F = k_f/k_r$. Recently,

a modified inversion recovery sequence followed by echo planar or fast spin echo imaging has been used to efficiently map qMT parameters [62, 63]. Quantitative
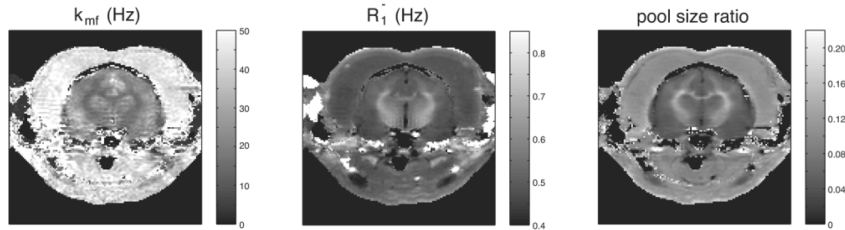


Figure 1.10: Quantitative magnetization transfer parameter images of a ferret brain at 9.4 T using selective inversion recovery [63]. Backward exchange rate $k_{mf} = k_r$ (left), relaxation rate of the free pool $R_1$ (middle) and pool size ratio $F$ (right).

parameter maps of a ferret brain at 9.4 T (Fig. 1.10) [63] and of frog skeletal muscle at 4.7 T [64] were derived using this method. In 2010, the approach was tested on healthy volunteers and an MS patient at 3 T, where a $2 \times 2 \times 5$ mm slice was acquired in 4 min [65].

Ropele et al. introduced a fast multislice $T_1$ and $T_{1sat}$ imaging technique using phase acquisition of composite echoes (PACE) [47, 66]. PACE stands for the simultaneous acquisition of a spin echo and a phase-shifted stimulated echo. The phase of such a composite echo is weighted purely by longitudinal relaxation. Therefore, the phase of a PACE experiment without RF saturation yields $T_1$, the phase of a PACE experiment with RF saturation yields $T_{1sat}$, while the amplitudes of both experiments yield the MTR (Fig. 1.6 c). From these quantities, the forward transfer rate $k_f = \text{MTR}/T_{1sat}$ can be calculated (Fig. 1.11) [42].
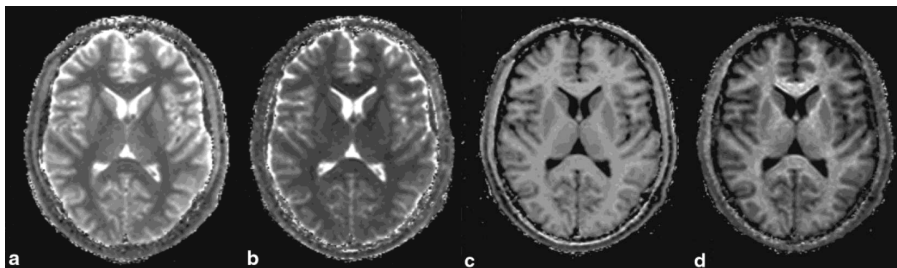


Figure 1.11: Images obtained from a PACE experiment with and without RF saturation at 1.5 T. (a) $T_1$ map, (b) $T_{1sat}$ map, (c) MTR map, (d) magnetization exchange ($k_f$) map [42].

In 2003, Ropele et al. described a new method for mapping the bound pool fraction (BPF $= M_{0,b}/M_{0,a} + M_{0,b}$) [67]. A stimulated echo preparation modulates the phase distribution within a spin ensemble. The labeled spins of the liquid pool then serve as a indicator for magnetization transfer. Advantages of this technique are that no additional relaxation time measurements and no information about the lineshape of the bound pool are needed.

Helms et al. derived an empirical signal equation for a spoiled gradient echo sequence with pulsed saturation [43]. This equation is based on a biexponential time course including $T_1$ relaxation and magnetization transfer. The so-called MT saturation can be obtained from the MT-weighted signal and two reference SPGR signals at different flip angles (Fig. 1.6 d). While the MTR refers to the reduction of the steady-state signal, the MT saturation refers to the saturation effect of a single MT pulse. This concept benefits from the fact that it is insensitive to inhomogeneities of the transmitted RF field and receive coil.

## 1.5 Fast Imaging with Steady-State Free Precession

### 1.5.1 Steady-State Free Precession

Conventional spin echo or gradient echo sequences have long scan times caused by the time it takes to let the magnetization relax back or close to thermal equilibrium before the next RF excitation pulse is played out. Approaches to reduce scan time are to acquire several echoes per excitation as with turbo spin echo (TSE) sequences, or to cover more sampling points in **k**-space after a single excitation as with echo planar imaging (EPI). Another approach to shorten acquisition times is to use repetition times (TR) much smaller than $T_1$ (TR $\ll T_1$), but considerably larger than $T_2$ (TR $\gg T_2$). This means that the longitudinal magnetization cannot return to thermal equilibrium before each new excitation. If TR is even chosen to be less than $T_2$ (TR $\leq T_2$), the transverse magnetization does not relax back to zero. Under these circumstances, the magnetization before an excitation pulse has both longitudinal and transverse components originating from previous excitations. After a certain number of excitations, a dynamic equilibrium or steady state builds up, which means that the magnetization is periodic with TR. A theoretical treatment of the steady state was already presented by Carr in 1958 [68] and by Freeman and Hill [69] and Hinshaw [70] in the 1970s long before fast sequences for MR imaging were available.

The characteristic parameters of a steady-state free precession (SSFP) sequence are:

- the **repetition time TR** being the time between consecutive RF excitation pulses,

- the **echo time TE** denoting the timepoint at which the transverse magnetization is refocused to form an echo,

- the **flip angle $\alpha$** that quantifies the deflection of the magnetization owing to the RF pulse,

- the **phase $\vartheta_n$** of the RF pulse, which determines the direction of the $B_1$ field in the $xy$-plane ($\vartheta_n = 0$ corresponds to a rotation around the $x$-axis),

- the **dephasing angle $\varphi$** describing the rotation of the magnetization around the $z$-axis.
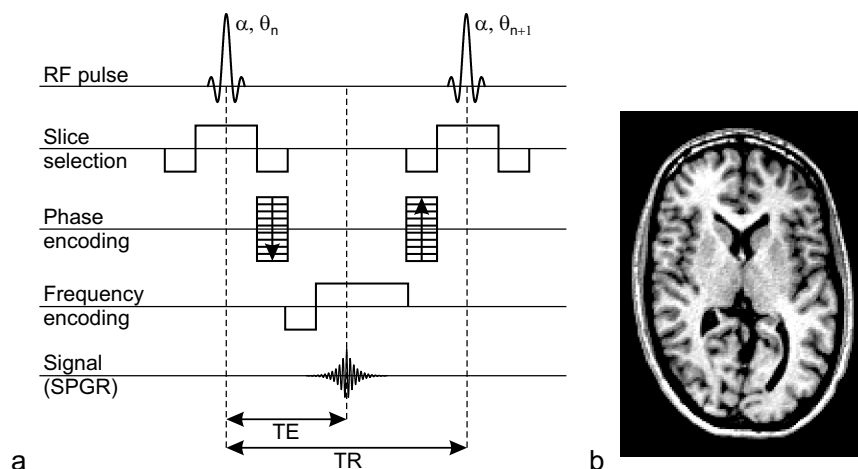
Figure 1.12: (a) Spoiled gradient echo sequence (SPGR), also known as FLASH, or $T_1$-FFE. (b) SPGR acquisition in human brain with TR = 10 ms and $\alpha = 17°$ showing $T_1$-weighted contrast.

In order to reach a steady state, the following conditions must be fulfilled [71–73]: TR and $\alpha$ must be constant, the dephasing $\varphi$ within TR must be constant, and the phase of the RF pulses must satisfy the equation $\vartheta_n = a + bn + cn^2$, where $n = 0, 1, 2, \ldots$, and $a$, $b$, and $c$ are arbitrary constants.

## 1.5.2   Spoiled Gradient Echo

The spoiled gradient echo (SPGR, FLASH, or $T_1$-FFE) sequence (Fig. 1.12) has a characteristic dephasing moment in readout direction. However, from the constraint of constant dephasing within any TR [74], the phase-encoding gradient must be rewound prior to the next excitation. The resulting image exhibits a mixed $T_1$ and $T_2$ contrast [71]. Approximate $T_1$-weighting is only achieved with RF spoiling, which means that the phase of the RF pulse is incremented in a specific way from one pulse to the next:

$$\vartheta_n = \frac{n(n+1)}{2}\,\vartheta_{inc}, \tag{1.8}$$

where $\vartheta_{inc}$ is chosen to be 50° or 117° depending on the manufacturer [71–73]. For these and other possible values of $\vartheta_{inc}$, the RF spoiled gradient echo signal approximates the ideally spoiled signal given by the Ernst equation:

$$S_{\mathrm{SPGR}} = M_0 \sin\alpha \frac{1 - E_1}{1 - E_1 \cos\alpha}, \tag{1.9}$$

where $M_0$ is the equilibrium magnetization and $E_1 := \exp(-\mathrm{TR}/T_1)$ [75]. The flip angle that maximizes the SPGR signal is called the Ernst angle and is given by $\alpha_E := \cos^{-1}(E_1)$.

For low flip angles, the SPGR signal is essentially proton density ($\rho_0$) weighted and independent of $T_1$ and $T_2$. Flip angles above the Ernst angle lead to $T_1$-weighted images, where tissues with long $T_1$ appear dark (Fig. 1.12 b).
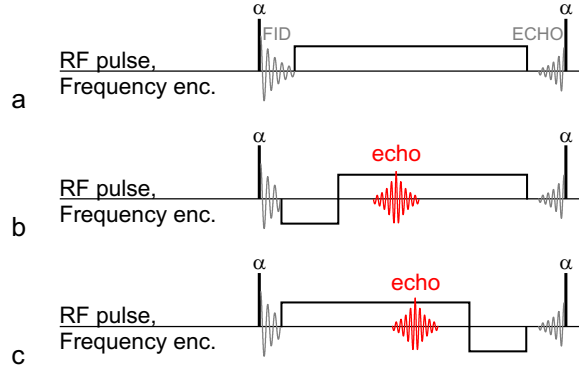
Figure 1.13: (a) A repetitive unit of an SSFP sequence with FID and ECHO. The readout gradient can be shaped to generate an echo from the FID (b) or from the ECHO (c).

### 1.5.3  Steady-state Free Precession FID and ECHO

For non-RF spoiled SSFP, the transverse magnetization contributes to the signal evolution. Therefore, a higher signal is achieved, but often at the cost of reduced contrast.

The transverse magnetization present before an RF pulse is called the ECHO and consists of a number of echoes caused by preceding pulses (Fig. 1.13 a). The signal induced by transverse magnetization after the RF pulse coming from fresh longitudinal magnetization is called the free induction decay (fid). However, the total transverse magnetization after the pulse also consists of the transverse component from before the pulse in addition to the fid and is termed FID (Fig. 1.13 a). Both the FID and the ECHO can be turned into a gradient echo by dephasing and rephasing readout gradients as demonstrated in Fig. 1.13 b and c.

Sequence diagrams of SSFP-FID (FISP, GRASS, FFE, or FAST) and SSFP-ECHO (PSIF, SSFP, $T_2$-FFE, or CE-FAST) are shown in Fig. 1.14 a and b. For nonbalanced SSFP, a dephasing of $\varphi = [-\pi \ldots \pi]$ per imaging voxel is induced from unbalanced gradient moments. Therefore, the steady-state signals of SSFP-FID and SSFP-ECHO are found by averaging the steady-state transverse magnetization within one voxel across all possible dephasing angles [76]:

$$S_{\text{FID}} = M_0 \sin \alpha \, \frac{1 - E_1}{C} \left( \frac{C + DE_2}{\sqrt{D^2 - C^2}} - E_2 \right), \tag{1.10}$$

$$S_{\text{ECHO}} = M_0 \sin \alpha \, \frac{E_2(1 - E_1)}{C} \left( 1 - \frac{D + CE_2}{\sqrt{D^2 - C^2}} \right), \tag{1.11}$$

where $C = E_2(E_1 - 1)(1 + \cos \alpha)$, $D = 1 - E_1 \cos \alpha - (E_1 - \cos \alpha)E_2^2$ and $E_2 = \exp(-\text{TR}/T_2)$. For $\text{TR} \gg T_2$, the SSFP-FID signal converges towards the SPGR signal, whereas the SSFP-ECHO vanishes. For small flip angles, the SSFP-FID signal becomes $\rho_0$-weighted as the SPGR signal. Despite these similarities in the two limiting cases, SSFP-FID and SPGR display substantially different contrast behavior. For both, SSFP-FID and SSFP-ECHO, the signal intensity is very similar for white and gray matter while fluids appears bright
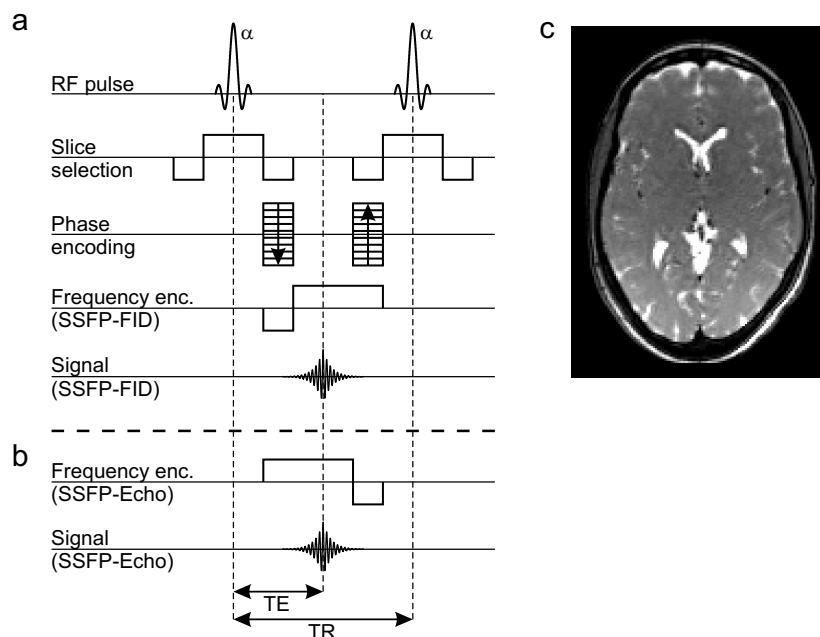
Figure 1.14: (a) SSFP-FID sequence, also known as FISP, GRASS, FFE, or FAST. (b) SSFP-ECHO sequence, also known as PSIF, SSFP, $T_2$-FFE, or CE-FAST. (c) SSFP-FID acquisition on human brain with TR = 3.9 ms and $\alpha = 35°$.

(Fig. 1.14 c). Since the signal is composed of many components formed by earlier excitation pulses, these sequences are very sensitive to flow and motion, which can cause inconsistent dephasing among the TR intervals and spoil the transverse steady state. Since the magnetization directly before the RF pulse is proportional to $E_2$, the scans based on the acquisition of the ECHO are more $T_2$ weighted than those of the FID: $S_{\text{ECHO}}/S_{\text{FID}} \approx E_2^2$.

### 1.5.4 Balanced Steady-State Free Precession

In the previously presented SSFP sequences, the transverse magnetization was dephased between successive RF pulses in order to read out the echo. In balanced SSFP (bSSFP, TrueFISP, FIESTA, or B-FFE), it is fully rephased by a reversed gradient pulse as shown in Fig. 1.15 a, providing the highest signal of all steady-state sequences. Furthermore, this sequence is flow compensated, which means that spins with constant velocity in slice- and readout-direction are not subdued to any dephasing during TR. Since bSSFP has very high requirements on $B_0$-field homogeneity and gradient performance, it has only been clinically used in the past 10 years. To avoid off-resonance effects, it is favorable to use short TR and apply a shim in order to homogenize the main magnetic field.

Typically, a centered echo (TE = TR/2) and an RF phase increment of 180° are used to yield the steady-state signal [69, 76]

$$S_{\text{bSSFP}} = M_0 \sin\alpha \; \sqrt{E_2} \, \frac{1 - E_1}{1 - E_1 E_2 - (E_1 - E_2)\cos\alpha}. \tag{1.12}$$
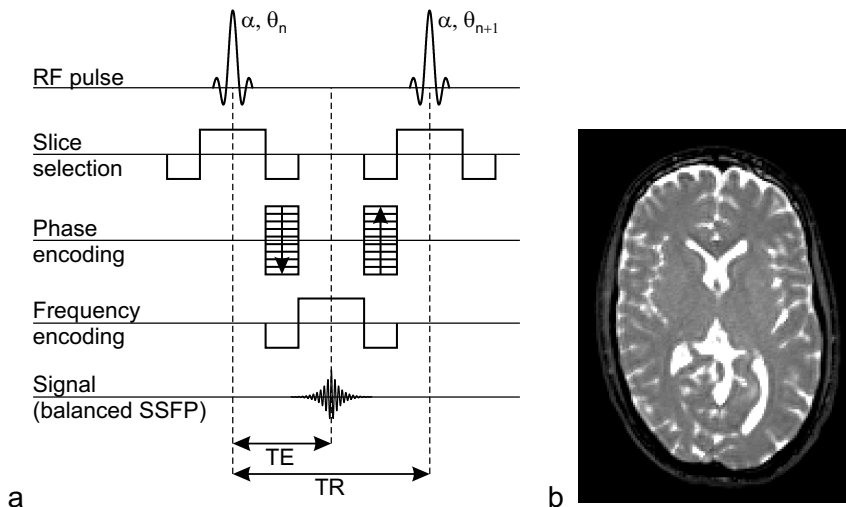
Figure 1.15: (a) Balanced SSFP (bSSFP) sequence, also known as TrueFISP, FIESTA, or B-FFE. (b) BSSFP acquisition on human brain with TR = 4.6 ms and $\alpha = 35°$.

For TR $\ll T_1, T_2$ the signal can be shown to be proportional to $T_2/T_1$ [77]. Therefore, fluids and fat appear hyperintense while white and gray matter exhibit a similar signal intensity owing to their comparable $T_2/T_1$ ratios (Fig. 1.15 b). The flip angle that gives maximum signal is $\alpha_{\mathrm{opt}} \approx \cos^{-1}\left[(T_1/T_2 - 1)/(T_1/T_2 + 1)\right]$ and the corresponding peak signal reads $S_{\mathrm{bSSFP,opt}} \approx 1/2 M_0 \sqrt{T_2/T_1}$.

## 1.6 Magnetization Transfer Effects in Steady-State Free Precession

The signal of bSSFP as given by the Freeman-Hill formula (Eq. (1.12)) is a function of relaxation times, excitation angle, and spin density only [69]. However, considerable signal deviations with varying TR were observed in tissue by Bieri and Scheffler [78]. Magnetization transfer was perceived as major contributor to this signal variation with TR. In tissues, such as brain white matter, where a high MT effect is expected, the signal attenuation for short TR is strongest. Simulations of the bSSFP signal using a two-pool model [28] were in accordance with the measured signal deviations. Also, two bSSFP images with different TR showed a very similar contrast to SPGR images with and without MT prepulse. It could be shown that on-resonant excitation in bSSFP leads to a saturation of restricted pool protons, which becomes negligible for long TR. Moreover, Bieri and Scheffler showed that MT contrast in bSSFP can also be achieved by RF pulse modifications [79]. An elongation of the RF pulse duration $T_{\mathrm{RF}}$ by a factor of $\beta$ results in a reduction of the mean saturation rate per RF pulse by $1/\beta^2$. Combined with a TR elongation these RF pulse modifications were analyzed to yield optimized bSSFP-MT contrast (Fig. 1.16 a and b). Resulting MTR maps were compared to MTR maps using SPGR experiments (Fig. 1.16 c).
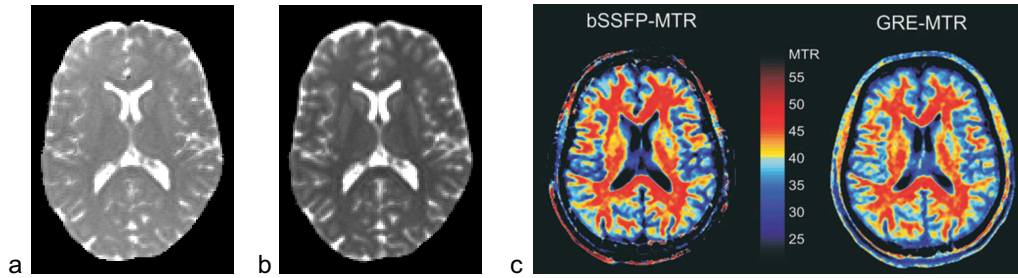
Figure 1.16: Balanced SSFP acquisitions with (a) $T_{RF}$ = 2100 µs and TR = 4.8 ms and (b) $T_{RF}$ = 330 µs and TR = 3.0 ms. A considerable signal attenuation for a short RF pulse and a short TR is observed. (c) Comparison of MTR maps from bSSFP (left) and SPGR (right) of a healthy volunteer.

The concept of magnetization transfer ratio (MTR) imaging using bSSFP has been adapted to nonbalanced SSFP (nb-SSFP) sequences, as well [80]. Compared to bSSFP, these sequences are not sensitive to off-resonance related dephasing. Consequently, SSFP-FID and SSFP-ECHO might be favored for targets with high susceptibility variations (e.g. the musculoskeletal system) and for high field applications. While the MT-free bSSFP signal is insensitive to TR, the signal from SSFP-FID increases slightly with TR and the signal from SSFP-ECHO decreases due to $T_2$-weighting. Therefore, an optimized MT protocol for nb-SSFP minimizes signal variations from changes in TR. Histogram analysis in human brain revealed lower MTR values for nb-SSFP as compared to bSSFP, but excellent agreement in terms of tissue classification. Furthermore, images of human patellar cartilage were presented at 3 T and at 7 T using SSFP-FID (Fig. 1.17).
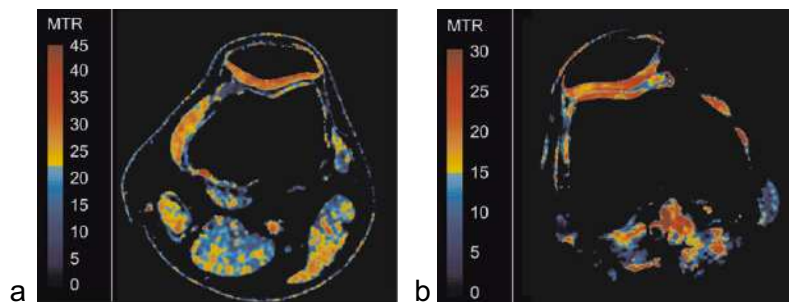


Figure 1.17: Nonbalanced SSFP-based MTR images of human patellar cartilage (a) at 3 T with a voxel size of $500 \times 500 \times 1000$ µm and (b) at 7 T with a voxel size of $280 \times 280 \times 3000$ µm.

## 1.7   Aim of this Thesis

Magnetization transfer has become an accepted tool to generate a new quality of contrast in MRI. This contrast is based on tissue microstructure and is able

to visualize nonwater components. Additional information about tissue changes are desirable for better understanding, for early diagnosis and for monitoring treatment response of many pathologies. However, most MT imaging techniques are still not suitable for application in the daily clinical routine. A major issue is that sampling of MT dispersion curves by MT-weighted spin echo or gradient echo sequences makes acquisition times too long or allows only for imaging of a few slices. In contrast, SSFP sequences offer short acquisition times and high signal-to-noise ratios (SNR) in combination with their intrinsic MT-sensitivity [78].

The inherent MT contrast in SSFP has so far been used to generate MTR maps [80]. In this thesis, new MT imaging methods are developed using SSFP sequences. A theoretical framework has been presented for balanced SSFP in the master's thesis preceding this work [81]. To ideally map MT in different types of tissue, the concept is adapted to nb-SSFP. The fast quantitative MT imaging methods are tested and discussed widely to overcome the issue of limited applicability.

Another issue that has to be addressed before clinical implementation is the reproducibility of a new MT imaging technique. This is realized here in terms of a variability analysis of bSSFP-based MTR imaging.

After presenting the novel methods, their feasibility is demonstrated on healthy volunteers. Comparisons to conventional methods are made and finally, applications in the clinical environment are illustrated.

## 1.8   Outline of the Thesis

In the first part of **Chapter 2**, a new quantitative MT imaging technique is developed based on bSSFP. Differential equations for the on-resonant bSSFP signal including MT exchange terms are partially integrated. Using the assumption that relaxation and exchange processes can be separated within TR, the extended steady-state eigenvalue equation is solved analytically. Numerical simulations of the Bloch equations are performed to confirm the validity of the assumptions made. In the second part of this chapter, the new MT-bSSFP equation is used to determine quantitative MT parameters in human brain after a separate measurement of $T_1$ and $B_1$. The bound pool fraction $F$ and the forward exchange rate $k_f$ as well as the relaxation times are compared to literature values. It is shown that off-resonance related signal deviations are typically small in brain tissue. Because of the short acquisition times combined with high SNR and good reproducibility, bSSFP might offer high potential for clinically feasible qMT imaging.

With the presented method, qMT parameters are derived by measuring the signal dependence on the flip angle and on the RF pulse duration. In **Chapter 3** a shortened protocol is introduced without flip angle variation and applied in human brain. This protocol benefits from a reduced acquisition time as well as from the possibility to incorporate phase-cycled acquisitions to reduce banding artifacts. It has recently been shown that the effect of finite RF pulses can lead to substantial bSSFP signal deviations [82]. In the second part of this chapter, this

effect is accounted for by a modification to the two-pool bSSFP signal equation. The extent of change in qMT parameters is assessed in brain white and gray matter.

While bSSFP techniques are well applicable in targets with low susceptibility variations, such as the human brain, targets of the musculoskeletal system, such as cartilage and muscle cause signal loss from off-resonance effects. As a result, in **Chapter 4**, the proposed qMT imaging principle is adapted to nb-SSFP. First, a two-pool SSFP-FID signal equation is derived based on coupled Bloch equations. Numerical simulations are done to confirm the separation of relaxation and exchange processes. Secondly, qMT parameters are derived from human femoral muscle and human patellar cartilage. Finally, consistency with literature and issues arising from the flow and motion sensitivity of SSFP-FID are discussed.

In addition to qMT imaging, bSSFP-based MTR measurements are performed in significantly shorter times and with an improved SNR compared to conventional methods. In **Chapter 5**, the reproducibility of bSSFP MTR is analyzed. First, optimal flip angles were chosen from the theoretically predicted signal dependence. Then measurements at different systems and several sites were carried out. The low variability achieved in brain tissue of healthy subjects is important for future MTR scans in a clinical setting.

In order to establish bSSFP-based qMT imaging in a clinical setting, a reference data set of normal appearing brain structures is analyzed in **Chapter 6**. It is possible to assess regional variations in relaxation times and MT parameters. First experiences of bSSFP-based qMT imaging in tumor and ischemia patients are presented. Quantitative parameters are analyzed in various tumor regions and, on the other hand, in a time series after cerebral stroke.

# References

[1] I. Solomon. Relaxation Processes in a System of Two Spins. *Phys Rev*, 99: 559–565, 1955.

[2] I. Solomon and N. Bloembergen. Nuclear Magnetic Interactions in the HF Molecule. *J Chem Phys*, 25:261–266, 1956.

[3] S. Forsen and R. A. Hoffman. Study of Moderately Rapid Chemical Exchange Reactions by Means of Nuclear Magnetic Double Resonance. *J Chem Phys*, 39(11):2892–2901, 1963.

[4] R. A. Hoffman and S. Forsen. Transient and Steady-State Overhauser Experiments in the Investigation of Relaxation Processes. Analogies between Chemical Exchange and Relaxation. *J Chem Phys*, 45:2049–2060, 1966.

[5] H. T. Edzes and E. T. Samulski. The Measurement of Cross-Relaxation Effects in the Proton Nmr Spin-Lattice Relaxation of Water in Biological Systems: Hydrated Collagen and Muscle. *J Magn Reson*, 31:207–229, 1978.

[6] S. D. Wolff and R. S. Balaban. Magnetization Transfer Contrast (MTC) and Tissue Water Proton Relaxation in Vivo. *Magn Reson Med*, 10(1):135–44, 1989.

[7] R. M. Henkelman, G. J. Stanisz, and S. J. Graham. Magnetization Transfer in MRI: A Review. *NMR Biomed*, 14(2):57–64, 2001.

[8] G. B. Pike, B. S. Hu, G. H. Glover, and D. R. Enzmann. Magnetization Transfer Time-of-Flight Magnetic Resonance Angiography. *Magn Reson Med*, 25(2):372–9, 1992.

[9] V. Dousset, R. I. Grossman, K. N. Ramer, M. D. Schnall, L. H. Young, F. Gonzalez-Scarano, E. Lavi, and J. A. Cohen. Experimental Allergic Encephalomyelitis and Multiple Sclerosis: Lesion Characterization with Magnetization Transfer Imaging. *Radiology*, 182(2):483–91, 1992.

[10] J. Eng, T. L. Ceckler, and R. S. Balaban. Quantitative 1H Magnetization Transfer Imaging in Vivo. *Magn Reson Med*, 17(2):304–14, 1991.

[11] E. Liepinsh and G. Otting. Proton Exchange Rates from Amino Acid Side Chains–Implications for Image Contrast. *Magn Reson Med*, 35(1):30–42, 1996.

[12] T. Ceckler, J. Maneval, and B. Melkowits. Modeling Magnetization Transfer Using a Three-Pool Model and Physically Meaningful Constraints on the Fitting Parameters. *J Magn Reson*, 151(1):9–27, 2001.

[13] T. A. Fralix, T. L. Ceckler, S. D. Wolff, S. A. Simon, and R. S. Balaban. Lipid Bilayer and Water Proton Magnetization Transfer: Effect of Cholesterol. *Magn Reson Med*, 18(1):214–23, 1991.

[14] R. C. Mehta, G. B. Pike, and D. R. Enzmann. Magnetization Transfer MR of the Normal Adult Brain. *AJNR Am J Neuroradiol*, 16(10):2085–91, 1995.

[15] S. H. Koenig. Cholesterol of Myelin Is the Determinant of Gray-White Contrast in MRI of Brain. *Magn Reson Med*, 20(2):285–91, 1991.

[16] Steven D. Wolff and Robert S. Balaban. NMR Imaging of Labile Proton Exchange. *Journal of Magnetic Resonance (1969)*, 86(1):164–169, 1990.

[17] V. Guivel-Scharen, T. Sinnwell, S. D. Wolff, and R. S. Balaban. Detection of Proton Chemical Exchange between Metabolites and Water in Biological Tissues. *J Magn Reson*, 133(1):36–45, 1998.

[18] K. M. Ward, A. H. Aletras, and R. S. Balaban. A New Class of Contrast Agents for MRI Based on Proton Chemical Exchange Dependent Saturation Transfer (CEST). *J Magn Reson*, 143(1):79–87, 2000.

[19] Jinyuan Zhou and Peter C.M. van Zijl. Chemical Exchange Saturation Transfer Imaging and Spectroscopy. *Progress in Nuclear Magnetic Resonance Spectroscopy*, 48(2-3):109–136, 2006.

[20] R. G. Bryant. The Dynamics of Water-Protein Interactions. *Annu Rev Biophys Biomol Struct*, 25:29–53, 1996.

[21] R. S. Balaban and T. L. Ceckler. Magnetization Transfer Contrast in Magnetic Resonance Imaging. *Magn Reson Q*, 8(2):116–37, 1992.

[22] S. Zhang, P. Winter, K. Wu, and A. D. Sherry. A Novel Europium(Iii)-Based MRI Contrast Agent. *J Am Chem Soc*, 123(7):1517–8, 2001.

[23] S. Aime, A. Barge, D. Delli Castelli, F. Fedeli, A. Mortillaro, F. U. Nielsen, and E. Terreno. Paramagnetic Lanthanide(III) Complexes as pH-Sensitive Chemical Exchange Saturation Transfer (CEST) Contrast Agents for MRI Applications. *Magn Reson Med*, 47(4):639–48, 2002.

[24] J. Zhou, J. F. Payen, D. A. Wilson, R. J. Traystman, and P. C. van Zijl. Using the Amide Proton Signals of Intracellular Proteins and Peptides to Detect pH Effects in MRI. *Nat Med*, 9(8):1085–90, 2003.

[25] J. Zhou, B. Lal, D. A. Wilson, J. Laterra, and P. C. van Zijl. Amide Proton Transfer (APT) Contrast for Imaging of Brain Tumors. *Magn Reson Med*, 50(6):1120–6, 2003.

[26] N. Goffeney, J. W. Bulte, J. Duyn, Jr. Bryant, L. H., and P. C. van Zijl. Sensitive NMR Detection of Cationic-Polymer-Based Gene Delivery Systems Using Saturation Transfer Via Proton Exchange. *J Am Chem Soc*, 123(35): 8628–9, 2001.

[27] K. Snoussi, J. W. Bulte, M. Gueron, and P. C. van Zijl. Sensitive CEST Agents Based on Nucleic Acid Imino Proton Exchange: Detection of Poly(Ru) and of a Dendrimer-Poly(Ru) Model for Nucleic Acid Delivery and Pharmacology. *Magn Reson Med*, 49(6):998–1005, 2003.

[28] R. M. Henkelman, X. Huang, Q. S. Xiang, G. J. Stanisz, S. D. Swanson, and M. J. Bronskill. Quantitative Interpretation of Magnetization Transfer. *Magn Reson Med*, 29(6):759–66, 1993.

[29] H. M. McConnell. Reaction Rates by Nuclear Magnetic Resonance. *J Chem Phys*, 28(3):430–431, 1958.

[30] X. Wu. Lineshape of Magnetization Transfer Via Cross Relaxation. *J Magn Reson*, 94:186–190, 1991.

[31] C. Morrison and R. M. Henkelman. A Model for Magnetization Transfer in Tissues. *Magn Reson Med*, 33(4):475–82, 1995.

[32] J. G. Li, S. J. Graham, and R. M. Henkelman. A Flexible Magnetization Transfer Line Shape Derived from Tissue Experimental Data. *Magn Reson Med*, 37(6):866–71, 1997.

[33] R. W. Holt, J. L. Duerk, J. Hua, and G. C. Hurst. Estimation of Bloch Model MT Spin System Parameters from Z-Spectral Data. *Magn Reson Med*, 31(2):122–30, 1994.

[34] G. B. Pike. Pulsed Magnetization Transfer Contrast in Gradient Echo Imaging: A Two-Pool Analytic Description of Signal Response. *Magn Reson Med*, 36(1):95–103, 1996.

[35] S. J. Graham and R. M. Henkelman. Understanding Pulsed Magnetization Transfer. *J Magn Reson Imaging*, 7(5):903–12, 1997.

[36] J. G. Sled and G. B. Pike. Quantitative Interpretation of Magnetization Transfer in Spoiled Gradient Echo MRI Sequences. *J Magn Reson*, 145(1): 24–36, 2000.

[37] J. Hua and G. C. Hurst. Analysis of On- and Off-Resonance Magnetization Transfer Techniques. *J Magn Reson Imaging*, 5(1):113–20, 1995.

[38] A. Ramani, C. Dalton, D. H. Miller, P. S. Tofts, and G. J. Barker. Precise Estimate of Fundamental in-Vivo MT Parameters in Human Brain in Clinically Feasible Times. *Magn Reson Imaging*, 20(10):721–31, 2002.

[39] B. S. Hu, S. M. Conolly, G. A. Wright, D. G. Nishimura, and A. Macovski. Pulsed Saturation Transfer Contrast. *Magn Reson Med*, 26(2):231–40, 1992.

[40] E. Schneider, R. W. Prost, and G. H. Glover. Pulsed Magnetization Transfer Versus Continuous Wave Irradiation for Tissue Contrast Enhancement. *J Magn Reson Imaging*, 3(2):417–23, 1993.

[41] I. Berry, G. J. Barker, F. Barkhof, A. Campi, V. Dousset, J. M. Franconi, A. Gass, W. Schreiber, D. H. Miller, and P. S. Tofts. A Multicenter Measurement of Magnetization Transfer Ratio in Normal White Matter. *J Magn Reson Imaging*, 9(3):441–6, 1999.

[42] S. Ropele, R. Stollberger, H. P. Hartung, and F. Fazekas. Estimation of Magnetization Transfer Rates from PACE Experiments with Pulsed RF Saturation. *J Magn Reson Imaging*, 12(5):749–56, 2000.

[43] G. Helms, H. Dathe, and P. Dechent. Quantitative FLASH MRI at 3T Using a Rational Approximation of the Ernst Equation. *Magn Reson Med*, 59(3): 667–72, 2008.

[44] D. A. Finelli, G. C. Hurst, Jr. Amantia, P., R. P. Gullapali, and A. Apicella. Cerebral White Matter: Technical Development and Clinical Applications of Effective Magnetization Transfer (MT) Power Concepts for High-Power, Thin-Section, Quantitative MT Examinations. *Radiology*, 199(1):219–26, 1996.

[45] G. J. Barker, P. S. Tofts, and A. Gass. An Interleaved Sequence for Accurate and Reproducible Clinical Measurement of Magnetization Transfer Ratio. *Magn Reson Imaging*, 14(4):403–11, 1996.

[46] R. R. Lee and A. P. Dagher. Low Power Method for Estimating the Magnetization Transfer Bound-Pool Macromolecular Fraction. *J Magn Reson Imaging*, 7(5):913–7, 1997.

[47] S. Ropele, R. Stollberger, F. Ebner, and F. Fazekas. T1 Imaging Using Phase Acquisition of Composite Echoes. *Magn Reson Med*, 41(2):386–91, 1999.

[48] S. Ropele and F. Fazekas. Magnetization Transfer MR Imaging in Multiple Sclerosis. *Neuroimaging Clin N Am*, 19(1):27–36, 2009.

[49] T. J. Kurki, P. T. Niemi, and N. Lundbom. Gadolinium-Enhanced Magnetization Transfer Contrast Imaging of Intracranial Tumors. *J Magn Reson Imaging*, 2(4):401–6, 1992.

[50] M. H. Pui. Magnetization Transfer Analysis of Brain Tumor, Infection, and Infarction. *J Magn Reson Imaging*, 12(3):395–9, 2000.

[51] J. M. Prager, J. D. Rosenblum, D. C. Huddle, C. K. Diamond, and C. E. Metz. The Magnetization Transfer Effect in Cerebral Infarction. *AJNR Am J Neuroradiol*, 15(8):1497–500, 1994.

[52] T. Tourdias, V. Dousset, I. Sibon, E. Pele, P. Menegon, J. Asselineau, C. Pachai, F. Rouanet, P. Robinson, G. Chene, and J. M. Orgogozo. Magnetization Transfer Imaging Shows Tissue Abnormalities in the Reversible Penumbra. *Stroke*, 38(12):3165–71, 2007.

[53] B. Quesson, A. K. Bouzier, E. Thiaudiere, C. Delalande, M. Merle, and P. Canioni. Magnetization Transfer Fast Imaging of Implanted Glioma in the Rat Brain at 4.7 T: Interpretation Using a Binary Spin-Bath Model. *J Magn Reson Imaging*, 7(6):1076–83, 1997.

[54] J. G. Sled and G. B. Pike. Quantitative Imaging of Magnetization Transfer Exchange and Relaxation Properties in Vivo Using MRI. *Magn Reson Med*, 46(5):923–31, 2001.

[55] Y. T. Zhang, H. N. Yeung, P. L. Carson, and J. H. Ellis. Experimental Analysis of T1 Imaging with a Single-Scan, Multiple-Point, Inversion-Recovery Technique. *Magn Reson Med*, 25(2):337–43, 1992.

[56] C. S. Poon and R. M. Henkelman. Practical T2 Quantitation for Clinical Applications. *J Magn Reson Imaging*, 2(5):541–53, 1992.

[57] V. L. Yarnykh. Pulsed Z-Spectroscopic Imaging of Cross-Relaxation Parameters in Tissues for Human MRI: Theory and Clinical Applications. *Magn Reson Med*, 47(5):929–39, 2002.

[58] E. K. Fram, R. J. Herfkens, G. A. Johnson, G. H. Glover, J. P. Karis, A. Shimakawa, T. G. Perkins, and N. J. Pelc. Rapid Calculation of T1 Using Variable Flip Angle Gradient Refocused Imaging. *Magn Reson Imaging*, 5 (3):201–8, 1987.

[59] V. L. Yarnykh and C. Yuan. Cross-Relaxation Imaging Reveals Detailed Anatomy of White Matter Fiber Tracts in the Human Brain. *Neuroimage*, 23(1):409–24, 2004.

[60] M. Cercignani, M. R. Symms, K. Schmierer, P. A. Boulby, D. J. Tozer, M. Ron, P. S. Tofts, and G. J. Barker. Three-Dimensional Quantitative Magnetisation Transfer Imaging of the Human Brain. *Neuroimage*, 27(2): 436–41, 2005.

[61] D. F. Gochberg, R. P. Kennan, M. D. Robson, and J. C. Gore. Quantitative Imaging of Magnetization Transfer Using Multiple Selective Pulses. *Magn Reson Med*, 41(5):1065–72, 1999.

[62] D. F. Gochberg and J. C. Gore. Quantitative Imaging of Magnetization Transfer Using an Inversion Recovery Sequence. *Magn Reson Med*, 49(3): 501–5, 2003.

[63] D. F. Gochberg and J. C. Gore. Quantitative Magnetization Transfer Imaging Via Selective Inversion Recovery with Short Repetition Times. *Magn Reson Med*, 57(2):437–41, 2007.

[64] E. A. Louie, D. F. Gochberg, M. D. Does, and B. M. Damon. Transverse Relaxation and Magnetization Transfer in Skeletal Muscle: Effect of pH. *Magn Reson Med*, 61(3):560–9, 2009.

[65] R. D. Dortch, K. Li, A. A. Tamhane, E. B. Welch, D. F. Gochberg, J. C. Gore, and S. A. Smith. Quantitative Magnetization Transfer Imaging of Human Brain at 3T Using Selective Inversion Recovery. *In: Proceedings of the 18th Annual Meeting of ISMRM, Stockholm, Sweden, 2010*, page 335, 2010.

[66] S. Ropele, R. Stollberger, P. Kapeller, H. P. Hartung, and F. Fazekas. Fast Multislice T(1) and T(1sat) Imaging Using a Phase Acquisition of Composite Echoes (PACE) Technique. *Magn Reson Med*, 42(6):1089–97, 1999.

[67] S. Ropele, T. Seifert, C. Enzinger, and F. Fazekas. Method for Quantitative Imaging of the Macromolecular 1H Fraction in Tissues. *Magn Reson Med*, 49(5):864–71, 2003.

[68] H.Y. Carr. Steady-State Free Precession in Nuclear Magnetic Resonance. *Phys Rev*, 112(5):1693–1701, 1958.

[69] R Freeman and HDW Hill. Phase and Intensity Anomalies in Fourier Transform NMR. *J Magn Reson*, 4:366–383, 1971.

[70] W. S. Hinshaw. Image Formation by Nuclear Magnetic Resonance: The Sensitive-Point Method. *J Appl Phys*, 47:3709–3721, 1976.

[71] Y. Zur, M. L. Wood, and L. J. Neuringer. Spoiling of Transverse Magnetization in Steady-State Sequences. *Magn Reson Med*, 21(2):251–63, 1991.

[72] W. T. Sobol and D. M. Gauntt. On the Stationary States in Gradient Echo Imaging. *J Magn Reson Imaging*, 6(2):384–98, 1996.

[73] K. Scheffler. A Pictorial Description of Steady-States in Rapid Magnetic Resonance Imaging. *Concepts in Magnetic Resonance*, 11(5):291–304, 1999.

[74] M. L. Gyngell, N. D. Palmer, and L. M. Eastwood. The Application of Steady-State Free Precession in 2D-FT MR Imaging. *In: Proceedings of the 5th Annual SMRM meeting, Montreal, Canada*, 1986.

[75] R. R. Ernst, G. Bodenhausen, and A. Wokaun. Priciples of Nuclear Magnetic Resonance in One and Two Dimensions. *Clarendon Press, Oxford*, 1987.

[76] Y. Zur, S. Stokar, and P. Bendel. An Analysis of Fast Imaging Sequences with Steady-State Transverse Magnetization Refocusing. *Magn Reson Med*, 6(2):175–93, 1988.

[77] EM Haacke, RW Brown, MR Thompson, and R. Venkatesan. *Magnetic Resonance Imaging: Physical Principles and Sequence Design*. Wiley, 1999.

[78] O. Bieri and K. Scheffler. On the Origin of Apparent Low Tissue Signals in Balanced SSFP. *Magn Reson Med*, 56(5):1067–74, 2006.

[79] O. Bieri and K. Scheffler. Optimized Balanced Steady-State Free Precession Magnetization Transfer Imaging. *Magn Reson Med*, 58(3):511–8, 2007.

[80] O. Bieri, T. C. Mamisch, S. Trattnig, and K. Scheffler. Steady State Free Precession Magnetization Transfer Imaging. *Magn Reson Med*, 60(5):1261–6, 2008.

[81] M. Gloor. Quantitative Magnetization Transfer Imaging of the Brain Based on Balanced Steady-State Free Precession. Master's thesis, University of Basel, 2007.

[82] O. Bieri and K. Scheffler. SSFP Signal with Finite RF Pulses. *Magn Reson Med*, 62(5):1232–41, 2009.

# Chapter 2

# Quantitative Magnetization Transfer Imaging Using Balanced SSFP

## 2.1   Introduction

Balanced steady-state free precession (bSSFP; also known as TrueFISP, FIESTA, and balanced FFE) [1, 2] has become a valuable and indispensable tool in diagnostic imaging over the last several years, especially for cardiac and cardiovascular applications [3–5]. It is generally accepted that signal formation in bSSFP can be derived from the Freeman-Hill formula [6], being proportional to the $\sqrt{T_2/T_1}$ for repetition times $\mathrm{TR} \ll T_1, T_2$ [7]. However, only recently subtle signal deviations [8–10] from the Freeman-Hill formula indicated further contrast mechanisms, especially the steady-state of bSSFP in tissues may be reduced up to a factor of two from magnetization transfer (MT) effects [11]. Here, short TRs in combination with large flip angles ($\alpha$) saturate the magnetization of protons associated with macromolecules and membranes in biological tissues (restricted pool protons). As a result, subsequent exchange of these protons with mobile ones (liquid pool protons) constituting the steady-state leads to an overall signal reduction, if compared to a situation in absence of exchange. For bSSFP, on-resonant excitation thus not only generates the steady-state but also acts directly as MT sensitizing radio-frequency (RF) pulse. From this, a new method for MT imaging with bSSFP was proposed [12], which in contrast to common MT methods [13–15] circumvents the need for additional MT sensitizing pre-pulses.

MT was first demonstrated by Wolff and Balaban in the late 1980s [16]. Not only has it become a standard tool for suppression of background signals from tissues in MR angiography [14], but it was also realized that MT shows great promise in the field of multiple sclerosis offering tissue characterization beyond conventional $T_1$, $T_2$ and $T_2^*$ [16]. In its simplest and common form of quantification, MT effects are often condensed within the so-called magnetization transfer ratio (MTR) [17]. MTR has become popular not only for characterizing subtle diseases in the brain [15] but also for the assessment of breast, knee and cartilage [14]. Although great effort has been undertaken to ensure reproducibility in MTR measurements [18], the phenomenological breakdown of a complex tissue system to a single parameter may be inappropriate simply by its virtue of oversimplification, and thus may overlook useful diagnostic information. Indeed, there has been given evidence that MTR has only limited pathological specificity [19], making MTR results incomplete and controversial. As a result, binary spin-bath models have been investigated in detail over the last several years by many research groups, capable of gaining intrinsic MT model parameters [19–21]. Quantitative MT imaging (qMTI) yields the fraction ($F$) of restricted pool protons, the magnetization exchange rate ($k_f$), as well as the pool relaxation properties ($T_1$, $T_2$). Recent studies indicate that especially $F$ may be of great diagnostic potential, since it correlates with the myelin content in brain white matter [22]. Quantitative MT, in contrast to MTR, has the potential to yield extended and unquestionable diagnostic information; however, measurement protocols lack clinically applicable acquisition times.

So far, quantitative MT parameters are commonly derived from associated MT dispersion curves. Sampling of these curves is time consuming since different MT-weighted spin-echo or gradient-echo measurements have to be acquired based

on a set of MT pulses that differ in power and off-resonance frequency [19, 20]. In contrast, the overall MT sensitivity of bSSFP in combination with its excellent SNR and the short acquisition time makes it an ideal candidate to meet the clinical requirements for fast and reliable high resolution qMTI. In the first part of this work, an extended bSSFP signal equation is derived based on a binary spin-bath model to take MT exchange effects into account. Assuming that relaxation and exchange can be separated into two independent processes within any TR, partial integration of the coupled Bloch equations yields an extended steady-state eigenvector equation for bSSFP that can be solved analytically. Numerical simulations confirm the validity of the derived two-pool bSSFP signal equation and thereby justify the conceptual separation of exchange and relaxation processes. In the second part of this work, the extended two-pool bSSFP signal equation is used to derive qMTI parameters from human brain, such as the fractional pool size and corresponding exchange rates. It will be demonstrated that the fitted parameter values are in good correspondence with literature values. Possible issues and differences with respect to common qMTI methods are discussed and analyzed. Finally, it will be shown that qMTI with bSSFP offers great potential for generating qualitative high resolution MT parameter maps within clinically feasible acquisition times. In summary, this work introduces a novel fast and quantitative MTI method that is based on bSSFP.

## 2.2   Theory

### 2.2.1   Single-Pool BSSFP Signal Equation

For a centered echo (TE = TR/2) between alternating excitations ($\pm\alpha$), the steady-state of bSSFP is calculated from the Bloch equations using partial integration, yielding

$$M_y = M_0 \sin\alpha \, \sqrt{E_2} \frac{1 - E_1}{1 - E_1 E_2 - (E_1 - E_2)\cos\alpha},\qquad(2.1)$$

where $E_{1,2} = \exp(-\text{TR}/T_{1,2})$ and $M_0$ is the equilibrium magnetization [6, 7]. This formal description has been confirmed for simple probes consisting of a single aqueous phase [11]. However, considerable deviations (up to a factor of two) were detected in tissues, and the molecular origin of this apparent signal reduction was found to be MT [11]. Thus, at least for tissues the ordinary description of the steady-state according to Eq. (2.1) is inappropriate and demands for an extended bSSFP signal equation including MT effects. In the following, signal formation in bSSFP is analyzed based on a standard binary spin-bath MT model [19, 23] similar to the two compartment model for blood oxygen saturation [24].

### 2.2.2   Two-Pool BSSFP MT Model

The minimal model for MT based signal analysis is composed of two pools: a liquid pool of "free" protons (subscript $f$) and a semisolid of protons that are restricted in motion (subscript $r$). The formal description of this binary spin-bath

model leads to a set of coupled differential equations, as described in any detail elsewhere [19, 23]. Saturation of restricted pool protons is typically achieved by off-resonance irradiation (frequency offset $\Delta$) that ideally leaves the magnetization of free pool protons unaffected. The effect of pulsed irradiation [25] on the longitudinal magnetization of the restricted pool protons can be described by a time-dependent mean saturation rate

$$\langle W(\Delta) \rangle = \frac{\pi}{\mathrm{T_{RF}}} \int\limits_0^{\mathrm{T_{RF}}} \omega_1^2(t) dt \, G(\Delta), \tag{2.2}$$

where $G(\Delta)$ is the absorption line shape, and where $\langle W(\Delta) \rangle$ depends on the shape $\omega_1(t) = \gamma \, |\mathbf{B}_1(t)|$ and on the duration $\mathrm{T_{RF}}$ of the RF pulse.

On-resonance RF pulses are applied for MT bSSFP, i.e. $\Delta \to 0$ [11], and the system of differential equations [19] reduces to:

$$\frac{dM_{x,f}}{dt} = -R_{2,f} M_{x,f}, \tag{2.3a}$$

$$\frac{dM_{y,f}}{dt} = -R_{2,f} M_{y,f} + \omega_1(t) M_{z,f}, \tag{2.3b}$$

$$\frac{dM_{z,f}}{dt} = R_{1,f}(M_{0,f} - M_{z,f}) - k_f M_{z,f} + k_r M_{z,r} - \omega_1(t) M_{y,f}, \tag{2.3c}$$

$$\frac{dM_{z,r}}{dt} = R_{1,r}(M_{0,r} - M_{z,r}) + k_f M_{z,f} - k_r M_{z,r} - W(\Delta \to 0, t) M_{z,r}, \tag{2.3d}$$

where the subscripts $x$, $y$, $z$ denote the various spatial components of the magnetization vector $\mathbf{M}$, $R_{1,f}$ ($R_{1,r}$) refers to the longitudinal relaxation rate, and $R_{2,f}$ ($R_{2,r}$) to the transverse relaxation rate of the pools ($R_{1,2} = 1/T_{1,2}$). Magnetization exchange is given by the pseudo-first order rate constants $k_f = R M_{0,r}$ and $k_r = R M_{0,f}$, where $R$ is the fundamental rate constant between the two pools and $M_{0,f}$ ($M_{0,r}$) denotes the equilibrium magnetization of the free (restricted) pool. The fractional size of the restricted pool amounts to $F = M_{0,r}/M_{0,f}$, and by definition $k_r = k_f/F$.

### 2.2.3 Idealized Two-Pool BSSFP Signal Equation

The restricted pool in an idealized MT bSSFP experiment is fully saturated, i.e. $M_{z,r} = 0$. This leads to a decoupling of Eqs. (2.3c) and (2.3d) similar to the idealized MT spoiled GRE case [26]. Eq. (2.3c) can be rewritten as

$$\frac{dM_{z,f}}{dt} = (R_{1,f} + k_f) \left( \frac{R_{1,f}}{R_{1,f} + k_f} M_{0,f} - M_{z,f} \right) - \omega_1(t) M_{y,f} \tag{2.4}$$

being formally analogous to a single-pool situation, but with modified longitudinal relaxation and equilibrium magnetization. Therefore, Eq. (2.1) can be used to describe the idealized two-pool bSSFP signal using the substitutions

$$R_{1,f} \to R_{1,f} + k_f \quad \text{and} \quad M_{0,f} \to \frac{R_{1,f}}{R_{1,f} + k_f} M_{0,f}. \tag{2.5}$$

However, it can be readily deduced that especially in the range of low to moderate flip angles the $M_{z,r} = 0$ condition is inapplicable leading to a substantial overestimation of MT effects at low saturation levels. Thus, although the idealized bSSFP MT model is only of limited experimental interest, it represents the theoretical upper bound in the overall achievable MT effects.

### 2.2.4 Two-Pool BSSFP Signal Equation

Since the idealized two-pool model may fail to yield adequate MT parameter estimations due to practical limitations in the specific absorption rate (SAR) to satisfy $M_{z,r} = 0$, the two-pool model equations (2.3a)-(2.3d) must be solved. Although, in principle this system of coupled differential equations may be solved, the solution is complex and cumbersome. Therefore, a different approach based on partially integrated Bloch equations is presented, which methodologically closely follows the vector model description of bSSFP, as introduced by Carr in 1958 [1] and applied by many others [2, 6, 7] to derive signal properties of bSSFP (see Eq. (2.1)). Beside the normal separation of excitation and relaxation processes, it is further assumed that exchange processes decouple from relaxation processes within the short repetition times commonly used with bSSFP. This approach is valid as long as fractional pool size modifications from longitudinal relaxation processes are negligible within TR, which is quite similar to the concept of instantaneous rotation that allows for the decoupling of excitation and relaxation. Based on these simplifications, an analytical solution to the two-pool bSSFP model can be derived as follows:

Without loss of generality, RF pulses are played out along the $x$-axis. As a result, only $y$-components of the transverse magnetization contribute to the steady-state signal, and the system of differential equations (2.3a)-(2.3d) with magnetization $\mathbf{M} = (M_{x,f}\ M_{y,f}\ M_{z,f}\ M_{z,r})$ can be reduced to $\mathbf{M} = (M_{y,f}\ M_{z,f}\ M_{z,r})$. Exchange and relaxation parts of Eqs. (2.3b)-(2.3d) yield a solution of form $\mathbf{M}(t) = \mathbf{A}(t) \cdot \mathbf{M}(0)$ and $\mathbf{M}(t) = \mathbf{E}(t) \cdot \mathbf{M}(0)$ with matrix representations

$$
\begin{aligned}
\mathbf{A}(t) &= \frac{1}{F+1} \begin{pmatrix} F+1 & 0 & 0 \\ 0 & 1 + Fe^{-(F+1)k_r t} & 1 - e^{-(F+1)k_r t} \\ 0 & F - Fe^{-(F+1)k_r t} & F + e^{-(F+1)k_r t} \end{pmatrix} \text{ and} \\
\mathbf{E}(t) &= \begin{pmatrix} E_{2,f} & 0 & 0 \\ 0 & E_{1,f} & 0 \\ 0 & 0 & E_{1,r} \end{pmatrix},
\end{aligned} \tag{2.6}
$$

where $E_{2,f} = \exp(-R_{2,f}t)$, $E_{1,f} = \exp(-R_{1,f}t)$ and $E_{1,r} = \exp(-R_{1,r}t)$. Excitation is captured in a matrix $\mathbf{R}_x$ that contains a rotation part for the free pool and a saturation term for the restricted pool, whereas RF phase alternation is

described by $\mathbf{R}_z(\varphi = 180°)$ according to

$$
\mathbf{R}_x(\alpha, t) = \begin{pmatrix} \cos\alpha & \sin\alpha & 0 \\ -\sin\alpha & \cos\alpha & 0 \\ 0 & 0 & e^{-\langle W(\Delta \to 0)\rangle t} \end{pmatrix} \text{ and}
$$

$$
\mathbf{R}_z(\varphi = 180°) = \begin{pmatrix} -1 & 0 & 0 \\ 0 & 1 & 0 \\ 0 & 0 & 1 \end{pmatrix}. \tag{2.7}
$$

The steady state equation can now readily be derived following standard methods [7]. The magnetization directly after the $n^{\text{th}}$ RF pulse is given by $\mathbf{M}_n^+ = \mathbf{R}_x\mathbf{M}_n^-$, where $\mathbf{M}_n^-$ describes the magnetization directly before the $n^{\text{th}}$ RF pulse. The magnetization directly before the $(n + 1)^{\text{st}}$ pulse in case relaxation takes place before exchange thus evolves to

$$
\mathbf{M}_{n+1}^- = \mathbf{A}(\mathbf{E}\mathbf{R}_x\mathbf{M}_n^- + \mathbf{M}_0), \text{ where } \mathbf{M}_0 = \begin{pmatrix} 0 \\ M_{0,f}(1 - E_{1,f}) \\ M_{0,r}(1 - E_{1,r}) \end{pmatrix}. \tag{2.8}
$$

The eigenvalue equation for the steady-state magnetization directly after an RF pulse is of form $\mathbf{M}_{n+1}^- = \mathbf{R}_z\mathbf{M}_n^-$ (here $\mathbf{R}_z$ takes into account alternating RF pulses) to finally yield

$$
\mathbf{M}^+(\infty) = \mathbf{R}_x(\mathbf{I} - \mathbf{R}_z\mathbf{A}\mathbf{E}\mathbf{R}_x)^{-1}\mathbf{A}\mathbf{M}_0 \tag{2.9}
$$

with solution

$$
M_y^+ = M_{0,f}\sin\alpha \frac{(1 - E_{1,f})B + C}{A - BE_{1,f}E_{2,f} - (BE_{1,f} - AE_{2,f})\cos\alpha}, \tag{2.10}
$$

where

$$
\begin{aligned}
A &= 1 + F - f_w E_{1,r}(F + f_k), \\
B &= 1 + f_k(F - f_w E_{1,r}(F + 1)), \\
C &= F(1 - E_{1,r})(1 - f_k), \\
f_k &= \exp[-(k_f + k_r)\text{TR}], \\
f_w &= \exp[-\langle W(\Delta \to 0)\rangle \text{T}_{\text{RF}}], \\
M_{0,f} &= 1, \\
E_{2,f} &= \exp(-R_{2,f}\text{TR}), \\
E_{1,f} &= \exp(-R_{1,f}\text{TR}), \text{ and} \\
E_{1,r} &= \exp(-R_{1,r}\text{TR}).
\end{aligned} \tag{2.11}
$$

It is interesting to note that Eq. (2.10) is of the same form as the well-known single-pool bSSFP steady-state equation (Eq. (2.1)) but shows some additional terms comprising MT related parameters, such as $F$, $k_f$ and the mean saturation rate $\langle W \rangle$. It is thus apparent that Eq. (2.10) converges to Eq. (2.1) in the limit of a vanishing restricted pool, i. e. $\langle W \rangle$, $F$, $k_f$, $k_r$, $E_{1,r} \to 0$, as can be expected from

theoretical considerations. The solution to the two-pool bSSFP signal equation as given by Eqs. (2.10)-(2.11) represents the case where relaxation takes place *before* exchange. For reasons of completeness, it is noteworthy that the case where relaxation takes place *after* exchange yields an almost identical solution as Eqs. (2.10)-(2.11). For the sake of simplicity the following will only consider the former solution (relaxation *before* exchange).

## 2.3  Methods

Experiments and calibrations were performed on a Siemens 1.5 T Avanto system (Siemens Medical Solution, Erlangen, Germany) and all numerical simulations, data analysis and visualization were done in Matlab 2006a (The MathWorks, Inc., Natick, MA).

### 2.3.1  Numerical Simulations

Numerical simulations of the full set of non-simplified ordinary differential equations (ODE) (see Eqs. (2.3a)-(2.3d)) were performed to verify Eq. (2.10) in order to justify the separation of relaxation and exchange processes (see Eq. (2.6)). Therefore, a standard ODE solver was used to simulate the steady-state signal as a function of RF pulse characteristics (flip angle $\alpha$, RF pulse duration $\mathrm{T_{RF}}$), relaxation processes ($T_1$ and $T_2$), fractional pool size ($F$), and exchange properties ($k_f$). For excitation, sinc-shaped RF pulses of variable duration having a time-bandwidth product of 2.7 and one side lobe were used. The mean saturation rate ($\langle W \rangle$) is calculated as a function of $\alpha$ and $\mathrm{T_{RF}}$ according to Eq. (2.2) based on Super-Lorentzian line shapes $G(\Delta)$ being appropriate for the description of tissues [19, 21]:

$$G(\Delta) = \int\limits_0^1 \sqrt{\frac{2}{\pi}} \frac{T_{2,r}}{|3u^2 - 1|} \exp\left[-2\left(\frac{2\pi\Delta T_{2,r}}{3u^2 - 1}\right)^2\right] du. \qquad (2.12)$$

The on-resonance singularity is handled by extrapolating $G(\Delta)$ from about 1 kHz to the asymptotic limit $\Delta \to 0$, yielding $G(0) = 1.4 \cdot 10^{-5}\,\mathrm{s^{-1}}$ [11] for $T_{2,r} = 12\,\mathrm{\mu s}$ [19]. As a result of the uncertainty, no distinction was made between $G(0)$ for white matter and $G(0)$ for gray matter. Possible issues are analyzed and discussed in any detail later in this work. In this framework, the general uncertainty in $R_{1,r}$ [23] is expressed by the fact that $R_{1,r}$ is set equal to $R_{1,f}$. This is in contrast but not so different from the common $R_{1,r} = 1\,\mathrm{s^{-1}}$ assignment.

### 2.3.2  In Vivo Experiments

All experiments were performed in 3D with a sagittal orientation based on a $144 \times 192 \times 192$ matrix yielding 1.3 mm isotropic resolution. Different MT sensitivities in bSSFP can be achieved from a variation of the flip angle ($\alpha$) or the RF pulse duration ($\mathrm{T_{RF}}$) in Eq. (2.10) (Fig. 2.1). However, the signal change is considerably larger with RF pulse elongation as compared to an increase in TR
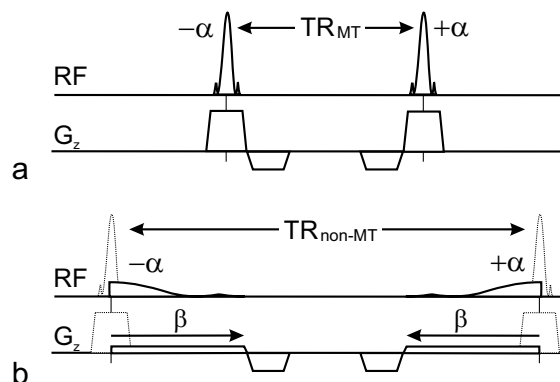
Figure 2.1: BSSFP sequence scheme for exploration of MT effects from RF pulse variation. (a) For short RF pulse durations and minimal repetition time $\text{TR}_{\text{MT}}$ the steady-state signal is strongly attenuated from MT effects. (b) Minimal MT effects can be achieved from a considerable increase in the RF pulse duration (factor $\beta$ leading to an increased repetition time $\text{TR}_{\text{non}-\text{MT}}$), yielding low saturation of the restricted pool protons.

only [12]. From the overall similarity of Eq. (2.10) and (2.1), it is seen that the main two-pool bSSFP signal characteristics rely on the combination $T_2/T_1$ [7]. As a result, reliable $T_1$ or $T_2$ parameter estimation from Eq. (2.10) thus requires an independent determination of either $T_1$ or $T_2$. In summary, the protocol used for quantitative MT parameter estimation consisted of:

1. Two spoiled gradient echo (SPGR) sequences (TR/TE = 9.8 ms/4.77 ms, bandwidth = 140 Hz/Pixel) with flip angles $\alpha_1 = 4°$ and $\alpha_2 = 15°$ for calculation of a $T_{1,f}$ map according to the DESPOT1 method [27, 28].

2. Eight bSSFP sequences with $\alpha = 35°$ (bandwidth = 790 Hz/Pixel) and varying RF pulse durations ($\text{TR}_1/\text{T}_{\text{RF},1} = 2.92\,\text{ms}/0.23\,\text{ms}$, $\text{TR}_2/\text{T}_{\text{RF},2} = 2.99\,\text{ms}/0.3\,\text{ms}$, $\text{TR}_3/\text{T}_{\text{RF},3} = 3.09\,\text{ms}/0.4\,\text{ms}$, $\text{TR}_4/\text{T}_{\text{RF},4} = 3.26\,\text{ms}/0.58\,\text{ms}$, $\text{TR}_5/\text{T}_{\text{RF},5} = 3.53\,\text{ms}/0.84\,\text{ms}$, $\text{TR}_6/\text{T}_{\text{RF},6} = 3.88\,\text{ms}/1.2\,\text{ms}$, $\text{TR}_7/\text{T}_{\text{RF},7} = 4.28\,\text{ms}/1.6\,\text{ms}$, $\text{TR}_8/\text{T}_{\text{RF},8} = 4.78\,\text{ms}/2.1\,\text{ms}$). Minimal $\text{TR}/\text{T}_{\text{RF}}$ values were determined by a compromise between peripheral nerve stimulation as a result of fast gradient switching and upper boundaries in $\alpha$ due to limitations in the SAR. Maximal $\text{TR}/\text{T}_{\text{RF}}$ values were chosen to yield an elongation factor ($\beta$) of the RF pulse of 8-10 (see Fig. 2.1). Minimal TR (irrespective of the RF pulse elongation) maximizes MT [12] and keeps the overall acquisition time minimal.

3. Eight bSSFP sequences with $\text{TR}/\text{T}_{\text{RF}} = 2.99\,\text{ms}/0.27\,\text{ms}$ (bandwidth = 790 Hz/Pixel) and varying flip angles ($\alpha_1 = 5°$, $\alpha_2 = 10°$, $\alpha_3 = 15°$, $\alpha_4 = 20°$, $\alpha_5 = 25°$, $\alpha_6 = 30°$, $\alpha_7 = 35°$, $\alpha_8 = 40°$), which were distributed up to the SAR limit.

4. A multislice (16 slices, 5 mm slice thickness) $B_1$ field map sequence ($64 \times 64$ matrix, 4 mm in plane resolution) using stimulated echoes in a multipulse

sequence ($\alpha-\alpha-\alpha$ analogous to the $\alpha-2\alpha-\alpha$ scheme [29] for the assessment of flip angle deviations.

5. For anatomical reference, an MPRAGE sequence (TR/TE = 1760 ms/ 3.35 ms, inversion time = 906 ms, $\alpha = 7°$, bandwidth = 190 Hz/Pixel) completed the qMTI protocol.

Typically, frequency variations of less than 20 Hz were achieved within the brain by manual shimming to reduce off-resonance sensitivities. Overall qMTI data acquisition was completed within 30 minutes (including DESPOT1: 6 min; bSSFP (varying $\alpha$): 8 min; bSSFP (varying $T_{RF}$): 11 min; $B_1$ map: 2 min; MPRAGE: 3 min). Measurements on healthy volunteers were approved by the local ethics committee. Five acquisitions on the same subject were performed with time-lags of one to three weeks in order to analyze the reproducibility of the method.

### 2.3.3 Data Analysis

The software packages FSL [30] and AFNI [31] were used for the image registration, brain extraction and white (gray) matter segmentation. The effective measured $B_1$ field is expressed as percentage difference from the actual flip angle as set by the system (protocol). From this, effective flip angles were calculated on a pixel-by-pixel base after $B_1$ image registration and data interpolation (FSL) prior to all data evaluations. Longitudinal relaxation time, $T_{1,f}$, was calculated from DESPOT1. The spin-bath model parameters $F$, $k_f$ and $T_{2,f}$ were estimated from a fit of Eq. (2.10) to all 16 bSSFP image acquisitions (pixel-by-pixel), using a global nonlinear least-squares fitting routine. Lastly, MTR maps were calculated from $T_{RF}$ variation ($T_{MT} = T_{RF,1} = 0.23$ ms and $T_{non-MT} = T_{RF,8} = 2.1$ ms) according to MTR = $100 \cdot (S_0 - S_{MT})/S_0$ [%], where $S_0$ and $S_{MT}$ correspond to the signal amplitude measured with $T_{MT}$ and $T_{non-MT}$, respectively [17]. As a result, 3D $T_{1,f}$, $F$, $k_f$, $T_{2,f}$ and MTR parameter maps could be extracted.

## 2.4 Results

### 2.4.1 Validation

Figure 2.2 displays a comparison of the derived two-pool bSSFP steady-state equation (Eq. (2.10)) with numerical simulations of differential equations (2.3a)-(2.3d) for white matter using parameter values from [19]. Within the range of experimentally applied flip angles (see "Methods" section), the analytical solution slightly underestimates simulated values by 1.1 % in maximum (Fig. 2.2 a). In addition, the idealized two-pool bSSFP steady-state signal (Eq. (2.5)) is displayed, where full saturation of the restricted pool protons occurs for all flip angles. As expected, the two-pool bSSFP equation converges to the idealized case only in the limit of large flip angles ($> 100°$).

In earlier work, it was demonstrated that bSSFP shows a strong dependency on TR [11] and especially on the RF pulse duration [12]. The derived two-pool bSSFP signal as a function of $T_{RF}$ (and TR) is displayed in Fig. 2.2 b.
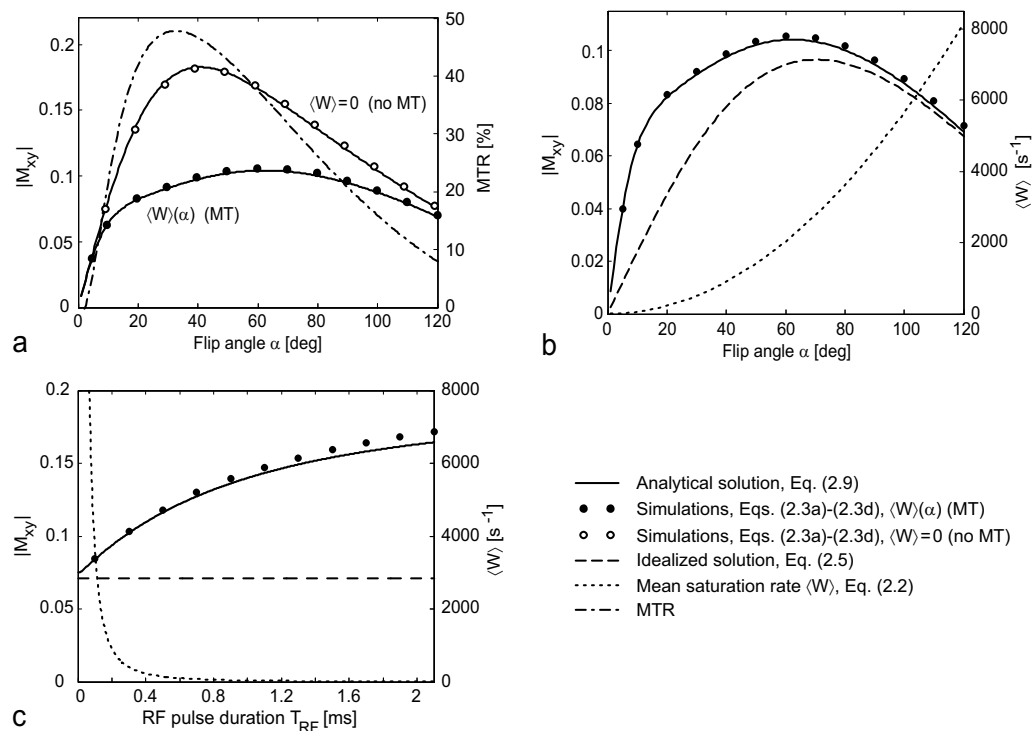
Figure 2.2: Two-pool bSSFP model analysis for white matter using parameters from literature ($T_{1,f} = 585\,\text{ms}$, $T_{2,f} = 81\,\text{ms}$, $F = 0.157$, $k_f = 4.45\,\text{s}^{-1}$, $R_{1,r} = 1\,\text{s}^{-1}$, $T_{2,r} = 12\,\text{s}$ [19]). (a) Transverse magnetization ($M_{xy}$) with and without MT and MTR as a function of flip angle ($\alpha$). (b) Variation of $\alpha$ (TR $= 2.92\,\text{ms}$, $T_{\text{RF}} = 230\,\mu\text{s}$): Excellent correspondence between numerical simulations and the prediction according to the analytical solution of the two-pool bSSFP model is found. The two-pool bSSFP signal equation converges to the idealized case roughly at $\alpha > 100°$, thereby indicating full saturation of restricted pool protons. (c) Variation of $T_{\text{RF}}$ ($\alpha = 35°$): Simulation and solution match for low $T_{\text{RF}}$ but deviate with increasing RF pulse durations.

Simulated RF pulse durations covered a range of $0 < \mathrm{T_{RF}} < 2.1\,\mathrm{ms}$ at a fixed time-bandwidth product of 2.7, with corresponding TR variation between $3\,\mathrm{ms}$ and $5.1\,\mathrm{ms}$. Similar to Fig. 2.2 a, the analytical two-pool model equation slightly underestimates values from full ODE simulations and the discrepancy increases with increasing RF pulse durations. At $\mathrm{T_{RF}} = 2.1\,\mathrm{ms}$ the simulated value exceeds the one deduced from the signal equation by $4.3\,\%$. This is most likely a result of the assumed instantaneous action of the RF pulses; a criteria that becomes more and more falsified with increasing $\mathrm{T_{RF}}$. For short $\mathrm{T_{RF}}$ durations, the situation of infinitely many RF pulses per second is achieved and therefore full saturation occurs ($\langle W \rangle \to \infty$) representing the idealized case.

In summary, good agreement between the analytical description of the two-pool bSSFP model (Eqs. (2.10)-(2.11)) and the numerical simulations based on the full, i.e. non-simplified, ODEs (Eqs. (2.3a)-(2.3d)) was found. The slight underestimation of the steady-state signal by Eq. (2.10) as compared to the numerical simulations is most likely due to neglected $T_2$ effects during excitation processes, as indicated by the increasing discrepancy with increasing RF pulse durations.

### 2.4.2  Quantitative Magnetization Transfer Imaging (qMTI)

Quantitative MT parameter evaluation based on Eqs. (2.10)-(2.11) is exemplarily displayed in Fig. 2.3. After brain extraction and registration, Eq. (2.10) was fitted pixel-by-pixel to bSSFP signal intensities. Figures 2.3 a and 2.3 b display the signal dependencies on RF pulse duration (and corresponding increase in TR) and flip angle for white and gray matter, respectively. The global fits (i.e. both flip angle and $\mathrm{T_{RF}}$ varied data sets share the same MT model parameters) yield parameter estimates for the fractional pool size $F$, the exchange rate $k_f$ and the relaxation time of the free pool $T_{2,f}$. Since the fractional pool size is correlated with myelin [22], $F$ shows higher values in white as compared to gray matter.

Figures 2.4 and 2.5 display the results from qMTI using the two-pool bSSFP model in normal appearing human brain. In Fig. 2.4, besides the anatomical reference, axial, sagittal and coronal slices were shown for $T_{1,f}$ (based on DESPOT1) and $T_{2,f}$ (two-pool model analysis), whereas Fig. 2.5 displays parameter maps for $F$ and $k_f$. An MTR evaluation completes the spectrum of quantitative MT image analysis. Generally, MT related model parameters (Fig. 2.5) feature a highly similar contrast with good discrimination between gray and white matter structures. MT parameter estimates for a selection of regions of interest (ROI, see Fig. 2.4) in white and gray matter structures and were compared to those derived from a standard qMTI model [19]. The results are summarized in Tables 2.1 and 2.2.

In general, good correspondence between the two-pool bSSFP and common qMTI models [19–21, 23, 25, 26, 32] is found. In normal appearing brain, the two-pool bSSFP model yields $F$ values that correlate well for gray matter, whereas for white matter $F$ is about $8\,\%$ lower as compared to literature [19]. Similarly, excellent agreement in $k_f$ for both, i.e. white and gray matter, is found, whereas for $T_{1,f}$ and $T_{2,f}$ discrepancies of up to $30\,\%$ were observed in white matter; most probably due to sequence specific weighting [19]. Derivation of quantitative MT
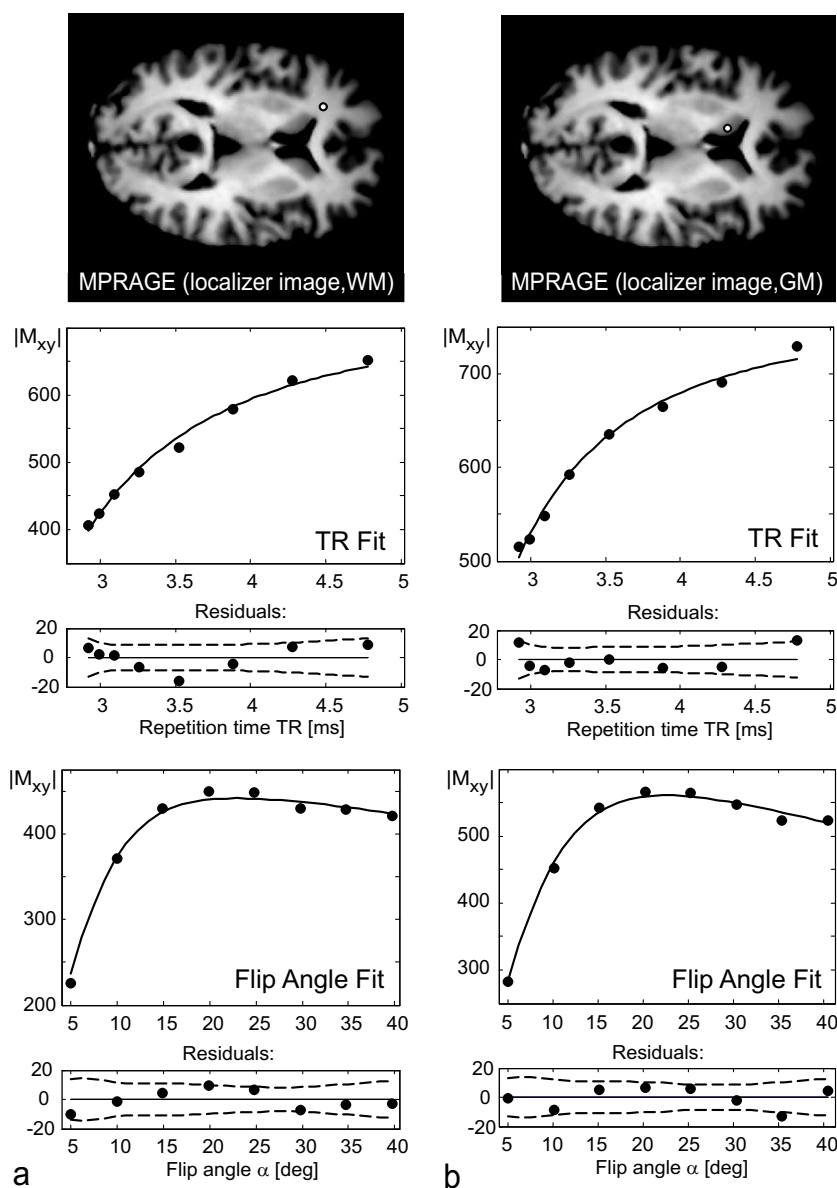
Figure 2.3: Introductory example to the two-pool bSSFP model analysis showing an MT parameter estimation from a single voxel $(1.3 \times 1.3 \times 1.3\,\mathrm{mm}^3)$ for white (a) and gray (b) matter in human brain, as indicated in the axial anatomical reference (MPRAGE image). Nonlinear least squares fitting of Eqs. (2.10)-(2.11) to all 16 bSSFP image acquisitions (as described in "Methods" section), yields the spin-bath model parameters $F$, $k_f$ and $T_{2,f}$. Single pixel estimate for frontal lobes: $F = 15.5 \pm 5.3\,\%$, $k_f = 4.41 \pm 1.85\,\mathrm{s}^{-1}$ and $T_{2,f} = 40.6 \pm 6.2\,\mathrm{ms}$, and for caudate nucleus: $F = 6.0 \pm 1.7\,\%$, $k_f = 2.29 \pm 0.95\,\mathrm{s}^{-1}$ and $T_{2,f} = 59.0 \pm 5.9\,\mathrm{ms}$. Additionally, fitting residuals in units of $M_{xy}$ and 95 % confidence interval of the predicted data are shown.
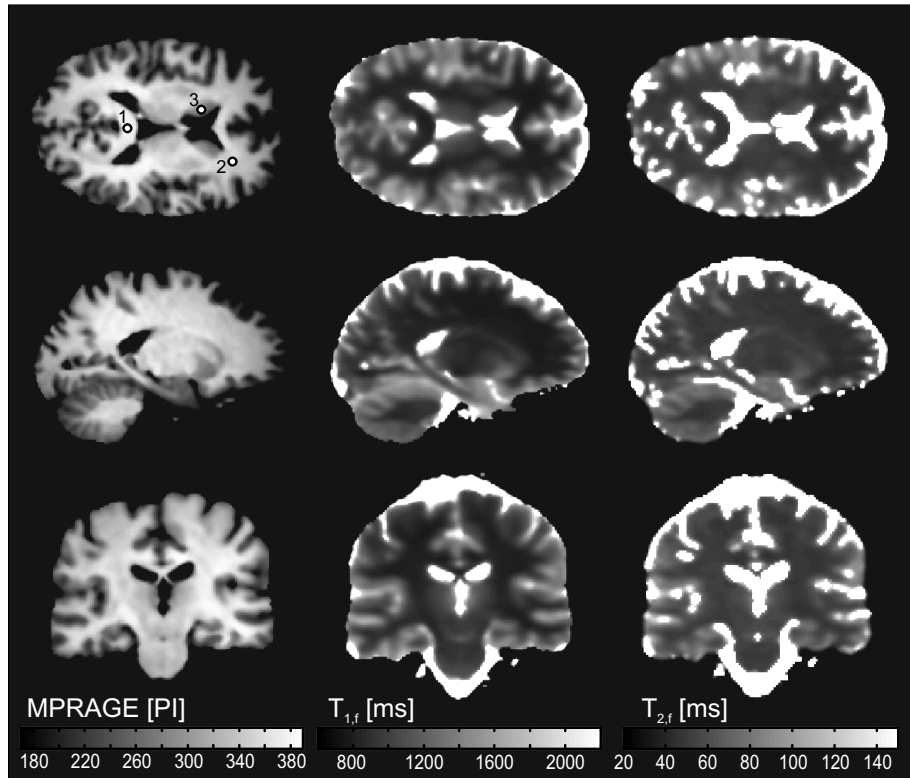
Figure 2.4: Axial, sagittal and coronal sample images (1.3 mm isotropic resolution) of a healthy volunteer displaying the results of whole brain MT parameter estimation from a two-pool bSSFP signal analysis. Regions of interest (1: corpus callosum splenium; 2: frontal lobes; 3: caudate nucleus) are defined in the axial anatomical reference (MPRAGE), and corresponding results are listed in Tables 2.1 and 2.2. $T_{1,f}$ maps were derived from DESPOT1, whereas $T_{2,f}$ maps were derived from fitting the two-pool bSSFP signal equation to a series of 3D bSSFP image acquisition, as illustratively displayed in Fig. 2.3.
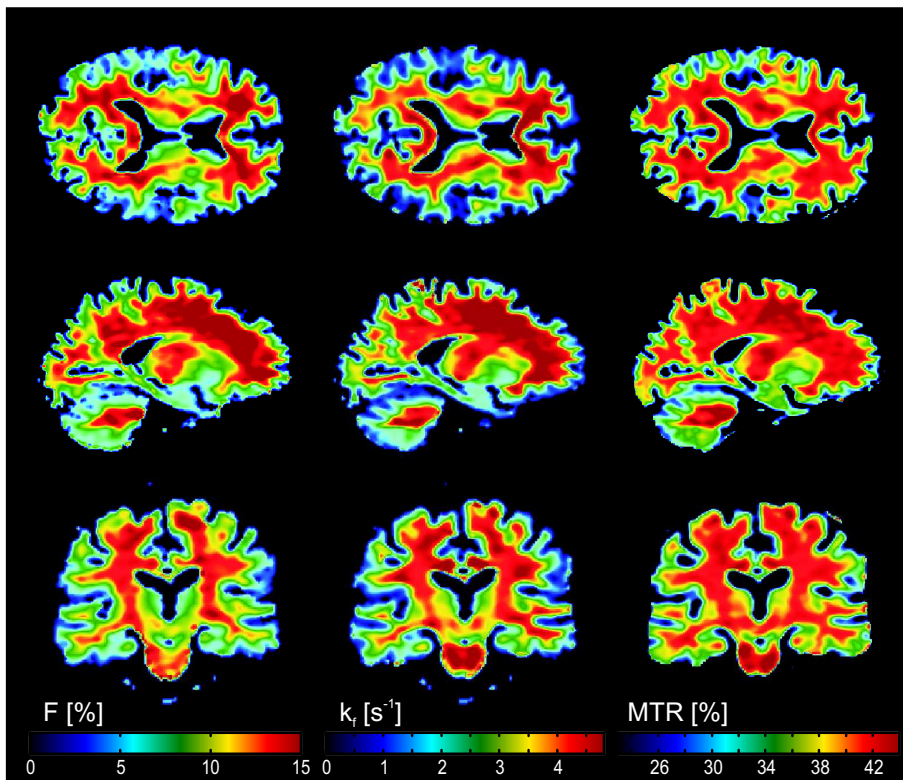
Figure 2.5: Axial, sagittal and coronal sample images of a healthy volunteer showing 3D 1.3 mm isotropic high-resolution MT parameter estimates for the restricted pool fraction $F$ and the magnetization exchange rate $k_f$, as derived from two-pool bSSFP model fitting (see Fig. 2.3). In addition, an MTR image is derived from two bSSFP image acquisitions ($TR_1$ and $TR_8$, see "Methods" section and [12]). In general, for normal appearing human brain, high correlation between all MT related parameters is observed.

parameters was well reproducible: standard deviations from five measurements on the same healthy volunteer were $1.3\,\%$ for $F$, $2.1\,\%$ for $k_f$, $1.5\,\%$ for $T_{1,f}$ and $3\,\%$ for $T_{2,f}$.

Table 2.1: Quantitative MT model parameters in white matter derived from two-pool bSSFP model fitting.

| | $WM^d$ | $WM^e$ | $WM^f$ | $WM^g$ |
|---|---|---|---|---|
| $T_{1,f}\,[\text{ms}]^a$ | $759 \pm 18$ | $733 \pm 19$ | $779 \pm 75$ | $556$ |
| $T_{2,f}\,[\text{ms}]^b$ | $43 \pm 1$ | $40 \pm 2$ | $45 \pm 4$ | $34$ |
| $F\,[\%]^b$ | $14.4 \pm 0.6$ | $14.5 \pm 0.9$ | $13.2 \pm 1.9$ | $15.7$ |
| $k_f\,[\text{s}^{-1}]^b$ | $4.6 \pm 0.2$ | $4.5 \pm 0.2$ | $4.3 \pm 0.6$ | $4.5$ |
| $\text{MTR}\,[\text{s}^{-1}]^c$ | $42.5 \pm 0.6$ | $41.7 \pm 0.6$ | $41.7 \pm 2.1$ | |

[a]Estimation is based on DESPOT1 [27].
[b]Estimation is based on two-pool bSSFP model fitting (Eqs. (2.10)-(2.11)).
[c]MTR values derived from bSSFP $TR_8$ and $TR_1$ measurements (see Methods section).
[d]Corpus callosum splenium (ROI 1, Fig. 2.4).
[e]Frontal lobes (ROI 2, Fig. 2.4).
[f]Median from whole brain white matter segmentation [30].
[g]Estimates from reference [19].

Table 2.2: Quantitative MT model parameters in gray matter derived from two-pool bSSFP model fitting.

| | $GM^d$ | $GM^e$ | $GM^f$ |
|---|---|---|---|
| $T_{1,f}\,[\text{ms}]^a$ | $1087 \pm 70$ | $1211 \pm 269$ | $1042$ |
| $T_{2,f}\,[\text{ms}]^b$ | $59 \pm 3$ | $71 \pm 28$ | $56$ |
| $F\,[\%]^b$ | $6.5 \pm 0.9$ | $6.2 \pm 2.2$ | $6.4$ |
| $k_f\,[\text{s}^{-1}]^b$ | $2.3 \pm 0.4$ | $1.8 \pm 0.7$ | $2.3$ |
| $\text{MTR}\,[\text{s}^{-1}]^c$ | $32.8 \pm 2$ | $34 \pm 6.2$ | |

[a]Estimation is based on DESPOT1 [27].
[b]Estimation is based on two-pool bSSFP model fitting (Eqs. (2.10)-(2.11)).
[c]MTR values derived from bSSFP $TR_8$ and $TR_1$ measurements (see Methods section).
[d]Caudate nucleus (ROI 3, Fig. 2.3).
[e]Median from whole brain gray matter segmentation [30].
[f]Estimates from reference [19].

As for many other quantitative MR methods, care has to be taken on the actual $B_1$ field achieved. The effect of $B_1$ correction on the parameters $F$ and $k_f$ is demonstrated in Fig. 2.6. Whereas $k_f$ is quite robust against $B_1$-field errors, variation in $F$ produced by $B_1$ variation might be quite severe. In summary, it is demonstrated that whole brain high resolution qMTI parameter maps can be achieved within less than 30 minutes.
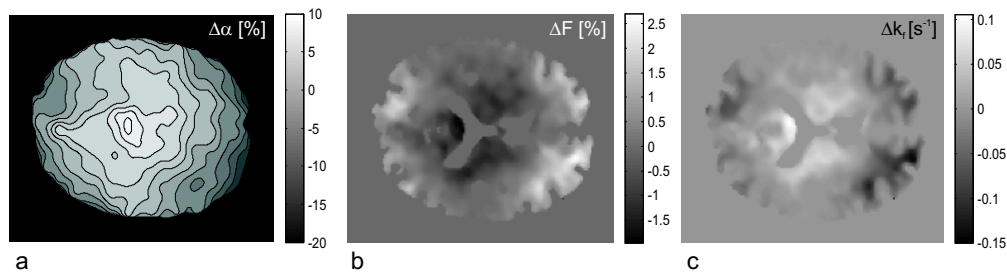
Figure 2.6: Effect of $B_1$-field inhomogeneity correction on MT parameter estimates from two-pool model bSSFP fitting. (a) Axial sample image of the measured $B_1$-field, reported as percentage flip angle deviation. Difference in $F$ (b) and $k_f$ (c) parameter estimates from $B_1$ corrected and uncorrected two-pool bSSFP model fitting. Flip angle deviations have a significant impact on $F$, whereas only subtle modifications can be observed for $k_f$.

## 2.5  Discussion

Commonly, bSSFP requires minimal TR to reduce off-resonance related signal variations that become typically severe for frequencies outside the range of about $2/(3\text{TR})$ [33]. Since MT effects are partially explored in the two-pool bSSFP model from $T_\text{RF}$ and thus TR variation (see Fig. 2.2 in the "Theory" section, qMTI protocol setup in the "Methods" section, and Fig. 2.3 in the "Results" section), some care has to be taken on possible issues that may arise from off-resonance effects.

Numerical simulations of the two-pool model as a function of the dephasing within TR are displayed in Fig. 2.7 a for varying $T_\text{RF}$ and in Fig. 2.7 c for varying $\alpha$. The arrows in the plots indicate the achievable signal range from $T_\text{RF}$ (and TR) and $\alpha$ variation, respectively (see "In Vivo Experiments" in the "Methods" section). Very limited signal deviations are observed for $\varphi \leq 60°$ from the ideal on-resonance signal modulation within the experimentally varied $T_\text{RF}$ range (Fig. 2.7 b), as a result of the near optimal flip angle setting $(\alpha_{opt} \approx \cos^{-1}\left[(\epsilon - 1)/(\epsilon + 1)\right], \epsilon = T_1/T_2$, see Ref. [7]). Likewise, signal deviations are negligible for $\varphi \leq 30°$ and moderate for $\varphi \leq 60°$ within the experimentally varied $\alpha$ range (Fig. 2.7 d). Sensitivity to off-resonances, however, is increased for $\alpha$ (Fig. 2.7 c) as compared to $T_\text{RF}$ (Fig. 2.7 a) variation, since bSSFP's frequency response becomes more and more M-shaped with diverging $\alpha$ from $\alpha_{opt}$ ($\alpha < \alpha_{opt}$). Therefore, $\alpha$-based bSSFP signal sampling should be constrained to minimal and constant TR protocol settings. In contrast, constant TR-based signal sampling would require the use the longest TR within the $T_\text{RF}$ sweep. Using minimal rather than constant TR for any $T_\text{RF}$ not only reduces overall data acquisition times, but also minimizes off-resonance related signal deviations in the short $T_\text{RF}$ regime (see Fig. 2.7 b). From this, and quite generally, minimal TR settings were used for all bSSFP measurements.

In summary, off-resonances have a negligible impact on the bSSFP signal analysis within $\pm 1/(12\,\text{TR})$ ($< 1\,\%$) and are low within $\pm 1/(6\,\text{TR})$ ($< 5\,\%$).
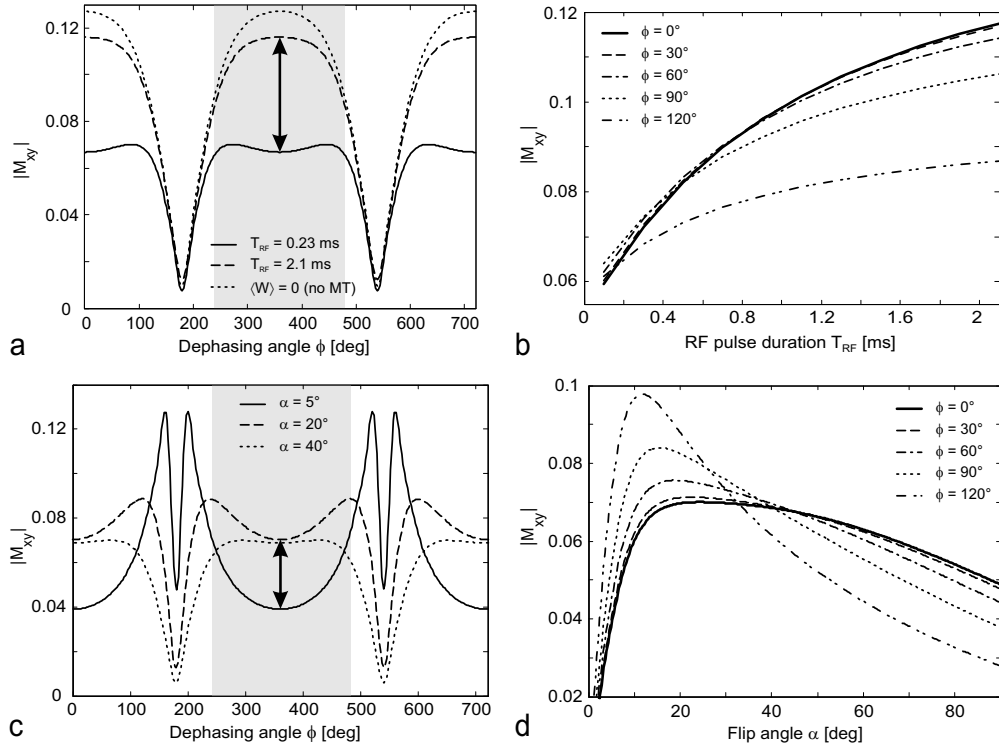
Figure 2.7: Off-resonance sensitivity of two-pool bSSFP parameter estimation, simulated for corpus callosum splenium (see Table 2.1). (a) Frequency response ($\alpha = 35°$) for the completely unsaturated case ($\langle W \rangle = 0$) and for the range of accessible saturations rates from $T_{RF}$ variation (see Eq. (2.2) and "Material" section) as indicated by the arrow. (b) Corresponding signal variation within the pass-band region ($\pm 1/(3\,TR)$; see shaded area in (a)) from $T_{RF}$ variation (see also Fig. 2.2 c). Very limited signal deviations ($< 5\,\%$) from the ideal on-resonance behavior are observed for dephasing angles $\varphi < 60°$. (c) BSSFP frequency response given for the range of applied flip angles (indicated by the arrow) using short RF pulses ($T_{RF} = 2.99\,\text{ms}$, $T_{RF} = 270\,\mu\text{s}$. (d) Corresponding signal variation as achieved in the $\alpha$-varied experiment within the pass-band region (see also Fig. 2.2 c). Deviations from the ideal case are negligible for $\varphi \leq 30°$ ($< 2.5\,\%$) and moderate for $\varphi \leq 60°$ ($< 10\,\%$).

This justifies the formal description of the two-pool bSSFP model according to the derived on-resonance signal equations (Eqs. (2.10)-(2.11)) within an off-resonance related frequency variation of about $\pm 1/(6\,\mathrm{TR})$. Typically, field variations of less than $20\,\mathrm{Hz}$ were achieved from manual shim corresponding to about $\pm 1/(10\,\mathrm{TR})$ for the longest TR used ($\mathrm{TR}_8 < 5\,\mathrm{ms}$). As a result, derivation of MT parameters from two-pool bSSFP signal analysis (Eqs. (2.10)-(2.11)) should not be falsified from off-resonance related precession.

The most obvious difference between bSSFP MT and common qMTI methods [19–21, 23, 25, 26, 32] is the RF irradiation concept. Although MT effects increase with smaller frequency offsets from the center resonance [16], undesired "bleed over", i.e. direct saturation of free pool protons (direct effect), may cause a significant reduction in the MT effect [25] that discouraged the use of binomial on-resonance irradiation concepts. This is in contrast with bSSFP-based qMTI, where excitation and saturation processes are fused together and where the direct effect is per se responsible and needed for the achievement of a dynamic equilibrium state. Since RF pulses are played out on-resonant, the absorption line shape $G(\Delta)$ (see Eq. (2.12)) can only be sampled at one point, i.e. at on-resonance. As a result, two-pool bSSFP model fitting leads to vague estimations of $T_{2,r}$; similar to what is observed in standard qMTI models. In contrast to the common GRE framework, where $R_{1,r}$ is set equal to one [23], the bSSFP framework does not specify $R_{1,r}$ and $R_{2,r}$. However, the fractional pool size $F$ seems to have the highest biological sensitivity and specificity of all MT-related parameters since it is directly associated with myelination [15, 22], whereas $T_{2,r}$ only provides very limited contrast between white and gray matter. In the following, $G(0)$ and thus $R_{2,r}$ sensitivities of MT parameter estimation is investigated.

Especially the ambiguity in the handling of the singularity of the Super-Lorentzian line shape function $G(\Delta)$ at $\Delta \to 0$ (Fig. 2.8 a) has a strong impact on MT parameter estimation (Figs. 2.8 b and 2.8 c), since it determines the mean saturation rate $\langle W \rangle$ of restricted pool protons (see Eq. (2.2)). For $F$ and $k_f$ sensitivity analysis, $G(0)$ variation was centered around the assumed value of $1.4 \cdot 10^{-5}\,\mathrm{s}^{-1}$ (see the Methods section) with lower bounds given by Lorentzian or Gaussian line shapes. Whereas $k_f$ shows only limited sensitivity, the fractional pool size $F$ undergoes substantial variation (about $15\,\%$ - $20\,\%$ for a change in $G(0)$ by $15\,\%$). The marginal discrepancy in $F$ values between common and bSSFP qMTI ($< 8\,\%$, see Tables 2.1 and 2.2) not only indicates a proper estimate for $G(0)$, but also reflects the arising ambiguity in its exact value, since residual small deviations can, in principle, easily be removed by a small change of $G(0)$. Equal line shape functions were assumed for gray and white matter from the high similarities in $T_{2,r}$ [19] and uncertainties at $\Delta \to 0$, however, distinct $G(0)$ for white matter and gray matter can, in principle, be taken into consideration.

Compared to common GRE methods using MT sensitizing preparation pulses, bSSFP qMTI provides high resolution 3D imaging within clinically applicable acquisition times. Standard multi-slice imaging with $0.9 \times 1.9 \times 5\,\mathrm{mm}^3$ resolution (one $T_1$ and 10 MT acquisitions) is completed within 30 minutes [20], whereas 3D acquisitions ($1 \times 2 \times 5\,\mathrm{mm}^3$ resolution) are completed within 20 minutes [32]. However, $B_1$-field maps were acquired prospectively and were not included in the
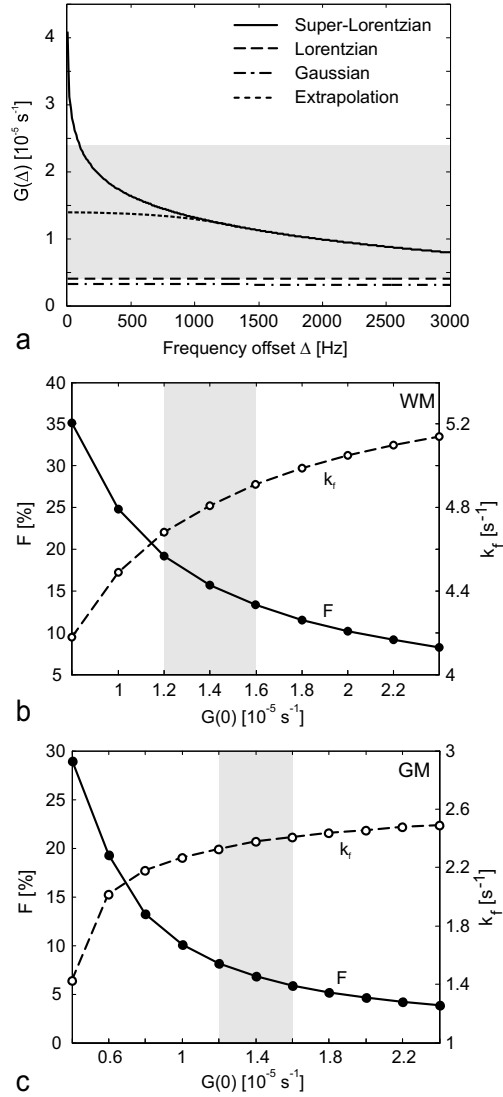
Figure 2.8: Frequency dependence of various absorption lineshapes as commonly used with MT models. Super-Lorentzian lineshapes have been suggested as being appropriate for the description of tissues and the singularity at on-resonance was handled by extrapolation to the asymptotic limit $\Delta \to 0$ ($G(0) = 1.4 \cdot 10^{-5}\,\mathrm{s}^{-1}$). Dependence of $F$ and $k_f$ for a range of $G(0)$ values (see gray shaded area in (a)) for white (b) and gray matter (c) as given in Tables 2.1 and 2.2 for the frontal lobe and caudate nucleus.

acquisition times. For a comparable 1.3 mm isotropic resolution, scan times of common qMTI methods extend to more than 1 hour. This is in contrast to the proposed bSSFP qMTI framework, where the total acquisition time is 30 minutes (i. e., 25 minutes without the anatomical reference scan and the $B_1$-field map). Using common 3D acceleration techniques, such as parallel imaging or partial Fourier, qMTI data collection can easily be reduced to 10-15 minutes. Furthermore, SNR for bSSFP is considerably increased as compared to GRE [32] and partial volume effects are drastically reduced from high resolution 3D imaging. Residual partial volume effects are directly linked with the steady states constituting the voxel signal. Gray and white matter feature a comparable bSSFP signal [11], and thus parameter estimates are averaged according to their partial volume fractions, whereas even small fractions of cerebrospinal fluid (CSF) accentuate the liquidity in the voxel and lead to an underestimation of gray or white matter content.

In summary, derivation of quantitative MT parameters, such as the fractional pool size $F$ and the magnetization exchange rate $k_f$, was demonstrated for normal appearing human brain from two-pool bSSFP model analysis. Several issues have been identified and were analyzed that may have a strong impact on the overall quality of qMTI model analysis, such as off-resonances, $B_1$-field inhomogeneity or absorption lineshape properties at on-resonance. Similar to standard methods, $R_{1,r}$ could not be determined from large fitting uncertainties, but was deliberately identified with $R_{1,f}$ ($R_{1,r} = R_{1,f}$). Additionally, $R_{1,f}$ was measured using DESPOT1, as a result of the intrinsic $T_2/T_1$ contrast of bSSFP. In contrast to common qMTI models, $T_{2,r}$ could not be determined from the proposed two-pool bSSFP model. Despite this possible deficiency, bSSFP-based qMTI delivers an excellent new framework meeting many of the desired sequence optimizations (such as resolution, brain coverage, and clinically feasible acquisition times) to challenge the quest for the biological significance and diagnostic relevance of quantitative MT parameters (such as $F$ or $k_f$). A further reduction in total acquisition time might be achieved by an optimization of the $T_{RF}$, $\alpha$ parameter sets.


## 2.6   Conclusion

A new quantitative MT method using bSSFP was introduced. Based on the observation that the ordinary bSSFP signal equation fails to adequately describe its steady-state behavior in tissues, a modified signal equation based on a binary spin-bath model was derived taking into account MT effects. Using this new model of bSSFP signal formation, quantitative MT parameters, such as the fractional pool size, corresponding magnetization exchange rates and relaxation times could be deduced from human brain. Since bSSFP-based MT model parameters show high correlation to those derived from commonly used gradient echo sequences, bSSFP may offer great potential towards clinically feasible qMTI. Especially the short acquisition times in combination with high signal-to-noise ratios allow for the acquisition of reproducible isotropic and high resolution quantitative

MT maps, as for the human brain, within reasonable acquisition times.

# References

[1] H.Y. Carr. Steady-State Free Precession in Nuclear Magnetic Resonance. *Phys. Rev.*, 112(5):1693–1701, 1958.

[2] A Oppelt, R Graumann, H Barfuss, H. Fischer, W Hartl, and W Schajor. FISP: Eine Neue Schnelle Pulssequenz Für Die Kernspintomographie. *Electromedia*, 54:15–18, 1986.

[3] K. Scheffler and S. Lehnhardt. Principles and Applications of Balanced SSFP Techniques. *Eur Radiol*, 13(11):2409–18, 2003.

[4] V. S. Deshpande and D. Li. Contrast-Enhanced Coronary Artery Imaging Using 3D TrueFISP. *Magn Reson Med*, 50(3):570–7, 2003.

[5] H. Thiele, E. Nagel, I. Paetsch, B. Schnackenburg, A. Bornstedt, M. Kouwenhoven, A. Wahl, G. Schuler, and E. Fleck. Functional Cardiac MR Imaging with Steady-State Free Precession (SSFP) Significantly Improves Endocardial Border Delineation without Contrast Agents. *J Magn Reson Imaging*, 14(4):362–7, 2001.

[6] R Freeman and HDW Hill. Phase and Intensity Anomalies in Fourier Transform NMR. *J Magn Reson*, 4:366–383, 1971.

[7] EM Haacke, RW Brown, MR Thompson, and R. Venkatesan. *Magnetic Resonance Imaging: Physical Principles and Sequence Design*. Wiley, 1999.

[8] P. Schmitt, M. A. Griswold, P. M. Jakob, M. Kotas, V. Gulani, M. Flentje, and A. Haase. Inversion Recovery TrueFISP: Quantification of T(1), T(2), and Spin Density. *Magn Reson Med*, 51(4):661–7, 2004.

[9] T. Y. Huang, I. J. Huang, C. Y. Chen, K. Scheffler, H. W. Chung, and H. C. Cheng. Are TrueFISP Images T2/T1-Weighted? *Magn Reson Med*, 48(4):684–8, 2002.

[10] K. Scheffler and J. Hennig. T(1) Quantification with Inversion Recovery TrueFISP. *Magn Reson Med*, 45(4):720–3, 2001.

[11] O. Bieri and K. Scheffler. On the Origin of Apparent Low Tissue Signals in Balanced SSFP. *Magn Reson Med*, 56(5):1067–74, 2006.

[12] O. Bieri and K. Scheffler. Optimized Balanced Steady-State Free Precession Magnetization Transfer Imaging. *Magn Reson Med*, 58(3):511–8, 2007.

[13] S. D. Wolff and R. S. Balaban. Magnetization Transfer Imaging: Practical Aspects and Clinical Applications. *Radiology*, 192(3):593–9, 1994.

[14] R. M. Henkelman, G. J. Stanisz, and S. J. Graham. Magnetization Transfer in MRI: A Review. *NMR Biomed*, 14(2):57–64, 2001.

[15] P. Tofts. *Quantitative MRI of the Brain*. Wiley, 2003.

[16] S. D. Wolff and R. S. Balaban. Magnetization Transfer Contrast (MTC) and Tissue Water Proton Relaxation in Vivo. *Magn Reson Med*, 10(1):135–44, 1989.

[17] V. Dousset, R. I. Grossman, K. N. Ramer, M. D. Schnall, L. H. Young, F. Gonzalez-Scarano, E. Lavi, and J. A. Cohen. Experimental Allergic Encephalomyelitis and Multiple Sclerosis: Lesion Characterization with Magnetization Transfer Imaging. *Radiology*, 182(2):483–91, 1992.

[18] P. S. Tofts, S. C. Steens, M. Cercignani, F. Admiraal-Behloul, P. A. Hofman, M. J. van Osch, W. M. Teeuwisse, D. J. Tozer, J. H. van Waesberghe, R. Yeung, G. J. Barker, and M. A. van Buchem. Sources of Variation in Multi-Centre Brain MTR Histogram Studies: Body-Coil Transmission Eliminates Inter-Centre Differences. *Magma*, 19(4):209–22, 2006.

[19] J. G. Sled and G. B. Pike. Quantitative Imaging of Magnetization Transfer Exchange and Relaxation Properties in Vivo Using MRI. *Magn Reson Med*, 46(5):923–31, 2001.

[20] A. Ramani, C. Dalton, D. H. Miller, P. S. Tofts, and G. J. Barker. Precise Estimate of Fundamental in-Vivo MT Parameters in Human Brain in Clinically Feasible Times. *Magn Reson Imaging*, 20(10):721–31, 2002.

[21] C. Morrison and R. M. Henkelman. A Model for Magnetization Transfer in Tissues. *Magn Reson Med*, 33(4):475–82, 1995.

[22] G. R. Davies, A. Ramani, C. M. Dalton, D. J. Tozer, C. A. Wheeler-Kingshott, G. J. Barker, A. J. Thompson, D. H. Miller, and P. S. Tofts. Preliminary Magnetic Resonance Study of the Macromolecular Proton Fraction in White Matter: A Potential Marker of Myelin? *Mult Scler*, 9(3): 246–9, 2003.

[23] R. M. Henkelman, X. Huang, Q. S. Xiang, G. J. Stanisz, S. D. Swanson, and M. J. Bronskill. Quantitative Interpretation of Magnetization Transfer. *Magn Reson Med*, 29(6):759–66, 1993.

[24] R. Dharmakumar, J. Hong, J. H. Brittain, D. B. Plewes, and G. A. Wright. Oxygen-Sensitive Contrast in Blood for Steady-State Free Precession Imaging. *Magn Reson Med*, 53(3):574–83, 2005.

[25] S. J. Graham and R. M. Henkelman. Understanding Pulsed Magnetization Transfer. *J Magn Reson Imaging*, 7(5):903–12, 1997.

[26] G. B. Pike. Pulsed Magnetization Transfer Contrast in Gradient Echo Imaging: A Two-Pool Analytic Description of Signal Response. *Magn Reson Med*, 36(1):95–103, 1996.

[27] S. C. Deoni, T. M. Peters, and B. K. Rutt. High-Resolution T1 and T2 Mapping of the Brain in a Clinically Acceptable Time with DESPOT1 and DESPOT2. *Magn Reson Med*, 53(1):237–41, 2005.

[28] J. Homer and J.K. Roberts. Conditions for the Driven Equilibrium Single Pulse Observation of Spin-Lattice Relaxation Times. *J Magn Reson*, 74: 424–432, 1987.

[29] S. Akoka, F. Franconi, F. Seguin, and A. Le Pape. Radiofrequency Map of an NMR Coil by Imaging. *Magn Reson Imaging*, 11(3):437–41, 1993.

[30] S. M. Smith, M. Jenkinson, M. W. Woolrich, C. F. Beckmann, T. E. Behrens, H. Johansen-Berg, P. R. Bannister, M. De Luca, I. Drobnjak, D. E. Flitney, R. K. Niazy, J. Saunders, J. Vickers, Y. Zhang, N. De Stefano, J. M. Brady, and P. M. Matthews. Advances in Functional and Structural MR Image Analysis and Implementation as FSL. *Neuroimage*, 23 Suppl 1:S208–19, 2004.

[31] R. W. Cox. AFNI: Software for Analysis and Visualization of Functional Magnetic Resonance Neuroimages. *Comput Biomed Res*, 29(3):162–73, 1996.

[32] M. Cercignani, M. R. Symms, K. Schmierer, P. A. Boulby, D. J. Tozer, M. Ron, P. S. Tofts, and G. J. Barker. Three-Dimensional Quantitative Magnetisation Transfer Imaging of the Human Brain. *Neuroimage*, 27(2): 436–41, 2005.

[33] K. Scheffler, O. Heid, and J. Hennig. Magnetization Preparation During the Steady State: Fat-Saturated 3D TrueFISP. *Magn Reson Med*, 45(6): 1075–80, 2001.

# Chapter 3

# Possible Adaptations of Quantitative Magnetization Transfer Imaging Using Balanced SSFP

## 3.1 Protocol Shortening and Phase-Cycling

### 3.1.1 Introduction

In tissues, the signal of balanced steady-state free precession (bSSFP) is strongly dependent on magnetization transfer (MT) [1]. Based on an extended bSSFP signal equation, taking MT effects fully into account, quantitative MT imaging (qMTI) parameters can be estimated in human brain [2]. So far, the flip angle as well as the pulse duration dependency of the bSSFP signal was sampled in order to estimate the bound proton fraction and corresponding magnetization exchange rates.

In this work, an accelerated measurement protocol based on pulse elongation only is explored to facilitate the clinical use of bSSFP-based qMTI. Using common 3D acceleration techniques, high-resolution volumetric maps of MT parameters can be generated within less than 10 minutes. This setup can be widely used to extend standard neurological protocols. On the other hand, scan time reduction of the modified protocol offers the possibility to overcome limitations arising from the off-resonance sensitivity of bSSFP.

Balanced SSFP imaging is limited by its high sensitivity to local field variation [3–5]. Characteristic signal nulls, also known as banding artifacts, become severe for off-resonance frequencies outside the range of about $\pm 2/(3\,\mathrm{TR})$ [6]. This should typically not cause problems for qMTI in the brain at 1.5 T [2], but might become an issue for specific regions near the sinuses, in other types of tissue, such as muscle and cartilage, and at higher field strengths. Several methods based on a combination of multiple bSSFP acquisitions with different RF phase increments have been proposed to reduce banding artifacts [7–12]. A combination of phase-cycled images is used to obtain quantitative MT maps even in brain regions with high susceptibility variation.

### 3.1.2 Methods

Quantitative MT parameters can in principle be derived from a two-pool bSSFP signal equation by measuring the signal dependence on the RF pulse duration ($\mathrm{T_{RF}}$) as well as the flip angle ($\alpha$) dependence [2]. For small flip angles, off-resonance induced banding artifacts can not effectively be reduced due to the thin pass-band. However, a preceding $T_2$ calculation makes it possible to estimate the bound proton fraction $F$ and the exchange rate $k_f$ from RF pulse elongation only (at a constant flip angle). Thereby, the acquisition time is reduced by one third and phase-cycled acquisitions are enabled.

---

This section has partly been presented as:

- M. Gloor, K. Scheffler, O. Bieri. Quantitative Magnetization Transfer Imaging of the Brain within 10 Minutes. ISMRM White Matter Workshop, Krakow, 2008.

- M. Gloor, K. Scheffler, O. Bieri. Accelerated Quantitative Magnetization Transfer Imaging Using Balanced SSFP. Proceedings of the 25th Annual Meeting ESMRMB, Valencia, 2008.

Experiments and calibrations were performed on a Siemens 1.5 T Avanto system (Siemens Medical Solution, Erlangen, Germany). Images were acquired in 3D with a sagittal orientation based on a $144 \times 192 \times 192$ matrix yielding 1.3 mm isotropic resolution. A multislice (16 slices, 5 mm slice thickness) $B_1$ field map sequence ($64 \times 64$ matrix, 4 mm in plane resolution) using stimulated echoes in a multipulse sequence [13] was acquired for the assessment of flip angle deviations. Relaxation times of the free pool $T_{1,f}$ and $T_{2,f}$ were calculated from two spoiled gradient echo (SPGR) sequences (TR/TE = 9.8 ms/4.77 ms, bandwidth = 140 Hz/Pixel, $\alpha_1 = 3°$ and $\alpha_2 = 17°$) according to the DESPOT1 method and from two bSSFP sequences (TR = 4.55 ms, bandwidth = 790 Hz/Pixel, $\alpha_1 = 15°$ and $\alpha_2 = 35°$) according to the DESPOT2 method, respectively [14]. The MT-bSSFP equation was fitted pixelwise to a set of 8 bSSFP sequences with $\alpha = 35°$ (bandwidth = 790 Hz/Pixel) and varying RF pulse durations $T_{RF}$ ($TR_1/T_{RF,1}$ = 2.68 ms/0.23 ms, ..., $TR_8/T_{RF,8}$ = 4.55 ms/2.1 ms) to yield $F$ and $k_f$. Data acquisition time for the qMTI protocol without phase-cycling was less than 10 minutes.

Image registration was performed using FSL [15] and AFNI [16]. Images with an RF phase increment $\vartheta = 180°$ and $\vartheta = 0°$, respectively, were combined using three different approaches. In sum-of-squares bSSFP, each reconstructed image is squared, the results are summed, and the square root is taken [11]. In maximum-intensity bSSFP, the combined image is formed by assigning each pixel the maximum magnitude of the corresponding pixels across the 2 acquired images [8, 17]. After calculating the final images, the two-pool model parameters $F$, $k_f$ and $T_{2,f}$ were estimated from a voxel-by-voxel nonlinear least-squares fit. With the third approach, MT parameters were determined for each phase-cycled acquisition separately before the parameter maps were combined based on a region of interest covering the banding artifacts.
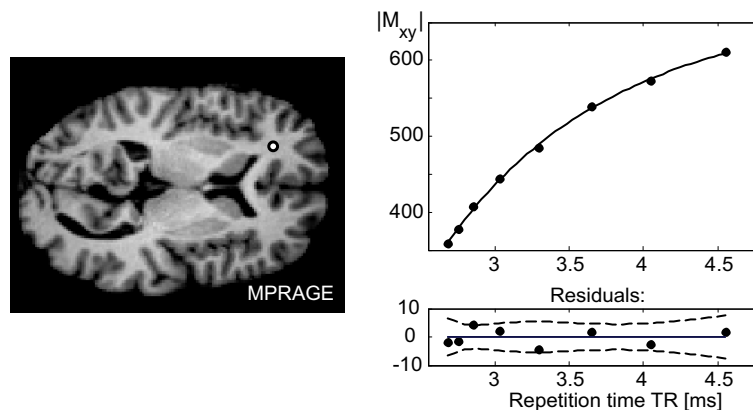


Figure 3.1: Exemplary single voxel fit of the MT-bSSFP equation to 8 bSSFP acquisitions with varying pulse duration and TR for white matter. Resulting two-pool model parameters $F = 15.8 \pm 4.7\,\%$, $k_f = 4.2 \pm 1.8\,\mathrm{s}^{-1}$ ($T_{1,f} = 73\,\mathrm{ms}$, $T_{2,f} = 51\,\mathrm{ms}$).
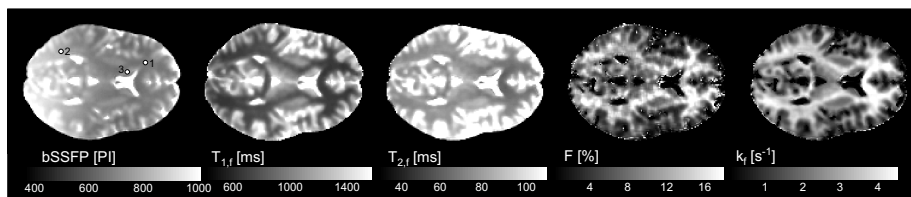
Figure 3.2: Axial sample images: BSSFP image (TR = 4.55 ms) with three evaluated regions of interest; $T_{1,f}$ from DESPOT1; $T_{2,f}$ from DESPOT2; and maps of $F$ and $k_f$ derived from two-pool bSSFP model fitting in a healthy volunteer.
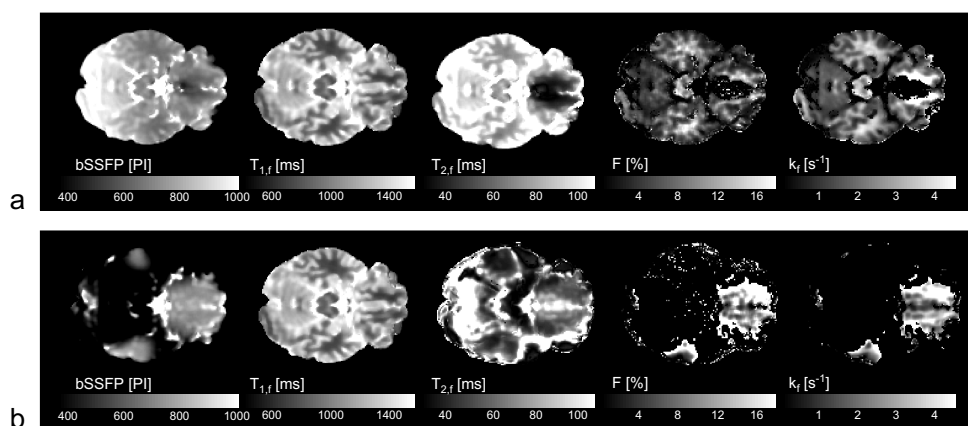


Figure 3.3: Axial sample images showing off-resonance banding artifacts. BSSFP image (TR = 4.55 ms), $T_{1,f}$, $T_{2,f}$, $F$ and $k_f$ for an RF phase increment of (a) $\vartheta$ = 180° and (b) $\vartheta = 0$°.

### 3.1.3   Results

A single voxel fit of the MT-bSSFP equation to the $T_{RF}$-varied bSSFP image acquisition is demonstrated in Fig. 3.1 for brain white matter. Exemplary parameter estimates are $F = 15.8 \pm 4.7\%$, $k_f = 4.2 \pm 1.8\,\mathrm{s}^{-1}$ ($T_{1,f} = 736\,\mathrm{ms}$, $T_{2,f} = 51\,\mathrm{ms}$). In Fig. 3.2, results from qMTI using the two-pool bSSFP model are shown for a normal appearing human brain. Exemplary values for the three displayed regions of interest were: $F_{WM,1} = 16.0 \pm 1.8\%$, $F_{WM,2} = 14.3 \pm 1.5\%$, $F_{GM,3} = 5.8 \pm 0.9$ %, $k_{f,WM,1} = 3.8 \pm 0.2\,\mathrm{s}^{-1}$, $k_{f,WM,2} = 3.7 \pm 0.1\,\mathrm{s}^{-1}$, $k_{f,GM,3} = 1.6 \pm 0.1\,\mathrm{s}^{-1}$ (selected regions of interest, see Fig. 3.2). No problems with banding artifacts arise in the displayed slice.

This is in contrast to slices containing regions near the sinuses (Fig. 3.3). Signal voids in the bSSFP images lead to fitting failures in the $T_{2,f}$, $F$ and $k_f$ maps around the sinuses for an RF phase increment of $\vartheta = 180$°. On the other hand, bSSFP acquisitions with $\vartheta = 0$° feature full signal around the sinuses but banding artifacts in the other regions.

Results using three different combination methods are displayed in Fig. 3.4. Combined bSSFP images, relaxation times, and MT parameters are displayed for sum-of-squares (Fig. 3.4 a) and maximum-intensity (Fig. 3.4 b) methods. Finally,
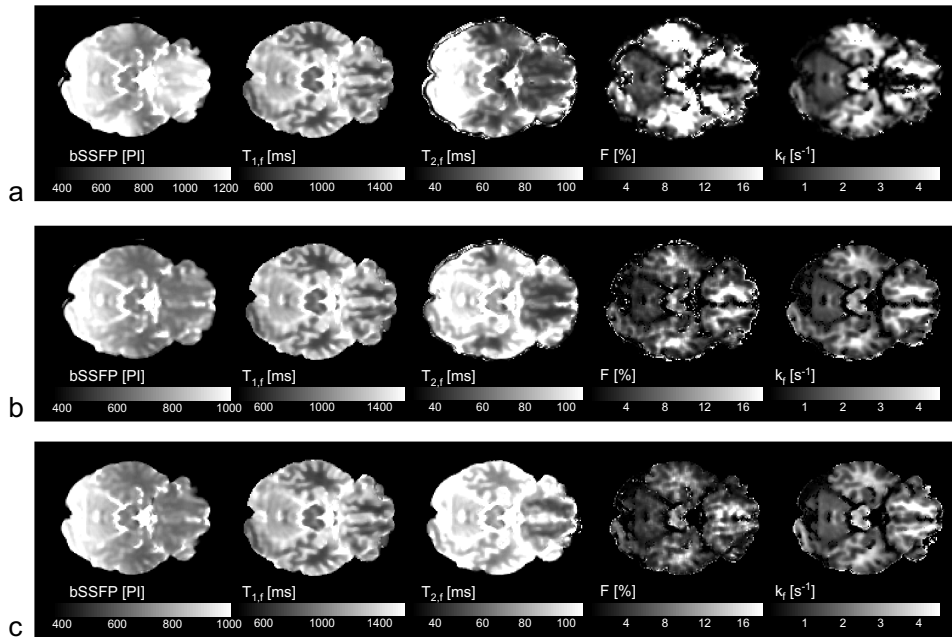
Figure 3.4: BSSFP image (TR = 4.55 ms), $T_{1,f}, T_{2,f}, F$ and $k_f$ maps of a sample slice using (a) sum-of-squares combination, (b) maximum-intensity combination, and (c) combination of separate fitting results.

results from the regional combination after fitting of separate images are shown in Fig. 3.4 c.

### 3.1.4   Discussion

Good correspondence between of the new accelerated qMTI framework with previously published methods [2, 18–24] was observed. It was demonstrated that for human brain, high-resolution 3D maps of the bound proton fraction $F$ and the exchange rate $k_f$ can be derived within less than 10 minutes. This protocol allows a wide application of the technique for various pathologies, such as demyelinating disease, cerebral angiopathy or tumor disorders in a clinical setup.

Furthermore, if needed, critical brain regions with high susceptibility variation may be covered by phase-cycled qMTI using bSSFP. A sum-of-squares combination before two-pool model fitting yielded large deviations in $F$ and $k_f$ and considerable deviations in $T_{2,f}$ from expected values (Fig. 3.4 a). A maximum-intensity combination seems to be more suitable, but $F$ and $k_f$ around the sinuses are notably overestimated (Fig. 3.4 b). The best results were obtained by individually performing the two-pool model fit on each of the phase-cycled data sets. A simple combination of the obtained final parameters yielded reasonable maps of $T_{1,f}$, $T_{2,f}$, $F$ and $k_f$.

In summary, it has been shown that qMTI based on bSSFP is possible with a variation of pulse duration only and a constant flip angle if $T_{2,f}$ is measured additionally. The reduced acquisition time can be used for phase-cycled acquisi-

tions. Most robust results were obtained from a combination of separate fitting results. In order to obtain smoother qMTI maps, however, the use of three or more phase cycles is advisable.

## 3.2   Finite RF Pulse Effects on Quantitative Magnetization Transfer Imaging Using Balanced SSFP

### 3.2.1   Introduction

It has recently been shown that the effect of finite RF pulses can lead to considerable bSSFP signal modulations [25]. As bSSFP-based qMT imaging uses RF pulse modifications, a correction for these effects might be required. In this work, a modification to the two-pool bSSFP equation is analyzed, overcoming the assumption of instantaneous RF pulses in the derivation of quantitative MT parameters. Effects of the correction on the parameter maps are assessed in human brain.
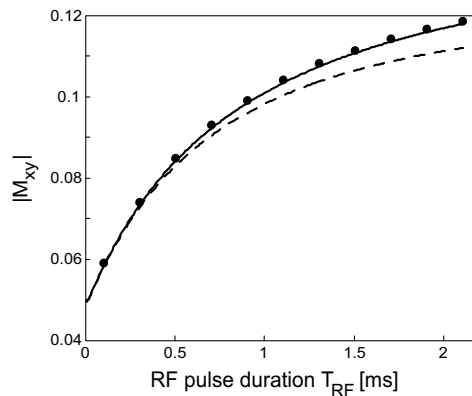


Figure 3.5: Numerical simulation (circles) of a binary spin-bath model and analytical solution without (dashed line) and with (solid line) RF correction for varying RF pulse duration $T_{RF}$ (TR $= 3\,\text{ms} + T_{RF}$, $\alpha = 35°$). Two-pool model parameters for frontal white matter were: $T_{1,f} = T_{1,r} = 733\,\text{ms}, T_{2,f} = 40\,\text{ms}, F = 14.5\,\%, k_f = 4.5\,\text{s}^{-1}, G(0) = 1.4 \cdot 10^{-5}\,\text{s}^{-1}$ [2].

### 3.2.2   Theory

Quantitative MT parameters, such as the bound pool fraction $F$, the forward exchange rate $k_f$ and the transverse relaxation time of the free protons $T_{2,f}$ can be derived from a two-pool bSSFP signal equation by measuring the signal dependence on the RF pulse duration ($T_{RF}$) as well as the flip angle ($\alpha$) dependence [2]. The two-pool bSSFP equation [2] assumes instantaneous RF pulses and therefore underestimates numerical simulations of a binary spin-bath model with increasing $T_{RF}$ (Fig. 3.5, dashed line).

Effects of finite RF pulses are captured by subtracting the part of the effective RF pulse duration, in which no relaxation takes place ($\zeta\,T_{RFE}$), from TR (Fig. 3.6), leading to a reduction in the transverse relaxation rate $R_{2,f}$ according

---

This section has partly been presented as: M. Gloor, K. Scheffler, O. Bieri. Finite RF Pulse Effects on Quantitative Magnetization Transfer Imaging Using Balanced SSFP. Proceedings of the Joint Annual Meeting ISMRM-ESMRMB, Stockholm, 2010.
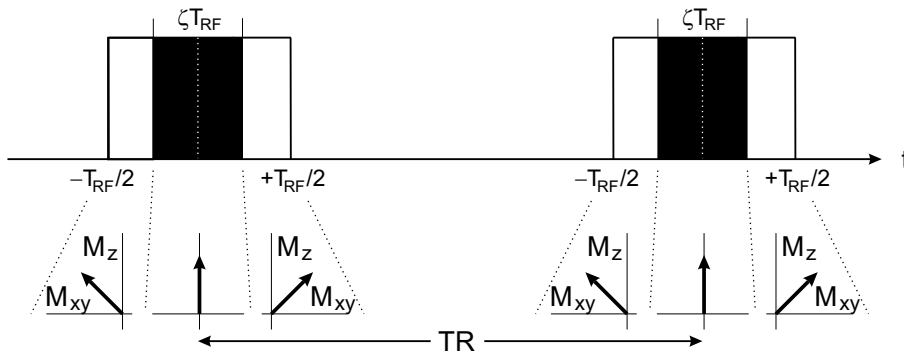
Figure 3.6: RF excitation is split into periods of zenithal and partial transverse alignment of the steady state magnetization. The mean effective fraction of $T_{RF}$, the magnetization appears to spend along the longitudinal direction, is denoted by $\zeta$.

to

$$\tilde{R}_{2,f} := \left(1 - \zeta \frac{T_{RFE}}{TR}\right) R_{2,f}, \text{where}$$
$$T_{RFE} := 1.20 \frac{T_{RF}}{TBW}, \quad \zeta \approx 0.68 - 0.125\left(1 + \frac{T_{RFE}}{TR}\right)\frac{R_{1,f}}{R_{2,f}},$$

$R_{1,f} = 1/T_{1,f}$, and $R_{2,f} = 1/T_{2,f}$ for slice selective pulses [25].

### 3.2.3   Results & Discussion

A comparison of the analytical two-pool bSSFP equation with a numerical simulation of the binary spin-bath model (Fig. 3.5) demonstrates that the finite RF pulse correction very effectively reduces the relative difference from about 5 % to less than 1 % for the longest $T_{RF}$. Figure 3.7 displays a single voxel fit in frontal white matter for a healthy volunteer. Exemplary parameter estimates are $F = 14.9 \pm 5.4\%$, $k_f = 6.8 \pm 4.5\,\text{s}^{-1}$, $T_{2,f} = 44.0 \pm 9.1\,\text{ms}$ without RF pulse correction, and $F = 13.1 \pm 3.8\%$, $k_f = 6.2 \pm 3.3\,\text{s}^{-1}$, $T_{2,f} = 39.0 \pm 6.0\,\text{ms}$ with RF pulse correction. Thus, parameters are reduced by about 10 %, whereas confidence intervals are narrowed by about 30 %, suggesting that the corrected equation describes the data more adequately. Parameter maps of a brain slice and relative differences between corrected and non-corrected results are shown in Fig. 3.8. Region of interest analysis yield similar changes in $F$ (-1.9 % and -1.2 %), $k_f$ (-0.5 s$^{-1}$ and -0.5 s$^{-1}$) and $T_{2,f}$ ($-5.3$ ms and $-5.0$ ms) for frontal white matter and putamen.

### 3.2.4   Conclusion

Especially for high $T_{RF}/TR$, the assumption of instantaneous RF pulses is no longer valid and a correction has to be included in the analysis of bSSFP-based qMT imaging. This finite RF pulse correction improves the fitting quality considerably and reduces the values of $F$, $k_f$ and $T_{2,f}$ by about 10 %.
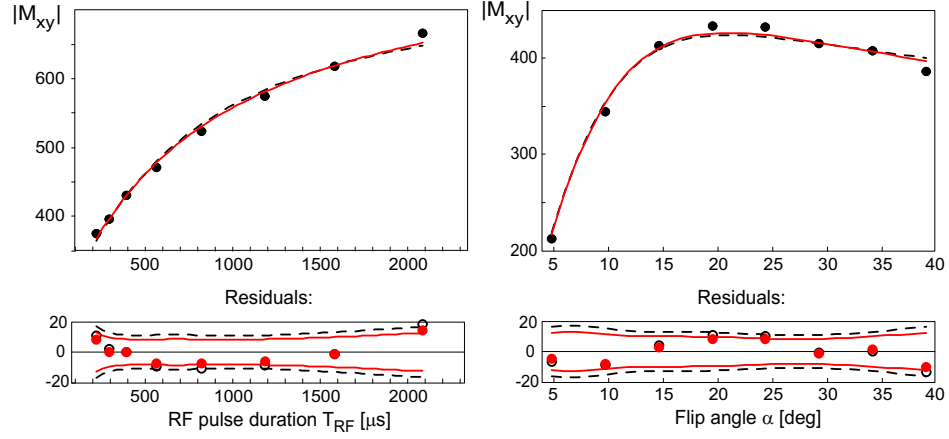
Figure 3.7: Exemplary single voxel fit in frontal white matter using the MT-bSSFP equation without (dashed black lines) and with (solid red lines) RF correction. Additionally, fitting residuals in units of $M_{xy}$ and 95 % confidence interval of the predicted data are shown (black: non-corrected, red: corrected). Correction for finite pulse effects reduces $F$ by 1.8 %, $k_f$ by $0.6\,\mathrm{s}^{-1}$ and $T_{2,f}$ by $5\,\mathrm{ms}$ in this voxel.
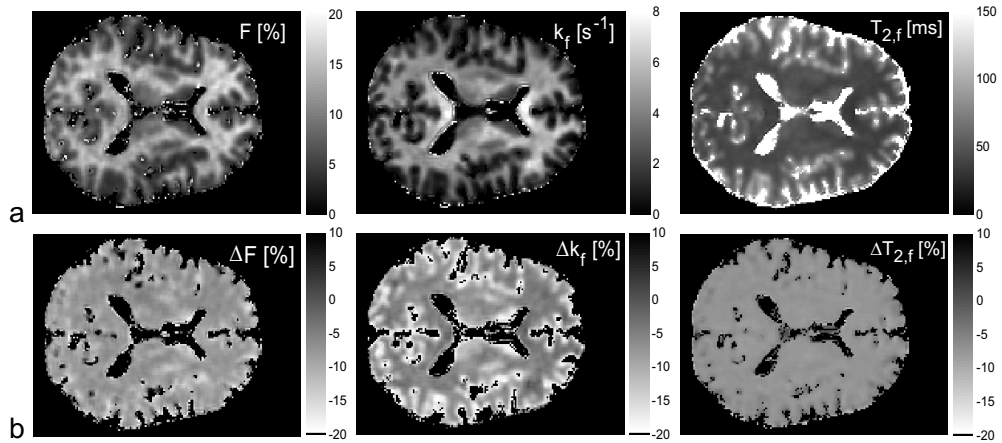


Figure 3.8: (a) Maps of $F$, $k_f$, and $T_{2,f}$ derived from two-pool bSSFP model fitting including a correction for finite RF pulse effects in a healthy volunteer. (b) Relative differences between corrected and non-corrected maps for the three fitting parameters.

# References

[1] O. Bieri and K. Scheffler. On the Origin of Apparent Low Tissue Signals in Balanced SSFP. *Magn Reson Med*, 56(5):1067–74, 2006.

[2] M. Gloor, K. Scheffler, and O. Bieri. Quantitative Magnetization Transfer Imaging Using Balanced SSFP. *Magn Reson Med*, 60(3):691–700, 2008.

[3] H.Y. Carr. Steady-State Free Precession in Nuclear Magnetic Resonance. *Phys. Rev.*, 112(5):1693–1701, 1958.

[4] R Freeman and HDW Hill. Phase and Intensity Anomalies in Fourier Transform NMR. *J Magn Reson*, 4:366–383, 1971.

[5] A Oppelt, R Graumann, H Barfuss, H. Fischer, W Hartl, and W Schajor. FISP: Eine Neue Schnelle Pulssequenz Für Die Kernspintomographie. *Electromedia*, 54:15–18, 1986.

[6] K. Scheffler, O. Heid, and J. Hennig. Magnetization Preparation During the Steady State: Fat-Saturated 3D TrueFISP. *Magn Reson Med*, 45(6):1075–80, 2001.

[7] A Schwenk. NMR Pulse Techniques with High Sensitivity for Slowly Relaxing Systems. *J Magn Reson*, (5):376–389, 1971.

[8] E. M. Haacke, P. A. Wielopolski, J. A. Tkach, and M. T. Modic. Steady-State Free Precession Imaging in the Presence of Motion: Application for Improved Visualization of the Cerebrospinal Fluid. *Radiology*, 175(2):545–52, 1990.

[9] Y. Zur, M. L. Wood, and L. J. Neuringer. Motion-Insensitive, Steady-State Free Precession Imaging. *Magn Reson Med*, 16(3):444–59, 1990.

[10] S. S. Vasanawala, J. M. Pauly, and D. G. Nishimura. Fluctuating Equilibrium MRI. *Magn Reson Med*, 42(5):876–83, 1999.

[11] N. K. Bangerter, B. A. Hargreaves, S. S. Vasanawala, J. M. Pauly, G. E. Gold, and D. G. Nishimura. Analysis of Multiple-Acquisition SSFP. *Magn Reson Med*, 51(5):1038–47, 2004.

[12] T. Cukur, N. K. Bangerter, and D. G. Nishimura. Enhanced Spectral Shaping in Steady-State Free Precession Imaging. *Magn Reson Med*, 58(6):1216–23, 2007.

[13] S. Akoka, F. Franconi, F. Seguin, and A. Le Pape. Radiofrequency Map of an NMR Coil by Imaging. *Magn Reson Imaging*, 11(3):437–41, 1993.

[14] S. C. Deoni, T. M. Peters, and B. K. Rutt. High-Resolution T1 and T2 Mapping of the Brain in a Clinically Acceptable Time with DESPOT1 and DESPOT2. *Magn Reson Med*, 53(1):237–41, 2005.

[15] S. M. Smith, M. Jenkinson, M. W. Woolrich, C. F. Beckmann, T. E. Behrens, H. Johansen-Berg, P. R. Bannister, M. De Luca, I. Drobnjak, D. E. Flitney, R. K. Niazy, J. Saunders, J. Vickers, Y. Zhang, N. De Stefano, J. M. Brady, and P. M. Matthews. Advances in Functional and Structural MR Image Analysis and Implementation as FSL. *Neuroimage*, 23 Suppl 1:S208–19, 2004.

[16] R. W. Cox. AFNI: Software for Analysis and Visualization of Functional Magnetic Resonance Neuroimages. *Comput Biomed Res*, 29(3):162–73, 1996.

[17] J. W. Casselman, R. Kuhweide, M. Deimling, W. Ampe, I. Dehaene, and L. Meeus. Constructive Interference in Steady State-3DFT MR Imaging of the Inner Ear and Cerebellopontine Angle. *AJNR Am J Neuroradiol*, 14(1): 47–57, 1993.

[18] R. M. Henkelman, X. Huang, Q. S. Xiang, G. J. Stanisz, S. D. Swanson, and M. J. Bronskill. Quantitative Interpretation of Magnetization Transfer. *Magn Reson Med*, 29(6):759–66, 1993.

[19] C. Morrison and R. M. Henkelman. A Model for Magnetization Transfer in Tissues. *Magn Reson Med*, 33(4):475–82, 1995.

[20] G. B. Pike. Pulsed Magnetization Transfer Contrast in Gradient Echo Imaging: A Two-Pool Analytic Description of Signal Response. *Magn Reson Med*, 36(1):95–103, 1996.

[21] S. J. Graham and R. M. Henkelman. Understanding Pulsed Magnetization Transfer. *J Magn Reson Imaging*, 7(5):903–12, 1997.

[22] J. G. Sled and G. B. Pike. Quantitative Imaging of Magnetization Transfer Exchange and Relaxation Properties in Vivo Using MRI. *Magn Reson Med*, 46(5):923–31, 2001.

[23] A. Ramani, C. Dalton, D. H. Miller, P. S. Tofts, and G. J. Barker. Precise Estimate of Fundamental in-Vivo MT Parameters in Human Brain in Clinically Feasible Times. *Magn Reson Imaging*, 20(10):721–31, 2002.

[24] M. Cercignani, M. R. Symms, K. Schmierer, P. A. Boulby, D. J. Tozer, M. Ron, P. S. Tofts, and G. J. Barker. Three-Dimensional Quantitative Magnetisation Transfer Imaging of the Human Brain. *Neuroimage*, 27(2): 436–41, 2005.

[25] O. Bieri and K. Scheffler. SSFP Signal with Finite RF Pulses. *Magn Reson Med*, 62(5):1232–41, 2009.

# Chapter 4

# Nonbalanced SSFP-Based Quantitative Magnetization Transfer Imaging

## 4.1 Introduction

Magnetization transfer (MT) was introduced by Wolff and Balaban about two decades ago [1] and has been widely used to improve the suppression of background signals from tissues in MR angiography [2]. Further potential applications include characterization of brain tissue degenerations such as multiple sclerosis plaques, ischemic lesions and edema [3, 4], and also offer new insights in tissue structures of the musculoskeletal system like cartilage repair tissue [5]. Often, pathologies reduce the so-called magnetization transfer ratio (MTR) that correlates with a decreased fraction of bound protons. However, the description of complex systems (such as tissues) by one single parameter seems to be an oversimplification and potentially useful diagnostic information may be missed [6]. As a result, several methods have been developed for extracting intrinsic MT model parameters [6–11], commonly referred to as quantitative MT imaging (qMTI). Based on a binary spin-bath model, qMTI yields the fraction ($F$) of restricted pool protons, the magnetization exchange rate ($k_f$) and the pool relaxation properties ($T_1$, $T_2$). Most of these methods use spin-echo or radio-frequency (RF) spoiled gradient-echo sequences combined with MT preparation pulses that differ in power and off-resonance frequency [6, 8].

Recently, a new and fast approach for qMTI was introduced [12] based on balanced steady-state free precession (bSSFP; also known as TrueFISP, FIESTA and balanced FFE). Balanced SSFP is well applicable to targets with low susceptibility variation such as the human brain, but in targets with high susceptibility variation such as cartilage and muscle, off-resonance effects cause signal loss. As a result, an adaptation of the previously proposed qMTI concept from bSSFP to nonbalanced SSFP is anticipated to characterize such targets. It has already been shown that MT effects correlate very well among all different SSFP protocols in terms of MTR [13]. Similar to bSSFP, on-resonant excitation in nonbalanced SSFP not only generates the steady-state, but also acts MT sensitizing, especially for short repetition times (TR) and large flip angles. Therefore, the well-known steady-state equations are expected to considerably overestimate the signal in tissues, where exchange between free and restricted pool protons takes place.

In this work, the recently proposed concept for qMTI using bSSFP [12] is adapted to SSFP-FID (also known as FISP, FFE, GRASS, FAST). First, to incorporate MT effects, an extended SSFP-FID signal equation based on a binary spin-bath model is derived. Since relaxation and exchange can be considered as separate and independent processes within TR, partial integration of the coupled Bloch equations is used to derive a new steady-state eigenvector equation for SSFP-FID that can be solved analytically. Numerical simulations are performed to confirm the derived two-pool SSFP-FID signal equation and thereby justify the conceptual separation of relaxation and exchange processes. In the second part, the extended SSFP-FID equation is used to derive qMTI parameters from an ex vivo muscle sample, in vivo human femoral muscle and in vivo human patellar cartilage. The derived parameters from SSFP-FID will be compared to those derived using bSSFP or to literature values. Finally, specific signal properties of SSFP-FID and bSSFP such as sensitivity to motion are discussed and compared.

## 4.2   Theory

### 4.2.1   Single-Pool SSFP-FID Signal Equation

Assuming quasi-instantaneous RF excitation pulses, an expression for the steady-state magnetization can be derived from the Bloch equations using partial integration. Directly after the RF pulse and in steady state, the (complex) transverse magnetization $M_{xy} = M_x + iM_y$ is given by

$$M_{xy}^+ = M_0 \sin \alpha \; \frac{(1 - E_1)(1 - E_2 e^{i\varphi})}{C \cos \varphi + D}, \tag{4.1}$$

where

$$C = E_2(E_1 - 1)(1 + \cos \alpha), \; D = 1 - E_1 \cos \alpha - (E_1 - \cos \alpha)E_2^2, \tag{4.2}$$

$E_{1,2} = \exp(-\mathrm{TR}/T_{1,2})$, $\alpha$ denotes the flip angle, $\varphi$ the dephasing angle in the $xy$-plane and $M_0$ the equilibrium magnetization [14]. For nonbalanced SSFP, a dephasing of $\varphi = [-\pi \ldots \pi]$ per voxel is induced from unbalanced gradient moments. Therefore, the steady-state signal of SSFP-FID is found by averaging the steady-state transverse magnetization within one voxel corresponding to an integration of Eq. (4.1) over all possible dephasing angles [14]:

$$
\begin{aligned}
\langle M_{xy}^+ \rangle &= M_0 \sin \alpha \frac{1 - E_1}{2\pi} \int_{-\pi}^{\pi} \frac{1 - E_2 \cos \varphi}{C \cos \varphi + D} d\varphi \\
&= M_0 \sin \alpha \; \frac{1 - E_1}{C} \left( \frac{C + D E_2}{\sqrt{D^2 - C^2}} - E_2 \right). \tag{4.3}
\end{aligned}
$$

From Eq. (4.3), only a slight dependence of the steady-state amplitude on TR is expected due to the weak $T_1$-weighting of this sequence [13]. This can be confirmed in aqueous probes, however, under certain circumstances tissues show considerable signal deviation from Eq. (4.3) that can be attributed to MT [15]. In the following, an SSFP-FID signal equation is derived based on a binary spin-bath model to allow for quantification of MT effects [6, 16].

### 4.2.2   Two-Pool SSFP-FID MT Model

The simplest model for MT signal analysis consists of a liquid pool of free protons (subscript $f$) and a semisolid pool of protons that are restricted in motion (subscript $r$). The formal description of this binary spin-bath model results in a set of coupled differential equations, as shown in detail elsewhere [6, 16]. Pulsed off-resonance irradiation with frequency offset $\varphi$ affects the longitudinal magnetization of the restricted pool protons, given by a time-dependent mean saturation rate [17]

$$\langle W(\Delta) \rangle = \frac{\pi}{T_{RF}} \int_0^{T_{RF}} \omega_1^2(t) dt \, G(\Delta). \tag{4.4}$$

Here, $G(\Delta)$ is the absorption line shape, and $\langle W(\Delta) \rangle$ depends on the power $(\omega_1^2)$ and duration $(T_{RF})$ of the RF pulse.

On-resonance RF pulses are used for imaging with SSFP, i.e. $\Delta \to 0$ [15], and therefore the system of differential equations [6] reduces to:

$$\frac{dM_{x,f}}{dt} = -R_{2,f}M_{x,f} + \gamma \langle \mathbf{G}(t) | \mathbf{r} \rangle M_{y,f}, \tag{4.5a}$$

$$\frac{dM_{y,f}}{dt} = -R_{2,f}M_{y,f} + \omega_1(t)M_{z,f} - \gamma \langle \mathbf{G}(t) | \mathbf{r} \rangle M_{x,f}, \tag{4.5b}$$

$$\frac{dM_{z,f}}{dt} = R_{1,f}(M_{0,f} - M_{z,f}) - k_f M_{z,f} + k_r M_{z,r} - \omega_1(t)M_{y,f}, \tag{4.5c}$$

$$\frac{dM_{z,r}}{dt} = R_{1,r}(M_{0,r} - M_{z,r}) + k_f M_{z,f} - k_r M_{z,r} - W(\Delta \to 0, t)M_{z,r}, \tag{4.5d}$$

where the subscripts $x$, $y$, $z$ denote the various spatial components of the magnetization vector $\mathbf{M}$. The dephasing from unbalanced gradient moments $(\gamma \int G(t)dt)$ corresponds to a precession around the $z$-axis, whereas $R_{1,f}$ $(R_{1,r})$ and $R_{2,f}$ $(R_{2,r})$ refer to the longitudinal and transverse relaxation rates of the free (restricted) pools $(R_{1,2} = 1/T_{1,2})$, respectively. $M_{0,f}$ $(M_{0,r})$ denotes the equilibrium magnetization of the free (restricted) pool and magnetization exchange is described by the pseudo-first order rate constants $k_f = RM_{0,r}$ and $k_r = RM_{0,f}$, where $R$ is the fundamental rate constant between the two pools. The fractional size of the restricted pool is $F := M_{0,r}/M_{0,f}$ and by definition $k_r := k_f/F$.

### 4.2.3 Two-Pool SSFP-FID Signal Equation

In principle, equations (4.5a)-(4.5d) offer an accurate description of MT-SSFP experiments. Nevertheless, it is computationally infeasible to use these ordinary differential equations to estimate the parameters of the two-pool model. For fast estimation of MT model parameters, a simple solution to Eqs. (4.5a)-(4.5d) is desirable. Assuming that exchange processes decouple from relaxation within the short TR used with SSFP [12], an analytical expression for the two-pool SSFP-FID model is derived based on the partially integrated Bloch equations, as introduced by Carr in 1958 and Ernst and Anderson in 1966 [18, 19]. In the following, the system of differential equations (Eqs. (4.5a)-(4.5d)) with magnetization $\mathbf{M} = (M_{x,f} \ M_{y,f} \ M_{z,f} \ M_{z,r})$ is split into four separate processes:

Exchange and relaxation parts yield a solution of form $\mathbf{M}(t) = \mathbf{A}(t) \cdot \mathbf{M}(0)$ and $\mathbf{M}(t) = \mathbf{E}(t) \cdot \mathbf{M}(0)$ with matrices

$$\mathbf{A}(t) = \frac{1}{F+1} \begin{pmatrix} F+1 & 0 & 0 & 0 \\ 0 & F+1 & 0 & 0 \\ 0 & 0 & 1+Fe^{-(F+1)k_r t} & 1-e^{-(F+1)k_r t} \\ 0 & 0 & F-Fe^{-(F+1)k_r t} & F+e^{-(F+1)k_r t} \end{pmatrix} \text{ and}$$

$$\mathbf{E}(t) = \begin{pmatrix} E_{2,f} & 0 & 0 & 0 \\ 0 & E_{2,f} & 0 & 0 \\ 0 & 0 & E_{1,f} & 0 \\ 0 & 0 & 0 & E_{1,r} \end{pmatrix}, \tag{4.6}$$

where $E_{2,f} = \exp(-R_{2,f}t)$, $E_{1,f} = \exp(-R_{1,f}t)$.

Excitation is captured in a matrix $\mathbf{R_x}$ that contains a rotation about the $x$-axis for the free pool and a saturation term for the restricted pool, whereas precession due to the gradient field is described by $\mathbf{R_z}$ that effects a rotation about the $z$-axis according to

$$
\mathbf{R}_x(\alpha, t) = \begin{pmatrix} 1 & 0 & 0 & 0 \\ 0 & \cos\alpha & \sin\alpha & 0 \\ 0 & -\sin\alpha & \cos\alpha & 0 \\ 0 & 0 & 0 & e^{-\langle W(\Delta \to 0)\rangle t} \end{pmatrix} \text{ and }
$$

$$
\mathbf{R}_z(\varphi) = \begin{pmatrix} \cos\varphi & \sin\varphi & 0 & 0 \\ -\sin\varphi & \cos\varphi & 0 & 0 \\ 0 & 0 & 1 & 0 \\ 0 & 0 & 0 & 1 \end{pmatrix}. \tag{4.7}
$$

This allows for the formulation of an eigenvalue equation for the steady-state magnetization directly after an RF pulse following standard methods [20]. Except for the additional $x$-component, derivation is analogous to the case of balanced SSFP [12], yielding

$$
\mathbf{M}^+(\infty) = \mathbf{R}_x(\mathbf{I} - \mathbf{R}_z^{-1}\mathbf{AER}_x)^{-1}\mathbf{AM}_0 \text{ and }
$$

$$
\mathbf{M}_0 = \begin{pmatrix} 0 \\ 0 \\ M_{0,f}(1 - E_{1,f}) \\ M_{0,r}(1 - E_{1,r}) \end{pmatrix}, \tag{4.8}
$$

with solution

$$
M_{xy}^+ = M_{0,f} \sin\alpha \; \frac{H\left(1 - E_2 e^{i\varphi}\right)}{C\cos\varphi + D}, \tag{4.9}
$$

in case relaxation takes place before exchange. Equation (4.9) is the solution to the phase dependent Bloch equations including MT and corresponds to Eq. (4.1). Averaging of the transverse magnetization within one voxel finally leads to the two-pool SSFP-FID equation

$$
\langle M_{xy}^+\rangle = M_{0,f} \sin\alpha \; \frac{H}{C} \left(\frac{C + DE_2}{\sqrt{D^2 - C^2}} - E_2\right), \tag{4.10}
$$

where

$$
\begin{aligned}
A &= 1 + F - f_w E_{1,r}(F + f_k), \\
B &= 1 + f_k(F - f_w E_{1,r}(F + 1)), \\
C &= E_2(BE_{1,f} - A)(1 + \cos\alpha), \\
D &= A - BE_{1,f}\cos\alpha - (BE_{1,f} - A\cos\alpha)E_2^2, \\
H &= M_{0,f}B(1 - E_{1,f}) + M_{0,r}(1 - E_{1,r})(1 - f_k), \\
f_k &= \exp[-(k_f + k_r)\mathrm{TR}], \\
f_w &= \exp\left[-\langle W(\Delta \to 0)\rangle\, \mathrm{T_{RF}}\right], \\
M_{0,f} &= 1, \\
E_{2,f} &= \exp(-R_{2,f}\mathrm{TR}), \\
E_{1,f} &= \exp(-R_{1,f}\mathrm{TR}), \\
E_{1,r} &= \exp(-R_{1,r}\mathrm{TR}).
\end{aligned}
\tag{4.11}
$$

Equation (4.10) is of the same form as the common single-pool SSFP-FID steady-state equation (Eq. (4.3)) but includes some additional terms related to the MT parameters $F$, $k_f$ and the mean saturation rate $\langle W \rangle$. These additional terms vanish in the limit of $\langle W \rangle$, $F$, $k_f$, $k_r$, $E_{1,r} \to 0$, and Eq. (4.10) then converges to Eq. (4.3). A similar expression can be derived for relaxation taking place after exchange (not shown). Since both solutions are almost identical (deviations are typically less than 1 %), only the former solution (relaxation before exchange) is considered.

## 4.3   Methods

Experiments and calibrations were performed on a Siemens 1.5 T Avanto system (Siemens Healthcare, Erlangen, Germany) and all numerical simulations, data analysis and visualization were done in Matlab 2007b (The MathWorks, Inc., Natick, MA). For verification of Eq. (4.10) and to justify the separation of relaxation and exchange processes (see Eq. (4.6)), numerical simulations of the full set of non-simplified ordinary differential equations (ODE) (see Eqs. (4.5a)-(4.5d)) were performed using a standard solver for non-stiff ODEs. Simulations and data analysis followed those presented by Gloor et al. [12], except for the properties of the line shape, which was allowed to be tissue-dependent: The singularity of the Super-Lorentzian lineshape at $\Delta \to 0$ was handled by extrapolation from 1 kHz. This reference point corresponds to the approximate mean bandwidth of the RF pulses used. Extrapolation to the asymptotic limit yields $G(0) = 1.0 \cdot 10^{-5}\,\mathrm{s^{-1}}$ (for $T_{2,r} = 6.6\,\mathrm{s}$, [6]) for uncooked beef and $G(0) = 1.2 \cdot 10^{-5}\,\mathrm{s^{-1}}$ (for $T_{2,r} = 8.5\,\mathrm{s}$, [21]) for skeletal muscle or cartilage (Fig. 4.1). The exchange rate and $T_2$ are only marginally affected (about 6 % and 1.5 % variation, respectively) by a change in $G(0)$ by 17 % (from 1.2 to 1.0 or 1.4 $\cdot 10^{-5}\,\mathrm{s^{-1}}$), whereas $F$ varies substantially (about 20 %).
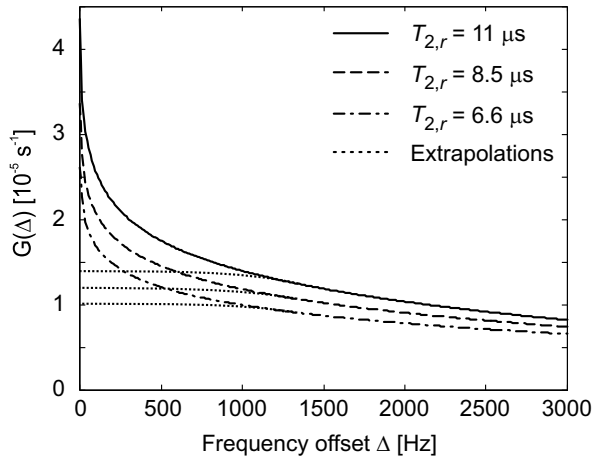
Figure 4.1: Frequency dependence of the Super-Lorentzian absorption line shape $G(\Delta)$ for brain tissue ($T_{2,f} \approx 11$ ms [21]), skeletal muscle or cartilage ($T_{2,f} \approx 8.5$ ms [21]), and uncooked beef ($T_{2,f} \approx 6.6$ ms [6]). Super-Lorentzian line shapes have been found to be appropriate for description of tissues. Extrapolation of the curves to the asymptotic limit of $\Delta \to 0$ yields $G(0) \approx 1.4 \cdot 10^{-5}$ s$^{-1}$, $G(0) \approx 1.2 \cdot 10^{-5}$ s$^{-1}$ and $G(0) \approx 1.0 \cdot 10^{-5}$ s$^{-1}$ for the different tissues.

### 4.3.1  Ex Vivo Experiments

As a proof of principle and to avoid any ambiguity in the results that might arise from the motion sensitivity of SSFP-FID, first, an ex vivo sample (muscle-rich uncooked beef immersed in water) is used for comparison with bSSFP-qMTI [12]. Acquisitions were performed in 3D based on a $192 \times 192 \times 20$ matrix yielding 1.3 mm isotropic resolution. MT-weighting of SSFP-FID can be modified by variation of the flip angle ($\alpha$) or variation of the RF pulse duration ($T_{RF}$) and repetition time (TR) in Eq. (4.10) (Fig. 4.2). In summary, the protocol used for quantitative MT parameter estimation consisted of:

1. Two spoiled gradient echo (SPGR) sequences (TR/TE = 9.8 ms/4.3 ms, bandwidth = 140 Hz/Pixel) with flip angles $\alpha_1 = 3°$ and $\alpha_2 = 17°$ for calculation of a $T_{1,f}$ map according to the DESPOT1 method [22, 23].

2. Eight SSFP-FID sequences with $\alpha = 35°$ (bandwidth = 790 Hz/Pixel) and varying RF pulse durations (TR$_1$/T$_{RF,1}$ = 2.62 ms/0.23 ms, TR$_2$/T$_{RF,2}$ = 2.64 ms/0.3 ms, TR$_3$/T$_{RF,3}$ = 3.73 ms/0.4 ms, TR$_4$/T$_{RF,4}$ = 2.85 ms/ 0.58 ms, TR$_5$/T$_{RF,5}$ = 3.11 ms/0.84 ms, TR$_6$/T$_{RF,6}$ = 3.47 ms/1.2 ms, TR$_7$/ T$_{RF,7}$ = 4.87 ms/1.6 ms, TR$_8$/T$_{RF,8}$ = 4.37 ms/2.1 ms).

3. Eight SSFP-FID sequences with TR/T$_{RF}$ = 2.64 ms/0.3 ms (bandwidth = 790 Hz/Pixel) and varying flip angles ($\alpha_1 = 5°$, $\alpha_2 = 10°$, $\alpha_3 = 15°$, $\alpha_4 = 20°$, $\alpha_5 = 25°$, $\alpha_6 = 30°$, $\alpha_7 = 35°$, $\alpha_8 = 40°$).

4. A multislice (16 slices, 5 mm slice thickness) $B_1$ field map sequence ($64 \times 64$ matrix, 4 mm in plane resolution) using stimulated echoes in a multipulse
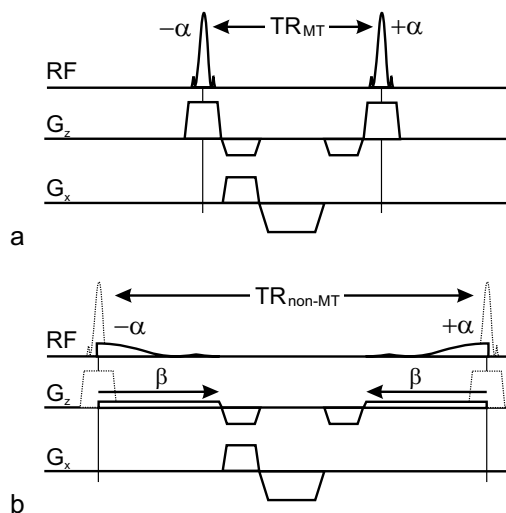
Figure 4.2: SSFP-FID sequence scheme implemented for modulation of MT effects from RF pulse variation. (a) Short RF pulse durations and minimal repetition times $TR_{MT}$ strongly attenuate the steady-state signal from MT. (b) Minimal MT effects (and thus maximum signal) can be achieved from a considerable increase in the RF pulse duration (factor $\beta$ leading to an increased repetition time $TR_{non-MT}$), yielding low saturation of the restricted pool protons.

sequence ($\alpha-\alpha-\alpha$ analogous to the $\alpha-2\alpha-\alpha$ scheme [24] for the assessment of flip angle deviations.

Overall qMTI data acquisition was completed within 5 minutes using a 12 channel head coil, parallel imaging and partial Fourier.

### 4.3.2 In Vivo Experiments

For in vivo muscle and cartilage imaging, a $192 \times 192 \times 16$ matrix was used, yielding 1 mm in plane resolution and a slice thickness of 3 mm and 1.25 mm for muscle and cartilage, respectively. The protocol used for quantitative MT parameter estimation consisted of:

1. Two spoiled gradient echo (SPGR) sequences (TR/TE $= 10$ ms/4.9 ms, bandwidth $= 140$ Hz/Pixel) with flip angles $\alpha_1 = 3.2°$ and $\alpha_2 = 18.3°$ for calculation of a $T_{1,f}$ map according to the DESPOT1 method [22, 23]

2. Ten SSFP-FID sequences with $\alpha = 35°$ (bandwidth $= 790$ Hz/Pixel) and varying RF pulse durations ($TR_1/T_{RF,1} = 3.04$ ms/0.23 ms, $TR_2/T_{RF,2} = 3.11$ ms/0.3 ms, $TR_3/T_{RF,3} = 3.21$ ms/0.4 ms, $TR_4/T_{RF,4} = 3.31$ ms/0.5 ms, $TR_5/T_{RF,5} = 3.46$ ms/0.65 ms, $TR_6/T_{RF,6} = 3.66$ ms/0.85 ms, $TR_7/T_{RF,7} = 3.91$ ms/1.1 ms, $TR_8/T_{RF,8} = 4.21$ ms/1.4 ms, $TR_9/T_{RF,9} = 4.61$ ms/1.8 ms, $TR_{10}/T_{RF,10} = 5.01$ ms/2.2 ms).

3. Ten SSFP-FID sequences with TR/$T_{RF} = 2.99$ ms/0.27 ms (bandwidth $=$

790 Hz/Pixel) and varying flip angles ($\alpha_1 = 4°$, $\alpha_2 = 8°$, $\alpha_3 = 12°$, $\alpha_4 = 16°$, $\alpha_5 = 20°$, $\alpha_6 = 24°$, $\alpha_7 = 28°$, $\alpha_8 = 32°$, $\alpha_9 = 36°$, $\alpha_{10} = 40°$).

4. A multislice (16 slices, 5 mm slice thickness) $B_1$ field map sequence ($64 \times 64$ matrix, 4 mm in plane resolution) using stimulated echoes in a multipulse sequence ($\alpha-\alpha-\alpha$ analogous to the $\alpha-2\alpha-\alpha$ scheme [24] for the assessment of flip angle deviations.

Six outer averages were taken to reduce possible SSFP-FID motion sensitivity. Nevertheless, overall qMTI data acquisition was completed within 15 minutes (including DESPOT1: 1:01 min; SSFP-FID (varying $\alpha$): 5:24 min; SSFP-FID (varying $T_{RF}$): 6:36 min; $B_1$ map: 1:42 min) using an 8 channel knee coil, parallel imaging and partial Fourier. Measurements on healthy volunteers were approved by the local ethics committee.

## 4.4 Results

### 4.4.1 Validation

Figure 4.3 compares the derived two-pool SSFP-FID steady-state equation (Eq. (4.10)) with numerical simulations of the system of ODEs (Eqs. (4.5a)-(4.5d)) for muscle using parameters from Stanisz et al. [21]. Within the range of experimentally applied flip angles (see "Methods" section), the analytical solution slightly underestimates simulated values by less than 1 % (Fig. 4.3 a). The two-pool SSFP-FID signal as a function of $T_{RF}$ (and TR) is displayed in Fig. 4.3 c. Here, simulated RF pulse durations covered a range of $0.23 < T_{RF} < 2.1$ ms at a fixed time-bandwidth product of 2.7, corresponding to a TR variation between 2.62 ms and 4.49 ms. Similar to Fig. 4.3 a, Eq. (4.10) slightly underestimates values from full ODE simulations and the discrepancy increases with increasing RF pulse durations. At $T_{RF} = 2.1$ ms the simulated value exceeds the one deduced from the signal equation by 4 %. In summary, good correspondence between the analytical description of the two-pool SSFP-FID model (Eqs. (4.10)-(4.11)) and the numerical simulations based on the full, i. e. non-simplified, ODEs (Eqs. (4.5a)-(4.5d)) was found.

### 4.4.2 Quantitative Magnetization Transfer Imaging (qMTI)

From unbalanced gradient moments, SSFP-FID acquisitions are prone to flow and motion artifacts. Six repetitions of ex vivo and in vivo qMTI curves were taken and averaged in order to increase signal stability (Fig. 4.4 a, b). Stability was analyzed by calculating the relative mean standard deviations across the repetitions for each set of parameters. Standard deviations of 1 % for the ex vivo muscle increased to 2 % for the in vivo muscle with a less smooth overall appearance of the sampled data. A similar analysis was performed for cartilage, resulting in a mean standard deviation of 3 %.

Non-linear least-squares fitting of Eqs. (4.10)-(4.11) to ex vivo muscle data (Fig. 4.4 c) is exemplarily depicted for a single voxel as a function of the RF
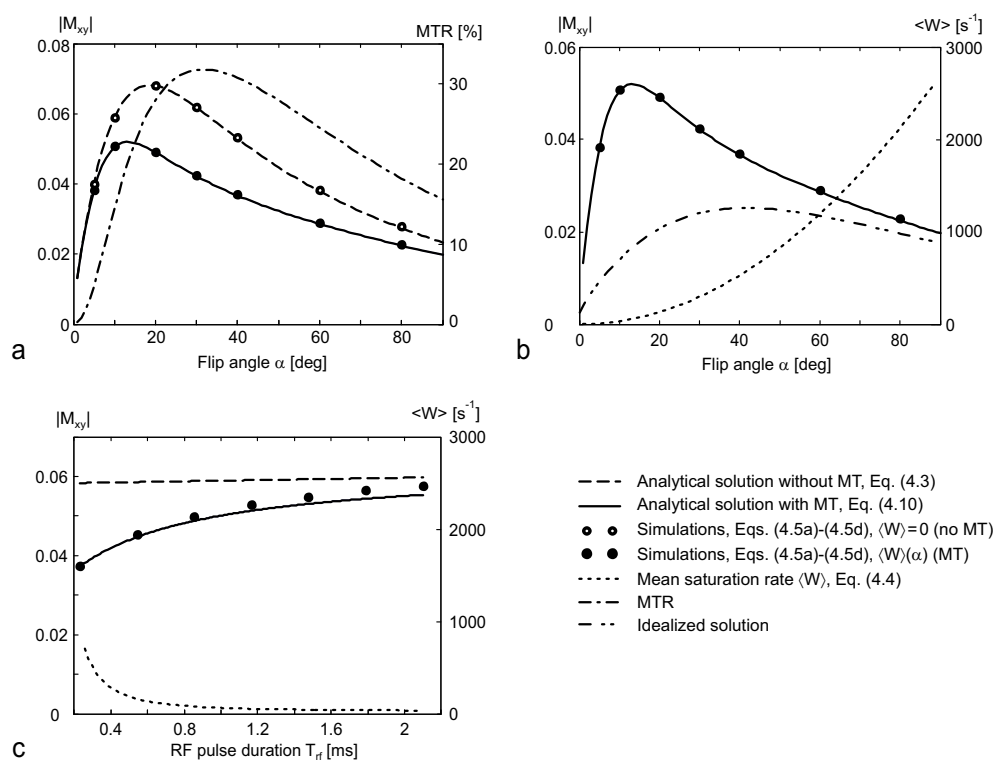
Figure 4.3: Numerical simulation of the two-pool model ODEs (see Eqs. (4.5a)-(4.5d)) for SSFP-FID and corresponding analytical solution (see Eqs. (4.10)-(4.11)) for skeletal muscle (parameter values were taken from literature [21]: $T_{1,f} = 1008\,\text{ms}$, $T_{2,f} = 44\,\text{ms}$, $F = 7.4\,\%$, $k_f = 4.88\,\text{s}^{-1}$, $R_{1,r} = 1\,\text{s}^{-1}$, $T_{2,r} = 8.7\,\mu\text{s}$). (a) Transverse magnetization $|M_{xy}|$ with and without MT ($\langle W \rangle = 0$) and corresponding MTR as a function of the flip angle ($\alpha$). Excellent correspondence between numerical simulations and the prediction according to the analytical solution of the two-pool SSFP-FID model is found. (b) Variation of $\alpha$ (TR = 2.64 ms, $T_{RF} = 300\,\mu\text{s}$): The two-pool SSFP-FID signal equation converges to the idealized case (i. e. fully saturated restricted pool as in [12]) roughly at $\alpha > 80°$, thereby indicating full saturation of restricted pool protons. (c) Variation of $T_{RF}$ ($\alpha = 35°$): Simulation and solution match for low $T_{RF}$ but deviate with increasing RF pulse durations.
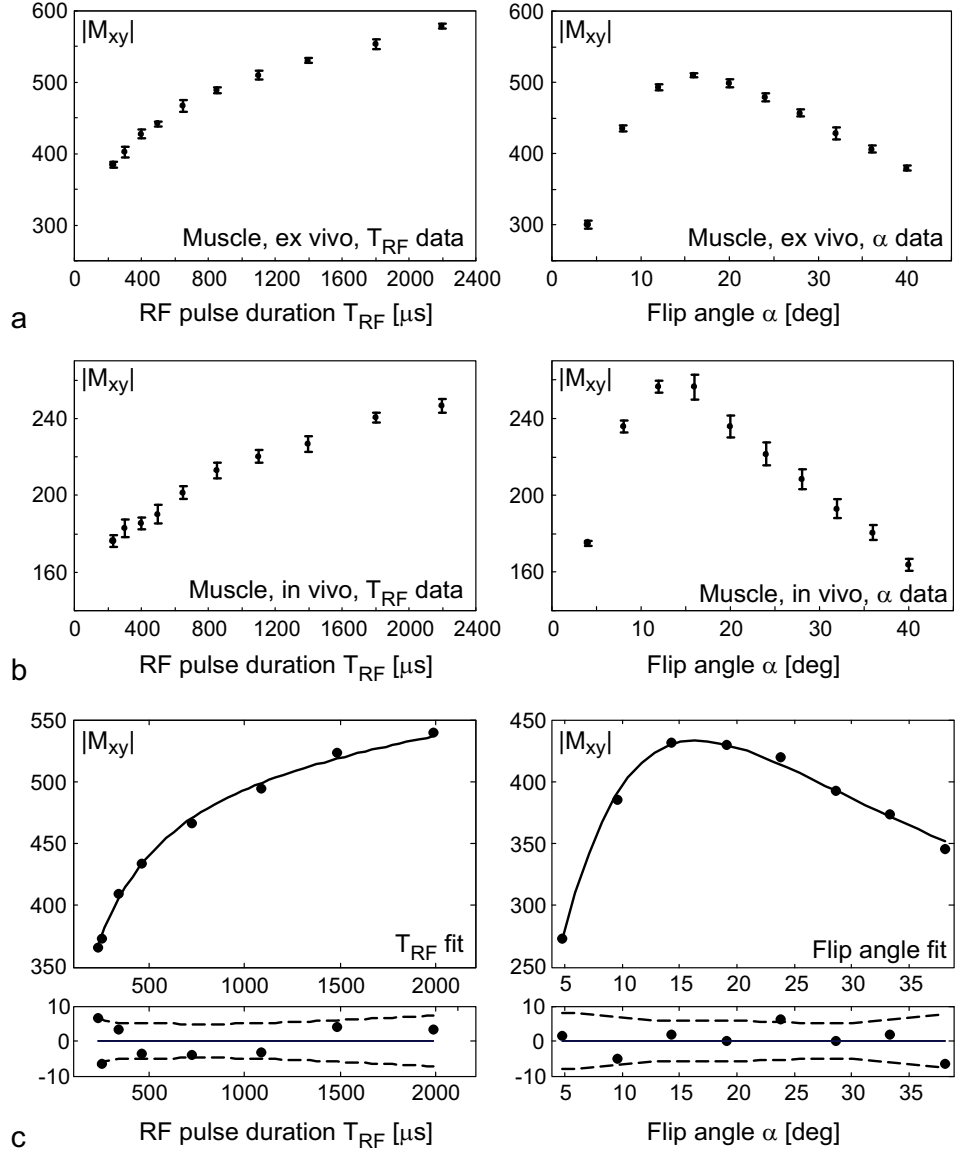
Figure 4.4: Mean SSFP-FID signal and standard deviations averaged over six measurements as a function of the RF pulse duration $T_{RF}$ and flip angle $\alpha$ for selected ROIs in (a) ex vivo muscle and (b) in vivo human femoral muscle. (c) Example of a two-pool SSFP-FID model analysis of a single voxel $(1.3 \times 1.3 \times 1.3\,\mathrm{mm}^3)$ for an ex vivo muscle sample. Nonlinear least squares fitting of Eqs. (4.10)-(4.11) yields the spin-bath model parameters $F = 10.1 \pm 1.9\,\%$, $k_f = 5.8 \pm 2.8\mathrm{s}^{-1}$ and $T_{2,f} = 50.5 \pm 3.5\,\mathrm{ms}$. Residuals of the fit are shown for $95\,\%$ confidence level and in units of $M_{xy}$.

pulse duration and flip angle. Global fits (i.e. both flip angle and $T_{RF}$ varied data sets share the same MT model parameters) yield parameter estimates for the fractional pool size $F$, the exchange rate $k_f$ and the relaxation time of the free pool $T_{2,f}$. Tables 4.1 and 4.2 summarize the results from qMTI using the two-pool SSFP-FID model in an ex vivo muscle sample and compares them to literature results. All quantitative parameters correspond well to the ones derived based on the two-pool bSSFP model [12].

Table 4.1: Quantitative MT model parameters of an ex vivo muscle sample and in vivo human femoral muscle (vastus lateralis) derived from two-pool SSFP-FID model fitting.

| | SSFP-FID, muscle samp. | BSSFP, muscle samp. | SSFP-FID, muscle | Literature, muscle | Literature muscle |
|---|---|---|---|---|---|
| $T_{1,f}$ [ms] | $790 \pm 16^a$ | $790 \pm 16^a$ | $987 \pm 25^a$ | $1008 \pm 20^b$ | $1060 \pm 155^c$ |
| $T_{2,f}$ [ms] | $47.9 \pm 1.9^d$ | $51.2 \pm 2.2^e$ | $27.1 \pm 3.7^d$ | $44 \pm 6^b$ | $35 \pm 4^c$ |
| $F$ [%] | $10.5 \pm 0.6^d$ | $9.7 \pm 0.7^e$ | $10.7 \pm 1.7^d$ | $7.4 \pm 1.6^b$ | $8.3 \pm 1.6^f$ |
| $k_f$ [s$^{-1}$] | $5.2 \pm 0.4^d$ | $3.7 \pm 0.3^e$ | $4.0 \pm 1.2^d$ | $4.9 \pm 1^b$ | $3.6 \pm 0.4^f$ |

[a] Estimation based on DESPOT1 [22].
[b] Estimates from Stanisz et al. [21].
[c] Estimates from Gold et al. [25].
[d] Estimates based on two-pool SSFP-FID model fitting (Eqs. (4.10)-(4.11)).
[e] Estimates based on two-pool bSSFP model fitting [12].
[f] Estimates from Louie et al. [26].

Table 4.2: Quantitative MT model parameters of in vivo human patellar cartilage derived from two-pool SSFP-FID model fitting.

| | SSFP-FID, cartilage | Literature, cartilage |
|---|---|---|
| $T_{1,f}$ [ms] | $922 \pm 49^a$ | $1024 \pm 70^b$ |
| $T_{2,f}$ [ms] | $43.6 \pm 5.3^c$ | $30 \pm 4^b$ |
| $F$ [%] | $12.7 \pm 2.0^c$ | $17.1 \pm 2.4^b$ |
| $k_f$ [s$^{-1}$] | $6.5 \pm 1.1^c$ | $9.7 \pm 1.5^b$ |

[a] Estimation based on DESPOT1 [22].
[b] Estimates from Stanisz et al. [21].
[c] Estimates based on two-pool SSFP-FID model fitting (Eqs. (4.10)-(4.11)).

The results for human femoral muscle and human patellar cartilage are shown in Fig. 4.5. In addition to $T_{2,f}$, $F$ and $k_f$ a map of $T_{1,f}$ (based on DESPOT1) is shown. For reasons of completeness, an evaluation of MT effects in terms of MTR is shown as well. Quantitative MT parameters for vastus lateralis and patellar cartilage were compared to literature data from continuous off-resonance RF irradiation [16] or inversion recovery [11]. The corresponding results are summarized in Tables 4.1 and 4.2. For muscle, the two-pool SSFP-FID model yielded $T_{1,f}$, $F$ and $k_f$ values that correspond well with literature [21, 26]. However, $T_{2,f}$ values are lowered by 23-38 % [21, 26]. For cartilage, good correspondence in $T_{1,f}$ is observed with a previous study [21]. Found free pool relaxation rates ($T_{2,f}$) are
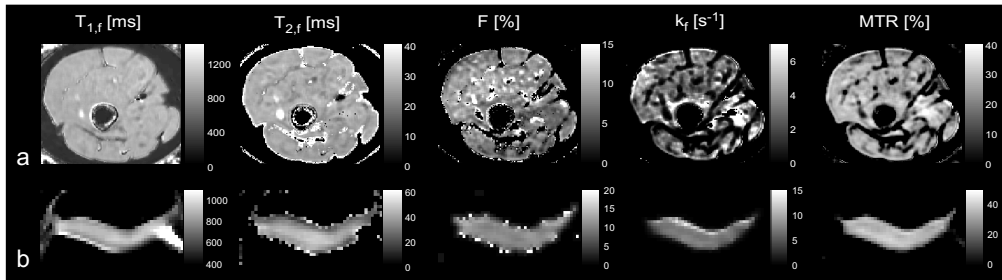
Figure 4.5: Axial images of (a) human femoral muscle ($1 \times 1 \times 3\,\text{mm}^3$ resolution) and (b) human patellar cartilage ($1 \times 1 \times 1.25\,\text{mm}^3$ resolution) of a healthy volunteer displaying the results of MT parameter estimation from a two-pool SSFP-FID signal analysis. $T_{1,f}$ maps were derived from DESPOT1, whereas $T_{2,f}$, the restricted pool fraction $F$ and the magnetization exchange rate $k_f$ were derived from fitting the two-pool SSFP-FID signal equation to a series of 3D SSFP-FID image acquisition, as illustratively displayed in Fig. 4.4 c. In addition, an MTR image was derived from two SSFP-FID image acquisitions ($\text{TR}_1$ and $\text{TR}_{10}$, see "Methods" section and [27]). Quantitative MT results for ROIs placed in vastus lateralis and patellar cartilage are listed in Tables 4.1 and 4.2.

consistent with those from Gold et al. [25], but increased by 41 % as compared to the ones from Stanisz et al. [21], whereas $F$ and $k_f$ values are lowered by 26 % and 32 %, respectively.

## 4.5   Discussion

Good correspondence between numerical simulations of the two-pool SSFP-FID model and its derived analytical expression was observed. The slight underestimation of the steady-state signal by Eq. (4.10) as compared to the numerical simulations is most likely due to neglected $T_2$ effects during excitation processes, as already observed with bSSFP [12]. As a result, proper extension of the SSFP-FID signal allowed for the assessment of quantitative MT parameter maps from various targets either ex vivo or in vivo. Generally, good correspondence between the parameters derived using SSFP-FID and literature values using common methods was observed. Some discrepancies were observed in $T_{2,f}$, which are most likely due to sequence specific weighting [6], whereas differences in $F$ and $k_f$ are presumably related to differences in the experimental conditions used (cited cartilage acquisitions were performed on in vitro bovine cartilage [21]). Muscle parameter fitting is critical in or around the fat and fascia as these regions exhibit either no MT (fat) or suffer from considerable partial volume effects (fascia), which may lead to wrong parameter estimates or even fitting failures (black spots, Fig. 4.5 a). Failures are less abundant for $T_{1,f}$ since these values are derived from a linear fit according to the DESPOT1 method, whereas for the $T_{2,f}$ map a simple one-pool model fit according to Eq. (4.3) was tried for all two-pool model fitting failures.

Balanced SSFP suffers from off-resonance related signal variation, typically

outside the range of $\varphi = 2/(3\,\mathrm{TR})$ [28]. Since derivation of quantitative MT parameters from a two-pool bSSFP model is based on a variation of $\mathrm{T_{RF}}$ (and thus of TR), banding artifacts may become an important issue for targets where high susceptibility variations can be expected. However, nonbalanced SSFP protocols are insensitive to constant dephasing and therefore might be suited to extend the concept of qMTI with SSFP-based sequences to targets of high susceptibility variations. It has been demonstrated that derivation of MT model parameters from a basic two-pool SSFP-FID signal model is feasible and is in accordance with literature for human femoral muscle and patellar cartilage. Nevertheless, caution must be paid on possible issues arising from its flow or motion sensitivity, which may complicate data acquisition.

Generally, analysis based on two-pool SSFP-FID offers a new and fast framework for qMTI, which is very well suited for in vitro samples, being completely insensitive to susceptibility variations. In contrast to bSSFP, however, unbalanced SSFP variants are motion sensitive. This is reflected by the increase in the signal variation for in vivo as compared to in vitro measurements. Generally, the use of SSFP-FID requires a good fixation of the target, what is feasible for the lower extremities, but may be an issue for other organs. Moreover, repeated acquisitions of the whole SSFP-FID signal curve seems advisable. Averaging of the acquisitions not only increases the signal to noise ratio but may also prevent signal fluctuations due to flow and motion that can lead to a falsification of the fit results. However, the additional time required for averaging may favor the use of bSSFP sequences for targets where a good overall shim can be achieved. For other targets, phase-cycled bSSFP might be a competing option. Unfortunately, correct signal estimates for a given flip angle using phase-cycled bSSFP, can only be attained if the maximum signal is achieved around on-resonance. As a result, for most tissues ($T_2/T_1 \approx 0.1$), measurements should be performed with flip angles exceeding approximately $30°$ [29]. Therefore, flip angle variation (see "Methods" section) cannot be performed, which is the main determinant for the $T_{2,f}$ estimate. A preceding $T_{2,f}$ calculation, however, makes it possible to estimate the bound proton fraction $F$ and the exchange rate $k_f$ from RF pulse elongation only (at a constant $\alpha$) [30]. Thereby, the acquisition time is reduced and this method will be of comparable speed as a qMTI protocol using averaged SSFP-FID acquisitions, assuming that no more than three to four phase cycles are needed. However, this requires (similar to $T_{1,f}$) a separate and accurate $T_{2,f}$ estimation to be used in the actual two-pool bSSFP model analysis.

In summary, SSFP based qMTI, either using balanced or nonbalanced protocols, offers the possibility for a fast estimation of MT model parameters with high resolution, typically within less than approximately 15 minutes. For ex-vivo targets, reliable results might be easily achieved with nonbalanced SSFP, whereas balanced SSFP is superior for targets of low susceptibility variation. All other targets will require testing which SSFP protocol will perform best, since it remains ambiguous whether averaging or phase-cycling might be more successful in overcoming possible issues from motion or off-resonances.

## 4.6 Conclusion

A new quantitative MT imaging method using a nonbalanced SSFP protocol was introduced. First, a modified SSFP-FID signal equation was derived based on a binary spin-bath model to include MT effects. Based on this model, it was exemplarily demonstrated that quantitative MT parameters such as the relaxation times, fractional pool size and magnetization exchange rates can be derived for human femoral muscle and patellar cartilage. While off-resonance induced dephasing leads to artifacts in bSSFP-based qMTI, this method is applicable for various targets irrespective of susceptibility differences. As SSFP-FID bares a strong flow and motion sensitivity, care has to be taken to ensure signal stability. Good fixation of the target and averaging enables the acquisition of high resolution quantitative MT maps with high signal-to-noise ratios and short acquisition times.

## References

[1] S. D. Wolff and R. S. Balaban. Magnetization Transfer Contrast (MTC) and Tissue Water Proton Relaxation in Vivo. *Magn Reson Med*, 10(1):135–44, 1989.

[2] R. M. Henkelman, G. J. Stanisz, and S. J. Graham. Magnetization Transfer in MRI: A Review. *NMR Biomed*, 14(2):57–64, 2001.

[3] R. C. Mehta, G. B. Pike, and D. R. Enzmann. Measure of Magnetization Transfer in Multiple Sclerosis Demyelinating Plaques, White Matter Ischemic Lesions, and Edema. *AJNR Am J Neuroradiol*, 17(6):1051–5, 1996.

[4] N. C. Silver, C. D. Good, G. J. Barker, D. G. MacManus, A. J. Thompson, I. F. Moseley, W. I. McDonald, and D. H. Miller. Sensitivity of Contrast Enhanced MRI in Multiple Sclerosis. Effects of Gadolinium Dose, Magnetization Transfer Contrast and Delayed Imaging. *Brain*, 120 ( Pt 7):1149–61, 1997.

[5] F. Palmieri, F. De Keyzer, F. Maes, and I. Van Breuseghem. Magnetization Transfer Analysis of Cartilage Repair Tissue: A Preliminary Study. *Skeletal Radiol*, 35(12):903–8, 2006.

[6] J. G. Sled and G. B. Pike. Quantitative Imaging of Magnetization Transfer Exchange and Relaxation Properties in Vivo Using MRI. *Magn Reson Med*, 46(5):923–31, 2001.

[7] C. Morrison and R. M. Henkelman. A Model for Magnetization Transfer in Tissues. *Magn Reson Med*, 33(4):475–82, 1995.

[8] A. Ramani, C. Dalton, D. H. Miller, P. S. Tofts, and G. J. Barker. Precise Estimate of Fundamental in-Vivo MT Parameters in Human Brain in Clinically Feasible Times. *Magn Reson Imaging*, 20(10):721–31, 2002.

[9] V. L. Yarnykh. Pulsed Z-Spectroscopic Imaging of Cross-Relaxation Parameters in Tissues for Human MRI: Theory and Clinical Applications. *Magn Reson Med*, 47(5):929–39, 2002.

[10] S. Ropele, T. Seifert, C. Enzinger, and F. Fazekas. Method for Quantitative Imaging of the Macromolecular 1H Fraction in Tissues. *Magn Reson Med*, 49(5):864–71, 2003.

[11] D. F. Gochberg and J. C. Gore. Quantitative Imaging of Magnetization Transfer Using an Inversion Recovery Sequence. *Magn Reson Med*, 49(3): 501–5, 2003.

[12] M. Gloor, K. Scheffler, and O. Bieri. Quantitative Magnetization Transfer Imaging Using Balanced SSFP. *Magn Reson Med*, 60(3):691–700, 2008.

[13] O. Bieri, T. C. Mamisch, S. Trattnig, and K. Scheffler. Steady State Free Precession Magnetization Transfer Imaging. *Magn Reson Med*, 60(5):1261–6, 2008.

[14] Y. Zur, S. Stokar, and P. Bendel. An Analysis of Fast Imaging Sequences with Steady-State Transverse Magnetization Refocusing. *Magn Reson Med*, 6(2):175–93, 1988.

[15] O. Bieri and K. Scheffler. On the Origin of Apparent Low Tissue Signals in Balanced SSFP. *Magn Reson Med*, 56(5):1067–74, 2006.

[16] R. M. Henkelman, X. Huang, Q. S. Xiang, G. J. Stanisz, S. D. Swanson, and M. J. Bronskill. Quantitative Interpretation of Magnetization Transfer. *Magn Reson Med*, 29(6):759–66, 1993.

[17] S. J. Graham and R. M. Henkelman. Understanding Pulsed Magnetization Transfer. *J Magn Reson Imaging*, 7(5):903–12, 1997.

[18] H.Y. Carr. Steady-State Free Precession in Nuclear Magnetic Resonance. *Phys. Rev.*, 112(5):1693–1701, 1958.

[19] R.R. Ernst. Application of Fourier Transform Spectroscopy to Magnetic Resonance. *Rev Sci Instrum*, 37(1):93–102, 1966.

[20] EM Haacke, RW Brown, MR Thompson, and R. Venkatesan. *Magnetic Resonance Imaging: Physical Principles and Sequence Design*. Wiley, 1999.

[21] G. J. Stanisz, E. E. Odrobina, J. Pun, M. Escaravage, S. J. Graham, M. J. Bronskill, and R. M. Henkelman. T1, T2 Relaxation and Magnetization Transfer in Tissue at 3T. *Magn Reson Med*, 54(3):507–12, 2005.

[22] S. C. Deoni, T. M. Peters, and B. K. Rutt. High-Resolution T1 and T2 Mapping of the Brain in a Clinically Acceptable Time with DESPOT1 and DESPOT2. *Magn Reson Med*, 53(1):237–41, 2005.

[23] J. Homer and J.K. Roberts. Conditions for the Driven Equilibrium Single Pulse Observation of Spin-Lattice Relaxation Times. *J Magn Reson*, 74: 424–432, 1987.

[24] S. Akoka, F. Franconi, F. Seguin, and A. Le Pape. Radiofrequency Map of an NMR Coil by Imaging. *Magn Reson Imaging*, 11(3):437–41, 1993.

[25] G. E. Gold, E. Han, J. Stainsby, G. Wright, J. Brittain, and C. Beaulieu. Musculoskeletal MRI at 3.0 T: Relaxation Times and Image Contrast. *AJR Am J Roentgenol*, 183(2):343–51, 2004.

[26] E. A. Louie, D. F. Gochberg, M. D. Does, and B. M. Damon. Transverse Relaxation and Magnetization Transfer in Skeletal Muscle: Effect of pH. *Magn Reson Med*, 61(3):560–9, 2009.

[27] O. Bieri and K. Scheffler. Optimized Balanced Steady-State Free Precession Magnetization Transfer Imaging. *Magn Reson Med*, 58(3):511–8, 2007.

[28] K. Scheffler, O. Heid, and J. Hennig. Magnetization Preparation During the Steady State: Fat-Saturated 3D TrueFISP. *Magn Reson Med*, 45(6): 1075–80, 2001.

[29] N. K. Bangerter, B. A. Hargreaves, S. S. Vasanawala, J. M. Pauly, G. E. Gold, and D. G. Nishimura. Analysis of Multiple-Acquisition SSFP. *Magn Reson Med*, 51(5):1038–47, 2004.

[30] M. Gloor, K. Scheffler, and O. Bieri. Accelerated Quantitative Magnetization Transfer Imaging Using Balanced SSFP. *In: Proc 25th Meeting ESMRMB 2008, Valencia*, 2008.

# Chapter 5

# Intra- and Inter-Scanner Variability of MT-Sensitized Balanced Steady-State Free Precession Imaging

## 5.1 Introduction

Magnetization transfer (MT) was introduced by Wolff and Balaban in 1989 [1] and has become a standard tool to suppress background signals from tissues in MR angiography [2]. Its potential for the understanding of various brain tissue degenerations has also been studied, predominantly in terms of magnetization transfer ratio (MTR) measurements. These measurements promise improved characterization of ischemic lesions, edema and myelin-related processes in multiple sclerosis [3–5].

Traditionally, spin-echo or gradient-echo (GRE) sequences with off-resonance saturation pulses are used to acquire MTR maps [1, 3]. As MTR values are potential markers for brain tissue integrity in various clinical settings, it is essential to estimate their reproducibility in normal brain matter. First intra-scanner MTR variability analyses were presented by Barker et al. [6]. A range of inter-site and inter-scanner MTR values were later reported by Berry et al. [7]. The definition of a standardized protocol for GRE-based MTR resulted in comparable results for several systems [8]. Remaining differences were reported to be mainly due to $B_1$ sensitivity [8, 9] and therefore, a correction scheme based on a $B_1$ map was suggested to significantly improve the reproducibility of inter-subject and inter-site variability [10].

Recently, a new and fast approach for MTR measurements was described [11] based on MT-sensitized balanced steady-state free precession (bSSFP). Macromolecular pool protons are saturated with the short radiofrequency (RF) pulses and short repetition times (TR) typically used for bSSFP, and the observed bSSFP signal is considerably reduced. A second acquisition with longer RF pulses and longer TR serves as reference image with almost full, i. e. unsaturated steady-state amplitude. As a result, whole brain bSSFP-MTR imaging benefits from a considerably reduced acquisition time or substantially improved signal-to-noise ratio (SNR) in comparison with a standard 3D GRE method.

In this study, the reproducibility and variability of bSSFP-MTR is assessed to derive a protocol for maximum stability. For this, the flip angle dependence of the MT effect in bSSFP was analyzed and optimal flip angles were chosen. Only limited MTR fluctuations are expected using these settings. Measurements in brain tissue of healthy volunteers were carried out at different systems and several sites. It will be shown that for optimal flip angle settings a very low variability between scans can be achieved, which is important for future MTR scans in a clinical setting.

## 5.2 Materials and Methods

### 5.2.1 Simulations

All numerical simulations, data analysis and visualization were done in Matlab 2007b (The MathWorks, Inc., Natick, MA). MTR values were simulated as a function of the flip angle using a two-pool bSSFP model as described in detail elsewhere [12] with $T_2$ values from [13] and quantitative MT parameters from
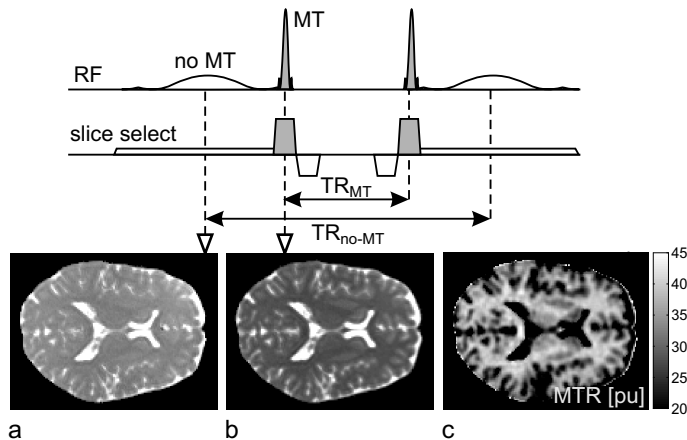
Figure 5.1: BSSFP sequence scheme for acquisition of MTR maps from RF pulse variation. (a) Long RF pulses (2.1 ms) and repetition times $TR_{non-MT}$ (4.8 ms) yield the full steady-state signal of brain tissue. (b) Short RF pulse durations (0.3 ms) and minimal repetition times $TR_{MT}$ (3.0 ms) attenuate the steady-state signal due to saturation of macromolecular pool protons. (c) MTR map derived from the difference between non-MT weighted and MT weighted image.

[12]. A range of flip angles was chosen around the maximum MTR value in order to minimize MTR variation arising from $B_1$ inhomogeneity.

## 5.2.2   Scanning

Experiments and calibrations were performed at 1.5 T on an Espree ($A$) and on an Avanto ($B$) system and at 3.0 T on a Verio system (Siemens Healthcare, Erlangen, Germany). For all scanners, the standard head coil of the manufacturer was used.

Intra-scanner MTR reproducibility was assessed from four consecutive scans of nine healthy volunteers ($V_1$, ..., $V_9$) performed on different days on both systems at site 1 ($A_1$, $B_1$). No care was taken to ensure that the position of the head was consistent with preceding scans. In order to estimate MTR variability between different scanners, nine healthy subjects ($V_1 - V_9$) were imaged on both scanners ($A_1$, $B_1$), and two of them ($V_6$, $V_7$) at six different sites ($A_{1-6}$, $B_{1-6}$: Basel, Zurich, Geneva, Freiburg, Munich, and Erlangen) within a half year period. This allowed for 19 comparisons of scanner $A$ and $B$ and 6 inter-site comparisons per scanner.

## 5.2.3   Pulse Sequence and Data Analysis

MT imaging was performed using a 3D bSSFP sequence (Fig. 5.1) with sagittal orientation. 144 slices were acquired with a thickness of 1.3 mm. The in plane resolution was 1.3 mm on scanner $B$ and if possible on scanner $A$ (fast gradient mode). Otherwise, 1.4 mm in plane resolution was used on scanner $A$. Slice-selective (sinc-shaped) RF pulses were used with a time-bandwidth product of 2.0.
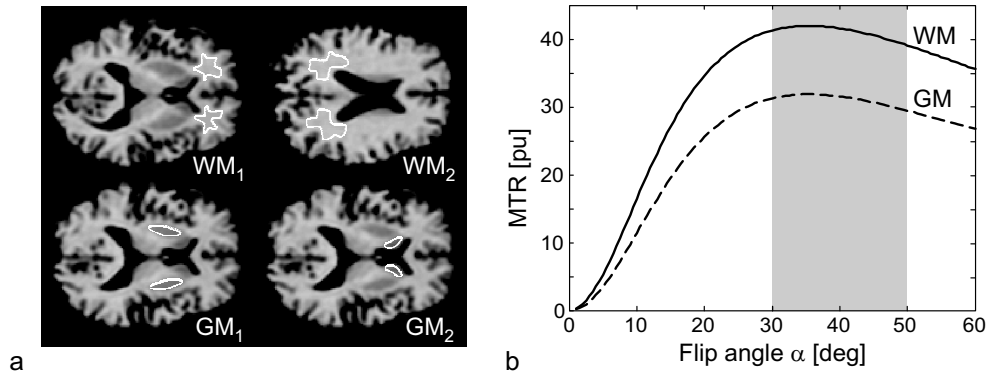
Figure 5.2: Reproducibility of MTR was assessed in four regions of interest (indicated in white): frontal white matter (WM$_1$), occipital white matter (WM$_2$), putamen (GM$_1$) and caudate nucleus (GM$_2$). (b) Simulation of bSSFP-MTR as a function of flip angle for white (solid line) and gray (dashed line) brain matter, using a two-pool bSSFP model [12], $T_2$ values from [13] and quantitative MT parameters from [12].

The receiver bandwidth was manually adapted in order to achieve the same TR on each scanner, and ranged from 700 to 900 Hz/Pixel. For the MT weighted bSSFP sequence, the pulse duration ($T_{RF}$) and the repetition time (TR) were minimized: $T_{RF} = 0.33$ ms and TR $= 3.01$ ms. These settings yield a maximum MT effect ($S_{MT}$, Fig. 5.1 b), whereas $T_{RF} = 2.10$ ms and TR $= 4.78$ ms result in a non-MT weighted image ($S_0$, Fig. 5.1 a). A whole brain MTR map using parallel imaging, partial Fourier and asymmetric echo was acquired within 1:19 min. The flip angles were varied between 30° and 50° in 5° steps to estimate $B_1$ sensitivity. The same resolution was used at 3.0 T with $T_{RF} = 0.6$ ms and TR $= 3.29$ ms for the MT-weighted and $T_{RF} = 2.10$ ms and TR $= 4.79$ ms the non-MT weighted scan in combination with a flip angle of 30° and a receiver bandwidth of 789 Hz/Pixel. Four images were acquired with different RF phase increments of -90°, 0°, 90°, and 180°.

Images were registered using the software packages FSL [14] and AFNI [15]. After image registration, MTR maps were calculated according to MTR $= 100 \cdot (S_0 - S_{MT})/S_0$ ([pu]: percentage units). Regions of interest were drawn in the first acquired MTR map of each volunteer and subsequently copied to the coregistered MTR maps. Finally, mean MTR values ($\langle$MTR$\rangle$ [pu]) and (absolute) standard deviations (SD [pu]) across both hemispheres were computed for frontal and occipital white matter (WM$_1$ and WM$_2$), putamen and caudate nucleus (GM$_1$ and GM$_2$) (Fig. 5.2 a). The reproducibility was assessed by the coefficient of variation ($c_v$).
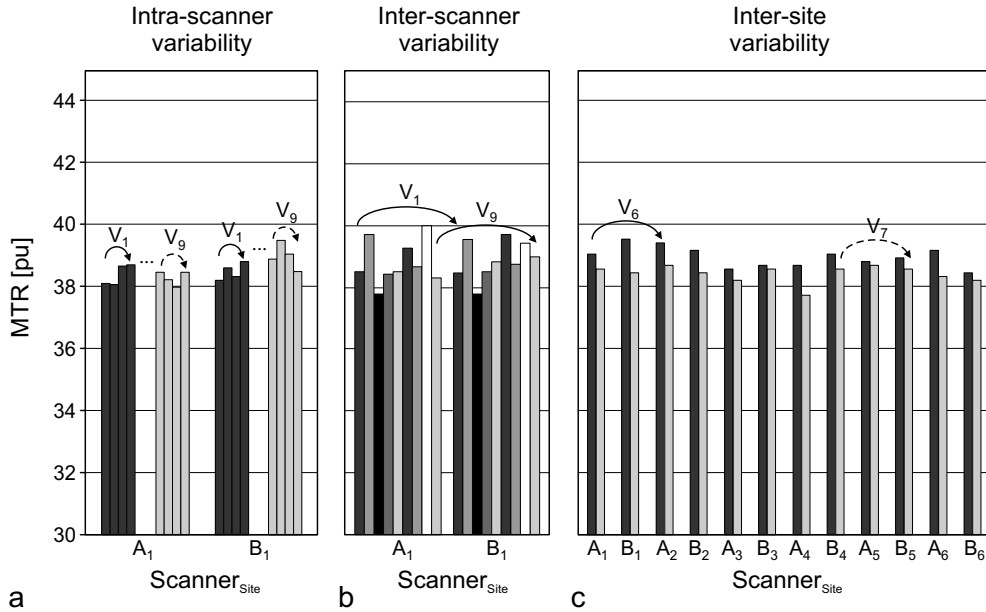
Figure 5.3: Intra-scanner variability of MTR was assessed with four consecutive acquisitions on nine healthy volunteers ($V_1$, ..., $V_9$) on both systems at site 1 ($A_1$, $B_1$). (b) MTR variability between different scanners was estimated from the same measurements on both scanners at site 1. (c) Two of them ($V_6$, $V_7$) were imaged on both systems and at six different sites ($A_{1-6}$, $B_{1-6}$). All values are displayed exemplarily for occipital white matter ($WM_2$).

## 5.3  Results

### 5.3.1  Simulations

Figure 5.2 b displays simulations of the MTR as a function of the flip angle for white matter (WM) and gray matter (GM). A considerable increase in saturation and thus in MTR is observed with increasing flip angles. For both WM and GM, maximum MT effects arise in the range of flip angles from 30° to 50°. Around this maximum, flip angle dependency, and thus $B_1$ sensitivity, is expected to be very limited. As a result, in the experiments, the flip angle was varied between 30° and 50° for reproducibility analyses.

### 5.3.2  In Vivo Measurements

Observed MTR values with a flip angle of 35° are exemplarily illustrated in Fig. 5.3 for occipital white matter ($WM_2$). Generally, low variation is found between repeated acquisitions. A detailed analysis is given in the following sections.

### 5.3.3  Intra-Scanner Variability

Variation between repeated MTR scans on volunteers $V_1$, ..., $V_9$ was very low (Fig. 5.3 a). White and gray matter MTR values from six acquisitions on the same volunteer using scanner $A$ are shown in Fig. 5.4 a. Intra-scanner variability is assessed by the mean $c_v$ between consecutive scans across four ROIs (Fig. 5.4 b). Within the range of experimentally applied flip angles, $c_v$ are below 0.016 for both systems. A restriction of the flip angle to $30°$ - $35°$ even leads to a $c_v$ of 0.011 or less, indicating a very good reproducibility.

### 5.3.4  Inter-Scanner Variability

Inter-scanner MTR measurements for volunteers $V_1$ to $V_9$ are shown in Fig. 5.3 b. Exemplary MTR curves from both systems are displayed in Fig. 5.4 c. Although the same volunteer was imaged, values from the two systems slightly differ. Coefficients of variation between scanner $A$ and $B$ were calculated for each volunteer separately and averaged across all volunteers and ROIs, yielding the curve shown in Fig. 5.4 d. For the lowest two flip angles inter-scanner $c_v$ are below 0.015.

### 5.3.5  Inter-Site Variability

Reproducibility of inter-site MTR values is presented in Fig. 5.3 c. Figure 5.4 e shows white and gray matter MTR curves from acquisitions on the same volunteer using the same scanner at six different sites. Inter-site variability is visualized by the mean $c_v$ between sites across four ROIs (Fig. 5.4 f). Again a choice of flip angles below $40°$ yields lowest $c_v$ of less than 0.017. Finally, white and gray matter MTR values from acquisitions on the same volunteer using both scanners at six different sites are plotted in Fig. 5.4 g. The mean $c_v$ for flip angles of $30°$ - $35°$ were below 0.016.

The optimized protocol consists of an MT weighted bSSFP sequence with $T_{RF}$ = 0.33 ms and TR = 3.01 ms and a non-MT weighted bSSFP sequence with $T_{RF}$ = 2.10 ms and TR = 4.78 ms. A flip angle of $35°$ is recommended for minimal variability.

## 5.4  Discussion

In bSSFP, the RF pulse train does not only generate the steady state but also saturates macromolecular pool protons, which exchange with free water protons. Therefore, an MT-weighted signal is formed without the insertion of additional saturation pulses, in contrast to the conventional GRE-based MTR sequence. As a result, the degree of freedom in imaging parameters is considerably reduced with MTR-bSSFP.

Simulations predict maximum MTR values at a flip angle of about $35°$ (Fig. 5.2 b). This maximum is the result of two concuring effects: On the one hand, saturation of macromolecular pool protons increases with increasing RF power, on the other hand, bSSFP signal amplitude decreases with high flip angles [11]. A choice of settings corresponding to the MTR plateau is indicated to be beneficial
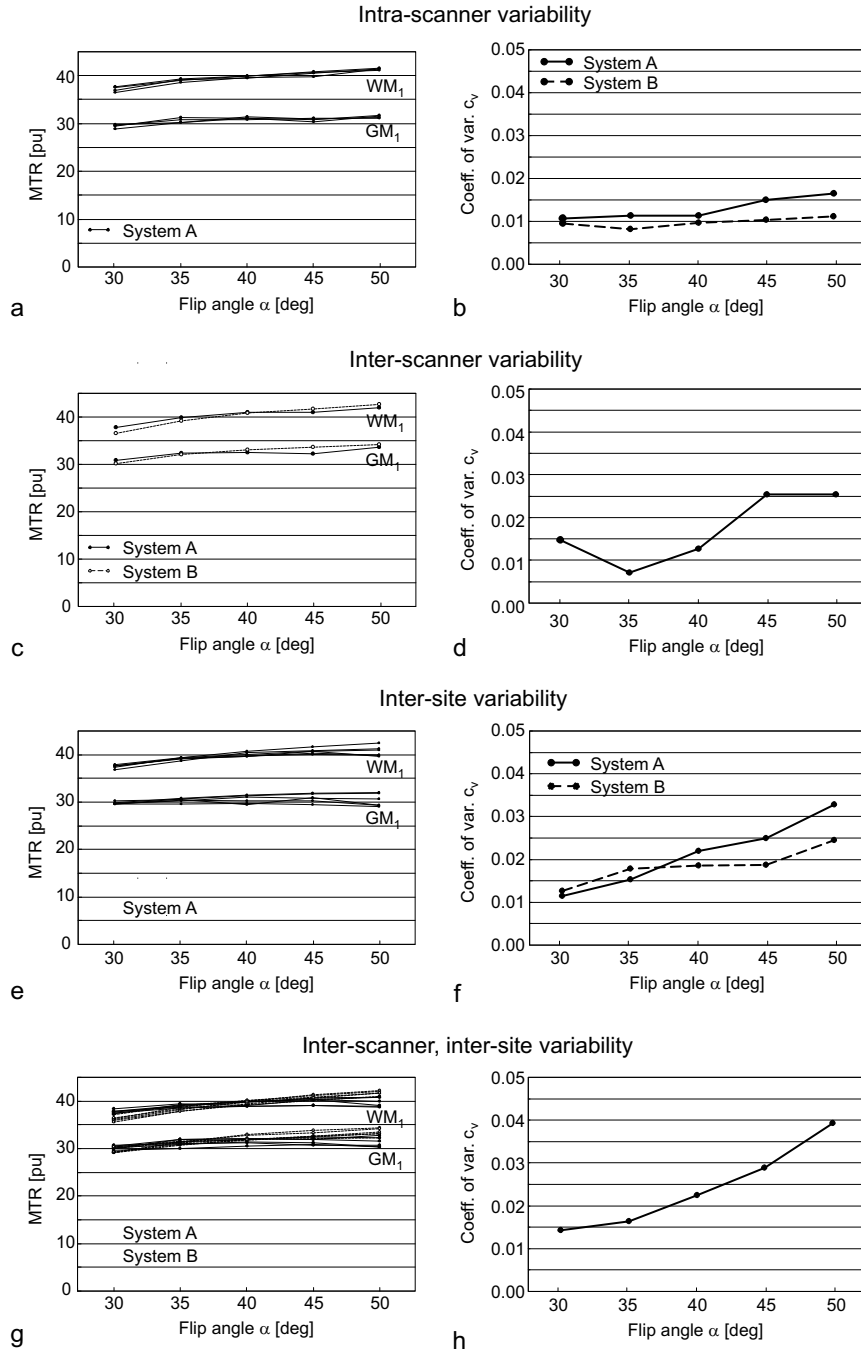
Figure 5.4: Results of MTR reproducibility as a function of flip angle. (a) Four consecutive MTR acquisitions on the same healthy volunteer on system $A_1$. (b) Intra-scanner coefficients of variation of nine volunteers across four different ROIs for both systems. (c) Exemplary MTR curves of the same volunteer at two different systems. (d) Inter-scanner coefficients of variation across nine volunteers and all ROIs. (e) Six MTR acquisitions on the same volunteer at six different sites (system $A$). (f) Inter-site coefficients of variation for both systems. (g) MTR of the one volunteer at six different sites (two different systems). (h) Inter-scanner, inter-site coefficients of variation across all volunteers and ROIs.

for stability (see Fig. 5.2). Thus, changes in $B_1$ either due to RF pulse imperfections or due to variations in subject positioning within the head coil only cause slight MTR deviations. As a result, intra-scanner coefficients of variation in this study were very low ($< 0.011$) although no attempt was made to reposition the volunteers perfectly (Fig. 5.4 b).

A slight discrepancy is observed between simulated and measured MTR values (Fig. 5.2 b and Figs. 5.4 a, c, e, g): experimental MTR values reach their maximum with higher flip angles than predicted from simulations. This is most likely attributed to additional compartments present in brain tissue. The two-pool model used represents only water and semisolid pool fractions, whereas more elaborated models consist of three or four pools (accounting also for myelin water and myelin semisolids) leading to an overall increase in signal with high flip angles [16].

It has been shown that in brain tissue $B_1$ errors of maximum 20% can be present [10]. In this extreme case, which will at the utmost affect the outer borders of the brain, the bSSFP-MTR variation averaged across all volunteers and ROIs amounts to about 4% for scanner $A$ and about 8% for scanner $B$, whereas GRE-based MTR variation was reported to be about 17% [10]. Slightly higher differences between the scanners and sites for higher flip angles (Fig. 5.4 d, f, h) may be due to scanner imperfections and bSSFP signal properties. For both white and gray matter, maximum MTR stability is observed for excitations near the optimal bSSFP flip angle $\alpha_{\mathrm{opt}} = 30° \text{ - } 35°$ ($\alpha_{\mathrm{opt}} = \cos^{-1}\left[(\epsilon - 1)/(\epsilon + 1)\right]$, $\epsilon = T_1/T_2$ [17]). The discrepancy in the $B_1$ field between the scanners only leads to a horizontal shift of MTR curves instead of a different slope as observed (Fig. 5.4 c, g). Also, $B_0$ effects can be ruled out as explanation of inter-scanner differences. Measurements at various off-resonance frequencies in the primary pass-band produced identical curves. In summary, the omission of a saturation pulse as well as the stability of MTR values around the optimal flip angle originate reduced $B_1$ sensitivity of bSSFP-MTR in comparison with GRE-based MTR.

In the present study, two types of 1.5 T scanners at six different sites were involved. However, application of bSSFP-MTR is not limited to 1.5 T and an exemplary measurement at 3 T is shown in Fig. 5.5. With increasing field strength, care has to be taken in regions of high susceptibility variation (Fig. 5.5 a, c). Banding artifacts become visible for slices near the sinuses and therefore MTR values are strongly reduced. This problem can be addressed by combining multiple bSSFP acquisitions with different RF phase increments [18]. As demonstrated in Fig. 5.5 b, d, maximum-intensity projection of four phase-cycled bSSFP scans very effectively removes banding artifacts to yield artifact free whole brain MTR maps at 3 T.

In accordance with theoretical predictions, experimental variability analyses propose the use of flip angles around 30° - 35° for bSSFP-MTR acquisitions. Measurements using these settings yielded coefficients of variation of less than 0.017 (Fig. 5.4 h) across different scanners and different sites. In addition to the high grade of reproducibility, this method benefits from the very short acquisition times, i. e. a factor four shorter than those of GRE-based MTR. Moreover, no $B_1$ mapping and correction is necessary with bSSFP-MTR. For these reasons, the presented optimized protocol is proposed for clinical MTR scans at individual
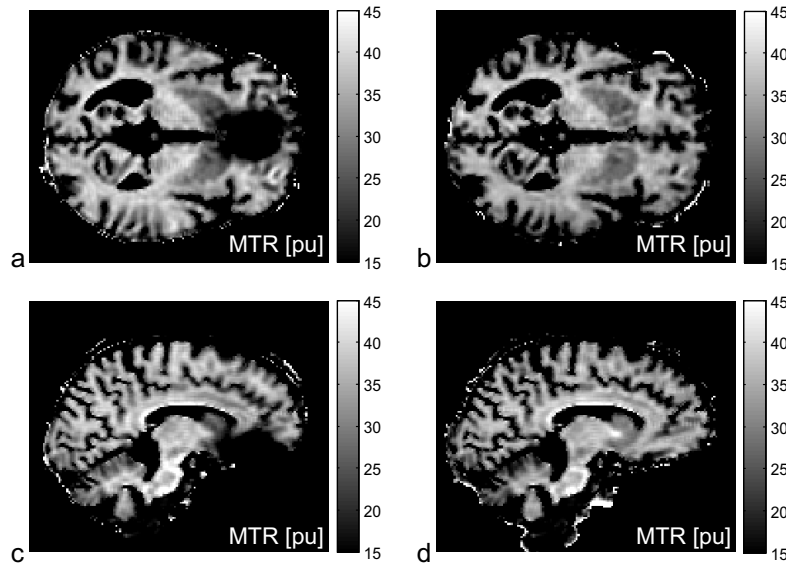
Figure 5.5: Exemplary bSSFP-MTR maps at 3 T in axial (a,b) and sagittal (c,d) view. A standard bSSFP-MTR scan (without phase-cycling) leads to considerably lowered MTR values in regions near the sinuses (a,c) from off-resonance. Combination of four phase-cycled bSSFP acquisitions yields an artifact free MTR map (b,d).

sites as well as for multi-center studies.

## 5.5   Conclusion

Reproducibility of a new and fast MTR mapping technique based on bSSFP sequences with modified RF pulses was studied at six different sites. Simulations of the MTR as a function of flip angle showed a broad plateau, where $B_1$ sensitivity is expected to be very limited. In agreement with the theoretical considerations, MTR values exhibited low intra-scanner, inter-scanner and inter-site variability at these flip angles. This demonstrates that accurate whole brain MTR mapping is possible without additional $B_1$ correction and within short acquisition times.

## References

[1] S. D. Wolff and R. S. Balaban. Magnetization Transfer Contrast (MTC) and Tissue Water Proton Relaxation in Vivo. *Magn Reson Med*, 10(1):135–44, 1989.

[2] R. M. Henkelman, G. J. Stanisz, and S. J. Graham. Magnetization Transfer in MRI: A Review. *NMR Biomed*, 14(2):57–64, 2001.

[3] V. Dousset, R. I. Grossman, K. N. Ramer, M. D. Schnall, L. H. Young, F. Gonzalez-Scarano, E. Lavi, and J. A. Cohen. Experimental Allergic En-

cephalomyelitis and Multiple Sclerosis: Lesion Characterization with Magnetization Transfer Imaging. *Radiology*, 182(2):483–91, 1992.

[4] R. C. Mehta, G. B. Pike, and D. R. Enzmann. Measure of Magnetization Transfer in Multiple Sclerosis Demyelinating Plaques, White Matter Ischemic Lesions, and Edema. *AJNR Am J Neuroradiol*, 17(6):1051–5, 1996.

[5] S. Ropele, A. Seewann, A. A. Gouw, W. M. van der Flier, R. Schmidt, L. Pantoni, D. Inzitari, T. Erkinjuntti, P. Scheltens, L. O. Wahlund, G. Waldemar, H. Chabriat, J. Ferro, M. Hennerici, J. O'Brien, A. Wallin, P. Langhorne, M. C. Visser, F. Barkhof, and F. Fazekas. Quantitation of Brain Tissue Changes Associated with White Matter Hyperintensities by Diffusion-Weighted and Magnetization Transfer Imaging: The Ladis (Leukoaraiosis and Disability in the Elderly) Study. *J Magn Reson Imaging*, 29(2):268–74, 2009.

[6] G. J. Barker, P. S. Tofts, and A. Gass. An Interleaved Sequence for Accurate and Reproducible Clinical Measurement of Magnetization Transfer Ratio. *Magn Reson Imaging*, 14(4):403–11, 1996.

[7] I. Berry, G. J. Barker, F. Barkhof, A. Campi, V. Dousset, J. M. Franconi, A. Gass, W. Schreiber, D. H. Miller, and P. S. Tofts. A Multicenter Measurement of Magnetization Transfer Ratio in Normal White Matter. *J Magn Reson Imaging*, 9(3):441–6, 1999.

[8] G. J. Barker, W. G. Schreiber, A. Gass, J. P. Ranjeva, A. Campi, J. H. van Waesberghe, J. M. Franconi, H. C. Watt, and P. S. Tofts. A Standardised Method for Measuring Magnetisation Transfer Ratio on MR Imagers from Different Manufacturers–the EuroMT Sequence. *Magma*, 18(2):76–80, 2005.

[9] P. S. Tofts, S. C. Steens, M. Cercignani, F. Admiraal-Behloul, P. A. Hofman, M. J. van Osch, W. M. Teeuwisse, D. J. Tozer, J. H. van Waesberghe, R. Yeung, G. J. Barker, and M. A. van Buchem. Sources of Variation in Multi-Centre Brain MTR Histogram Studies: Body-Coil Transmission Eliminates Inter-Centre Differences. *Magma*, 19(4):209–22, 2006.

[10] S. Ropele, M. Filippi, P. Valsasina, T. Korteweg, F. Barkhof, P. S. Tofts, R. Samson, D. H. Miller, and F. Fazekas. Assessment and Correction of B1-Induced Errors in Magnetization Transfer Ratio Measurements. *Magn Reson Med*, 53(1):134–40, 2005.

[11] O. Bieri and K. Scheffler. Optimized Balanced Steady-State Free Precession Magnetization Transfer Imaging. *Magn Reson Med*, 58(3):511–8, 2007.

[12] M. Gloor, K. Scheffler, and O. Bieri. Quantitative Magnetization Transfer Imaging Using Balanced SSFP. *Magn Reson Med*, 60(3):691–700, 2008.

[13] G. J. Stanisz, E. E. Odrobina, J. Pun, M. Escaravage, S. J. Graham, M. J. Bronskill, and R. M. Henkelman. T1, T2 Relaxation and Magnetization Transfer in Tissue at 3T. *Magn Reson Med*, 54(3):507–12, 2005.

[14] S. M. Smith, M. Jenkinson, M. W. Woolrich, C. F. Beckmann, T. E. Behrens, H. Johansen-Berg, P. R. Bannister, M. De Luca, I. Drobnjak, D. E. Flitney, R. K. Niazy, J. Saunders, J. Vickers, Y. Zhang, N. De Stefano, J. M. Brady, and P. M. Matthews. Advances in Functional and Structural MR Image Analysis and Implementation as FSL. *Neuroimage*, 23 Suppl 1:S208–19, 2004.

[15] R. W. Cox. AFNI: Software for Analysis and Visualization of Functional Magnetic Resonance Neuroimages. *Comput Biomed Res*, 29(3):162–73, 1996.

[16] S. C. Deoni, B. K. Rutt, T. Arun, C. Pierpaoli, and D. K. Jones. Gleaning Multicomponent T1 and T2 Information from Steady-State Imaging Data. *Magn Reson Med*, 60(6):1372–87, 2008.

[17] EM Haacke, RW Brown, MR Thompson, and R. Venkatesan. *Magnetic Resonance Imaging: Physical Principles and Sequence Design*. Wiley, 1999.

[18] N. K. Bangerter, B. A. Hargreaves, S. S. Vasanawala, J. M. Pauly, G. E. Gold, and D. G. Nishimura. Analysis of Multiple-Acquisition SSFP. *Magn Reson Med*, 51(5):1038–47, 2004.

# Chapter 6

# Clinical Applications of Magnetization Transfer Imaging Using Balanced SSFP

## 6.1 Characterization of Normal Appearing Brain Structures Using High-Resolution Quantitative Magnetization Transfer Steady-State Free Precession Imaging

### 6.1.1 Introduction

Magnetization transfer (MT) is based on the exchange of spin magnetization between protons in free water ("liquid pool") and those bound to larger molecules ("semisolid or solid pool") [1–4], thus providing information beyond conventional $T_1$- and $T_2$-magnetic resonance (MR) sequences. Although not belonging to the standard sequences in the daily clinical routine, studies characterizing the MT-effect in different pathologies, e.g. brain infarction, tumours and white matter (WM) lesions [3, 5–8] have been described. In its simplest form of quantification, MT effects are condensed into so-called magnetization transfer ratio (MTR) images being a rather qualitative measure for the quantity of bound protons present. Although MTR imaging is used in some centres in the clinical setting, it is difficult to be reproduced across different studies, as it highly depends on pulse sequence details and relaxation properties [1, 7, 9, 10]. Therefore, in characterizing the MT phenomenon by simply assessing MTR, potentially essential diagnostic information might be missed. In contrast to MTR, quantitative MT (qMT) imaging provides information about the magnetization transfer rate ($k_f$) between bound and free protons, and about the ratio ($F$) of the restricted pool size to the free pool size. In addition, qMT yields the $T_1$- and $T_2$-relaxation times [3, 11]. As qMT imaging (most commonly based on a two-pool MT model) reflects intrinsic tissue properties, it is believed to be more sensitive and specific to biological changes [3, 7–10, 12], and much less sensitive to sequence modifications [9, 11, 13]. So far, a number of imaging methods for qMT have been described in the literature that mainly differ in the state the magnetization is measured, that is: either in steady-state [2, 7, 13, 14] or during the transition to steady-state [4, 8, 15, 16]. However, clinical application of these methods is mostly limited by either low signal-to-noise ratio (SNR), long acquisition times, limited resolution or limited brain coverage and/or only permit the assessment of a few of the various parameters that can be obtained by qMT imaging. Only recently, a new MT-sensitized method, i.e. a fast imaging sequence based on balanced steady-state free precession (bSSFP) was proposed [17, 18], in which the addition of the MT-sensitizing off-resonance pulses prior to the proper MT measurement, indispensable in standard MT-SPGR methods, is not needed. Here, qMT imaging is based on a modification of the duration and the excitation angle of the radio-frequency (RF) pulses used. In contrast to common qMT imaging, bSSFP is able to produce high-resolution whole brain qMT parameter maps with high SNR within 30 minutes, hereby promising to be a good candidate for qMT analy-

sis in the clinical routine. For the establishment of a standardized high-resolution qMT reference data set for the interpretation of pathologies, normal appearing cerebral structures (12 WM and 11 grey matter (GM) structures) from 12 healthy volunteers were acquired with MT-sensitized bSSFP. Our results were compared with previously described quantitative MT-data acquired with markedly lower spatial resolution.

### 6.1.2 Materials and Methods

#### 6.1.2.1 Image Acquisition

All measurements were obtained at a 1.5 T MR whole body scanner (Avanto, Siemens Medical Solutions, Erlangen, Germany), equipped with a 12-channel head coil. Twelve healthy subjects (age range 26-45 years, 6 males and 6 females) underwent an imaging protocol including an axial unenhanced $T_1$-weighted turbo spin echo (TSE) sequence, an axial $T_2$-weighted TSE sequence, and an axial turbo inversion recovery magnitude (TIRM) sequence for anatomical exclusion of incidental findings, in addition to a sagittal 3D inversion recovery (IR) multi-planar magnetization prepared rapid acquisition gradient echo (MPRAGE) for anatomical reference. The MPRAGE acquisition and all qMT experiments were performed in 3D with a sagittal orientation based on a $144 \times 192 \times 192$ matrix and 1.3 mm isotropic resolution. QMT imaging included a multislice (16 slices, 5 mm slice thickness) $B_1$ map ($64 \times 64$ matrix, 4 mm in plane resolution) based on a stimulated echo sequence, two RF spoiled gradient echo (GRE) sequences with variable flip angles of $\alpha = 4°$ and $\alpha = 15°$ (TR/TE = 9.8 ms/4.77 ms) for $T_1$ mapping according to DESPOT1 [19, 20], and 16 bSSFP sequences using 8 different RF pulse durations ($\mathrm{T_{RF}} = 230\,\mu s - 2100\,\mu s$, $\alpha = 35°$) and 8 different flip angles ($\alpha = 5° - 40°$, $\mathrm{TR/T_{RF}} = 2.99\,ms/0.27\,ms$). Off-resonance related artifacts were reduced by manual shimming within the brain. Acquisition parameters are found in more detail elsewhere [21]. The qMT protocol was completed within 30 minutes.

#### 6.1.2.2 Image Post-Processing

Brain registration and segmentation were done with the software packages FSL [22] and AFNI [23]. Flip angle correction based on the $B_1$ field map, $T_1$ determination based on the RF spoiled GRE sequences and pixel-by-pixel non-linear least-squares fitting of the parameters $F$, $k_f$ and $T_2$ from the 16 bSSFP acquisitions were performed using Matlab 2006a (The MathWorks, Inc., Natick, MA). Theoretical derivation of the underlying equations are given elsewhere [21]. Twelve WM and eleven GM structures were identified and corresponding masks were drawn by an experienced radiologist, covering:

1. deep WM and cortical GM bilaterally for all four lobes (frontal, temporal, parietal, occipital),

2. the head of the caudate nucleus, the putamen, the globus pallidus, the thalamus, the mamillary body, the amygdala, the hippocampus, the crus
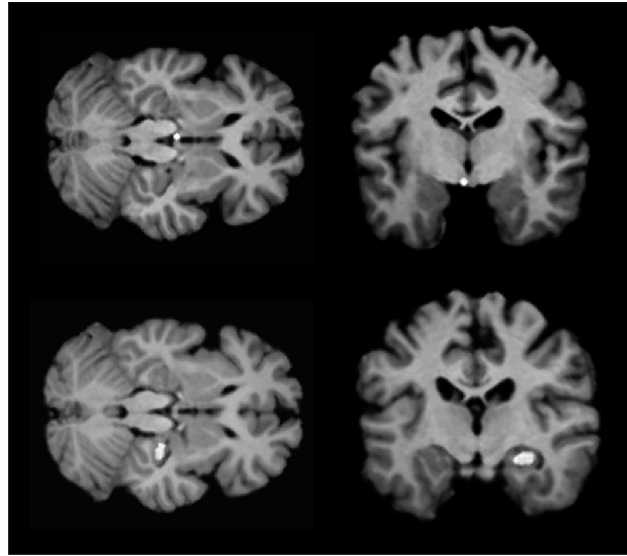
Figure 6.1: Axial (left) and coronal (right) images showing masks located in the left mamillary body (upper row) and right hippocampus (lower row).

cerebri, and the anterior and posterior limb of the internal capsule (IC) bilaterally, and as midline structures,

3. the anterior commissure and the four different parts of the corpus callosum (CC) (rostrum, genu, body and splenium).

For the frontal, temporal and occipital lobes, masks were created at the transition from the superior to the medial gyrus and sulcus, whereas the masks for the parietal lobe were drawn at the transition from the parietal lobulus to the angular gyrus. The lateral borders of the cortical GM masks were omitted to avoid inclusion of extracerebral or adjacent WM tissue. For all other cerebral structures, masks were slightly reduced by their anatomical margins to avoid partial volume effects from adjacent tissue or cerebral spinal fluid. All masks were drawn for each subject individually using FSL (FSL, Oxford, UK, www.fmrib.ox.ac.uk/fsl), and were of approximately the same size for all subjects. Special care was taken to draw the bilateral masks as symmetrically as possible in both hemispheres within the same as well as between all subjects. All masks were reviewed by a second experienced radiologist for proper anatomical localization and size. Examples of masked WM and GM structures are presented in Figure 6.1. Application of masks on qMT data was performed using Matlab (The MathWorks, Inc., Natick, MA, USA), yielding the quantitative two-pool MT model parameters $F$ and $k_f$, as well as the free pool relaxation times $T_1$ and $T_2$ (Fig. 6.2). In addition, mean values for WM, GM, IC and CC (calculated as the mean values of all contributing structures) are given in Table 6.1.

Figure 6.2: parametric maps in the axial (upper row), coronal (middle row), and sagittal (lower row) view, obtained from a healthy subject by the bSSFP method.
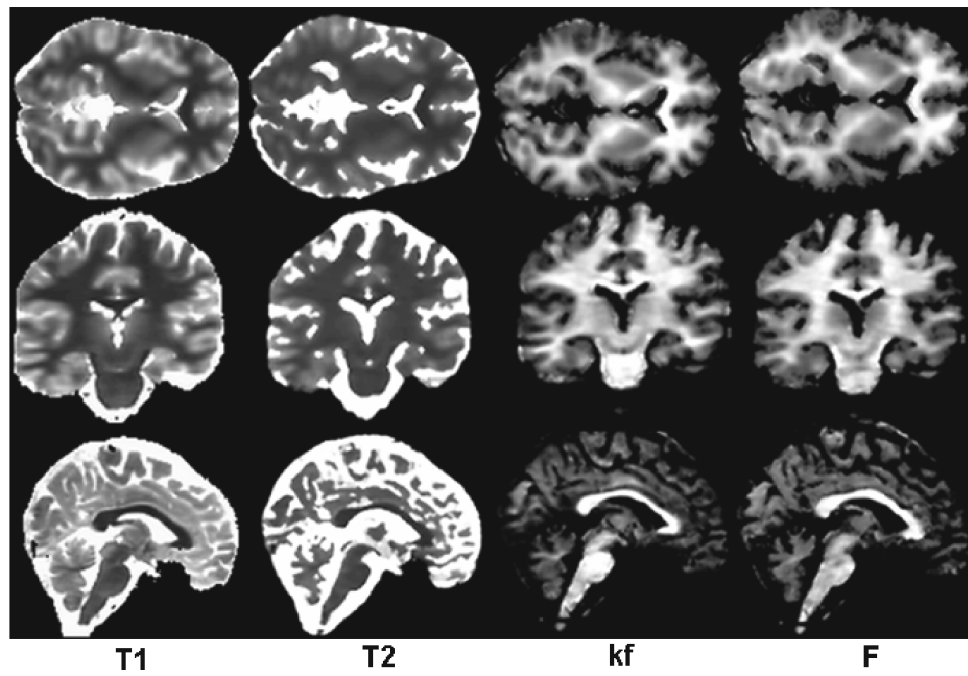
### 6.1.2.3  Statistical Analysis

For statistical analysis of results, two series of a two-way analysis of variances (ANOVA) factored into side of hemisphere (right/left) and structures (first series) and into structures and subjects (second series) were performed for each parameter ($F$, $k_f$, $T_1$, $T_2$) and type of tissue (WM and GM). A p-value of less than 1% was considered to be statistically significant.

For testing for differences between male and female patient for all parameters and for all structures, the Mann-Whitney U test was used, as normality could not be assumed. A p-value of $< 0.1$ indicated statistical difference.

For evaluation of the distribution of all brain structures and for comparison between and within WM and GM structures, a box-and-whisker plot for each parameter ($F$, $k_f$, $T_1$, $T_2$) was performed (Fig. 6.3). Hereby the box plot shows the median as the horizontal line inside the box and the inter-quartile range (25th to 75th percentiles) as the length of the box. The whiskers are the lines extending from the top and bottom of the box. Differences between structures were defined when the supposed horizontal extension of the median of one box was beyond the notch of the box of the structure to be compared with.

For comparison of $F$- and $k_f$-values among different studies [11, 13], the respective relative values were compared.

### 6.1.3  Results

Quantitative MT model parameters ($T_1$, $T_2$, $F$, $k_f$) averaged over the subjects are summarized in Table 6.1 for all brain structures investigated. The Mann-Whitney U-test showed no significant gender difference for all parameters and for each structure (data not shown). Differences between and within WM and GM structures for all parameters are graphically presented as box-whisker-plots (Fig. 6.3).

The first series of ANOVA showed no significant effect between hemispheres for all assessed parameters ($T_1$, $T_2$, $F$, $k_f$). In contrast, the second series of ANOVA showed significant inter-subject effects across the 12 subjects investigated for all assessed parameters (data not shown).

As expected, the highest differences were observed between the brain structures. Both series of ANOVA showed significant differences for all parameters between WM and GM structures, whereby, as expected, GM structures showed generally lower $F$- and $k_f$-values but longer $T_1$ and $T_2$ relaxation times than WM structures. Also within the WM and GM structures, respectively, several significant differences in $T_1$, $T_2$, $F$, and $k_f$ were observed (Fig. 6.3), as more precisely illustrated in the next sections.
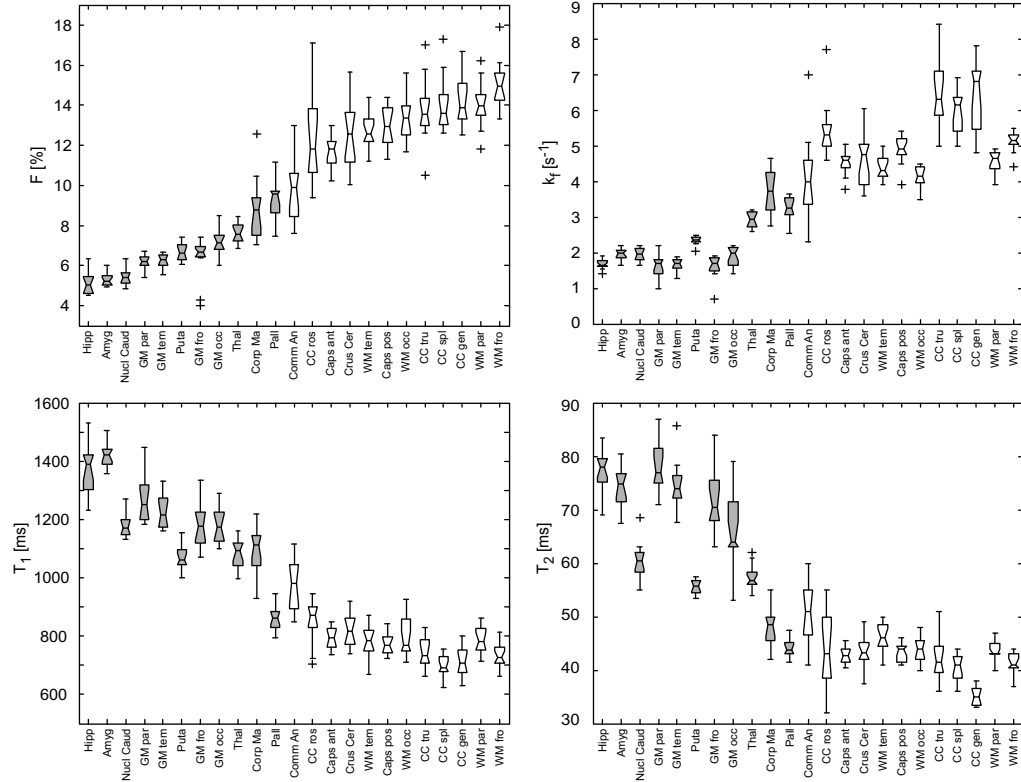
Figure 6.3: Box-and-whisker plots for each parameter ($F$, $k_f$, $T_1$, $T_2$) showing the distribution of all brain structures. The horizontal line inside the box represents the median and the length of the box the inter-quartile range (25th to 75th percentiles). The whiskers are the lines extending from the top and bottom of the box. Outlying values localized between 1.5 and 3 box lengths from the upper and lower edge of the box are shown as crosses. Differences between structures were defined when the supposed horizontal extension of the median of one box was beyond the notch of the box of the structure to be compared with.

Table 6.1: Quantitative MT parameter estimates for all evaluated WM and GM brain structures. Given are the mean and standard deviation (±SD).

| Structures | $T_1[\mathrm{ms}]^a$ | $T_2[\mathrm{ms}]^a$ | $F[\%]^a$ | $k_f[1/s]^a$ | $T_1[\mathrm{ms}]^b$ | $F[\%]^b$ | $k_f[1/s]^b$ | $T_1[\mathrm{ms}]^c$ | $F[\%]^c$ | $k_f[1/s]^c$ |
|---|---|---|---|---|---|---|---|---|---|---|
| WM: frontal | $734 \pm 13$ | $41 \pm 1$ | $15.0 \pm 0.3$ | $5.1 \pm 0.1$ | $578 \pm 0.1$ | $12.7 \pm 1.1$ | $4.3 \pm 0.4$ | 668 | $13.3 \pm 1.6$ | $3.4 \pm 0.6$ |
| WM: occipital | $796 \pm 18$ | $44 \pm 1$ | $13.4 \pm 0.3$ | $4.1 \pm 0.1$ | $588 \pm 0.1$ | $12.0 \pm 0.9$ | $3.7 \pm 0.4$ | 669 | $12.5 \pm 2$ | $3.3 \pm 0.8$ |
| WM: parietal | $788 \pm 13$ | $44 \pm 1$ | $14.0 \pm 0.3$ | $4.5 \pm 0.1$ | | | | | | |
| WM: temporal | $782 \pm 16$ | $46 \pm 1$ | $12.8 \pm 0.2$ | $4.4 \pm 0.1$ | | | | | | |
| WM: mean | $775 \pm 15$ | $44 \pm 1$ | $13.8 \pm 0.3$ | $4.5 \pm 0.1$ | | | | | | |
| CC rostrum | $852 \pm 73$ | $44 \pm 7$ | $12.4 \pm 2.3$ | $5.5 \pm 0.8$ | | | | | | |
| CC genu | $714 \pm 47$ | $35 \pm 2$ | $14.2 \pm 1.3$ | $6.5 \pm 1.0$ | $518 \pm 0.1$ | $14.2 \pm 1.1$ | $5.0 \pm 0.4$ | 647 | $17.2 \pm 1.8$ | $3.3 \pm 0.5$ |
| CC truncus | $743 \pm 55$ | $42 \pm 5$ | $13.7 \pm 1.6$ | $6.5 \pm 1.1$ | | | | | | |
| CC splenium | $698 \pm 42$ | $41 \pm 3$ | $14.0 \pm 1.4$ | $6.0 \pm 0.6$ | $549 \pm 0.1$ | $12.7 \pm 1.4$ | $3.9 \pm 0.7$ | 670 | $16.0 \pm 1.7$ | $3.3 \pm 0.5$ |
| CC mean | $752 \pm 54$ | $41 \pm 4$ | $13.6 \pm 1.7$ | $6.1 \pm 0.9$ | | | | | | |
| Crus cerebri | $822 \pm 17$ | $44 \pm 1$ | $12.5 \pm 0.5$ | $4.6 \pm 0.2$ | | | | 746 | $10.5 \pm 1.2$ | $3.7 \pm 1.2$ |
| IC ant. limb | $815 \pm 12$ | $42 \pm 1$ | $10.5 \pm 0.2$ | $4.2 \pm 0.1$ | $610 \pm 0.1$ | $10.6 \pm 1.3$ | $3.9 \pm 0.6$ | 724 | $12.9 \pm 1.6$ | $3.0 \pm 0.6$ |
| IC post. limb | $773 \pm 10$ | $43 \pm 1$ | $13.0 \pm 0.3$ | $4.9 \pm 0.1$ | $585 \pm 0.1$ | $12.0 \pm 1.0$ | $3.7 \pm 0.5$ | 721 | $10.7 \pm 1.2$ | $3.7 \pm 0.8$ |
| IC mean | $794 \pm 11$ | $43 \pm 1$ | $11.7 \pm 0.3$ | $4.5 \pm 0.1$ | | | | | | |
| Commisura ant. | $975 \pm 92$ | $51 \pm 6$ | $9.7 \pm 1.6$ | $4.1 \pm 1.2$ | | | | 752 | $13.6 \pm 1.9$ | $2.7 \pm 0.6$ |
| GM: frontal | $1178 \pm 23$ | $74 \pm 3$ | $6.3 \pm 0.3$ | $1.6 \pm 0.1$ | $1031 \pm 0.1$ | $6.4 \pm 0.5$ | $2.3 \pm 0.3$ | | | |
| GM: occipital | $1179 \pm 17$ | $66 \pm 2$ | $7.1 \pm 0.2$ | $1.9 \pm 0.1$ | $935 \pm 0.1$ | $7.0 \pm 0.5$ | $2.3 \pm 0.3$ | | | |
| GM: parietal | $1267 \pm 22$ | $78 \pm 1$ | $6.2 \pm 0.1$ | $1.6 \pm 0.1$ | | | | | | |
| GM: temporal | $1280 \pm 23$ | $80 \pm 1$ | $5.4 \pm 0.1$ | $1.6 \pm 0.1$ | | | | | | |
| GM: mean | $1226 \pm 21$ | $75 \pm 2$ | $6.3 \pm 0.2$ | $1.7 \pm 0.1$ | | | | 1285 | $6.8 \pm 1.4$ | $1.2 \pm 0.3$ |
| Globus pallidus | $861 \pm 12$ | $44 \pm 1$ | $9.2 \pm 0.3$ | $3.3 \pm 0.1$ | | | | 876 | $8.7 \pm 0.8$ | $2.1 \pm 0.5$ |
| Corpora mamillaria | $1090 \pm 22$ | $48 \pm 1$ | $8.8 \pm 0.4$ | $3.7 \pm 0.2$ | | | | | | |
| Thalamus | $1087 \pm 14$ | $57 \pm 1$ | $7.6 \pm 0.1$ | $2.9 \pm 0.1$ | | | | 1005 | $8.7 \pm 0.9$ | $2.0 \pm 0.5$ |
| Putamen | $1068 \pm 12$ | $56 \pm 0$ | $6.7 \pm 0.1$ | $2.4 \pm 0.0$ | $847 \pm 0.1$ | $7.0 \pm 0.4$ | $2.5 \pm 0.2$ | 1055 | $7.6 \pm 0.8$ | $1.5 \pm 0.3$ |
| Caput ncl. caudatus | $1179 \pm 11$ | $61 \pm 1$ | $5.4 \pm 0.1$ | $2.0 \pm 0.1$ | $990 \pm 0.1$ | $6.2 \pm 0.7$ | $1.7 \pm 0.3$ | 1122 | $7.2 \pm 0.8$ | $1.4 \pm 0.2$ |
| Amygdala | $1420 \pm 12$ | $74 \pm 1$ | $5.3 \pm 0.1$ | $2.0 \pm 0.2$ | | | | | | |
| Hippocampus | $1371 \pm 23$ | $77 \pm 1$ | $5.1 \pm 0.2$ | $1.7 \pm 0.2$ | | | | | | |

WM = white matter, GM = grey matter, CC = corpus callosum, IC = internal capsule, ant. = anterior, post. = posterior, ncl. = nucleus.

[a] This study: Sequence: 3D-bSSFP, Resolution: 1.3 mm isotropic, Acquisition time < 30 min. [b] Sled et al. [11]: Sequence: 2D-SPGR, Resolution: $2 \times 2 \times 7\,\mathrm{mm}^3$, Acquisition time < 35 min. [c] Yarnykh et al. [13]: Sequence: 3D-SPGR, Resolution: $1.4 \times 2.3 \times 2.8\,\mathrm{mm}^3$, Acquisition time: 30 min.

### 6.1.3.1 Fractional Pool Size ($F$)

Highest $F$-values were observed in the CC (WM structure) and deep WM, whereas the lowest $F$-value was found in the hippocampus (GM structure). Within the deep WM significances were observed between following regions: frontal vs. occipital and temporal, and parietal vs. temporal. For the GM structures differences were found between the following regions of the cortex: parietal vs. frontal and occipital, and temporal vs. occipital. Within the different parts of the CC significances were found between the rostrum and genu. There was no significant difference for $F$ between the posterior and anterior limb of the IC.

Within the GM highest $F$ were found in the pallidum and corpora mamillaria. These values were significantly higher than the $F$-values of all other GM structures.

### 6.1.3.2 Exchange Rate ($k_f$)

The highest values for $k_f$ were observed in the genu, truncus and splenium of the CC that were significantly higher than the $k_f$-values of all other WM structures. Within the GM, lowest $k_f$ were found in the hippocampus and the cerebral cortex of the parietal, temporal and frontal lobes.

Within the deep WM, significances could be observed between the following lobes: frontal vs. occipital, temporal and parietal, respectively, as well as parietal vs. occipital. For the cortex, no significant differences were observed between any regions. Within the CC, $k_f$ was significantly lower in the rostrum compared to all the other parts of the CC. Contrary to $F$, a significant difference could be observed for the $k_f$ of the IC, where the posterior limb showed significantly higher values than the anterior limb.

Within the GM, highest $k_f$ was observed in the corpora mamillaria, followed by the pallidum and thalamus.

### 6.1.3.3 $T_1$ Relaxation Time

Longest $T_1$-values were found in the amygdala, followed by the hippocampus, whereby their $T_1$-values were significantly longer than the corresponding values of all the other GM structures. Shortest $T_1$ were observed in the splenium and genu of the CC. Within the WM, the frontal WM showed significantly shorter $T_1$ than the occipital, parietal and temporal WM. For the cortex, significances were observed between the parietal and all the other three GM regions. The rostrum of the CC showed significantly longer $T_1$ than all the other parts of the CC. $T_1$-values of the anterior limb compared to the posterior limb of the IC did not reach significant differences. The commissura anterior was the only WM structure showing a $T_1$ exceeding the one of a GM structure, in this case of the pallidum, and this difference was significant.

#### 6.1.3.4   $T_2$ Relaxation Time

$T_2$-values were longest in the hippocampus, parietal GM and amygdala and lowest in the genu of the CC. Within the WM all matched regional pairs showed significant differences except for the occipital vs. the parietal and temporal lobes. For the cortical GM, following matched pairs showed significant differences: occipital vs. frontal, parietal and temporal, respectively, as well as frontal vs. parietal. Within the CC, $T_2$ was significantly shorter in the genu than in all the other regions of the CC. No significant difference could be observed between the anterior and posterior limb of the IC. The commissura anterior was the only WM structure showing significantly longer $T_2$ than the GM structures with the shortest $T_2$, i.e. the pallidum and corpora mamillaria. In general, a higher number of significant differences were observed within the GM structures as compared to the WM structures.

### 6.1.4   Discussion

In a preliminary study examining the feasibility of high-resolution MT-sensitized bSSFP in humans [21], qMT-values of gross WM and GM structures were within the expected range as known from established spoiled gradient echo (SPGR) methods using MT sensitizing preparation pulses with significantly lower resolution. In this study, a more detailed analysis was performed evaluating qMT-data from 42 brain structures in healthy volunteers, including very small and subtle brain structures that could not have been reliably examined before, like e. g. the corpora mamillaria and the hippocampus, with the aim to establish a high-resolution normal data set that might serve as a reference for the characterization of qMT in pathologic brain tissue in the future.

In general and as expected, $F$- and $k_f$-values were higher and relaxation times shorter in WM than in GM structures. Although the irradiation concept of the presented method obviously differs from common qMT techniques, $F$- and $k_f$-values are expected to be similar since they are derived from the same underlying two-pool model. For the bigger structures our MT parameters were overall in good accordance to the existing literature [1, 7, 11, 13]. Significant differences between MT parameters of smaller structures can be explained by partial volume effects. Relaxation times, on the other hand, of all brain regions differ from a part of previously published values. Our $T_1$-values are in the same range as those of Stanisz et al. [24] but higher than those of Sled et al. and Yarnykh et al. [11, 13]. This is probably due to sequence specific weighting. The $T_2$-values are in agreement with those of Sled et al. [11], but lower than those of Stanisz et al. [24]. In addition to the dependency on acquisition parameters, it has to be considered that the $T_2$-values presented in this MT framework correspond the free pool only ($T_{2,f}$). It has previously been observed that $T_{2,f}$ estimates are generally lower than $T_2$-values of MT-independent methods [24].

In contrast to previous studies, the isotropic resolution of $1.3\,\mathrm{mm}$ obtained with MT-based bSSFP enabled even a reliable assessment of quantitative parameters in very small structures, such as the hippocampus, with a low standard deviation. Furthermore, SNR for bSSFP is considerably increased as compared

to GRE [1]. A higher relative number of significant differences were found within GM as compared to WM structures, most likely due to smaller standard deviations in $F$ and $k_f$ in combination with a broader range of relaxation times reflecting a higher diversity. Significant differences in all qMT parameters were observed between the 12 subjects examined. This observation indicates that when applying qMT imaging each subject should be evaluated individually. The subject effect in the ANOVA is unlikely due to differences in acquisitions but most probably a result of slightly different ROI selection and the limited number of subjects. In addition, the data suggest that in patients with a one hemispheric pathology, qMT comparison with the non-affected hemisphere might be more accurate than with the same sided hemisphere of a healthy subject. Due to the high number of structures evaluated, only some of the most notable findings will be discussed in the following section.

Within WM and GM structures, respectively, many significant differences for all parameters could be observed. In addition, despite the overall higher relaxation times in GM tissue, the anterior commissure (WM structure) showed significantly longer $T_1$ and $T_2$ than the pallidum (GM structure), reflecting the complexity of brain tissue composition. Although both the pallidum and the putamen belong to the nucleus lentiformis, all parameters showed significant differences between the two structures. On the other side, the hippocampus and the amygdala, the two central components of the limbic system, showed no difference in $F$, $T_1$, and $T_2$, but significant differences in $k_f$.

Myelin water assessment has been widely described to be an indirect measure of myelinated tissue [25–29], and $F$ has been hypothesized to correlate with myelination [10, 15]. Thus the amount, size, and kind of axons, as well as differences in myelin density among the single WM structures may be an explanation for the regional differences in qMT model parameters observed within the assessed brain structures.

Limitations of this study include the small number of subjects examined, as well as their narrow age range (26-45 years), preventing a subdivision of the patient pool into different age ranges. Mehta et al. [30] did not observe any significant differences in MTR-values across different age groups, indicating that MTR may be a quite stable parameter. However, further and larger studies are required in order to verify whether this hypothesis can also be applied to qMT.

In this study, $k_f$ showed a higher stability than $F$ in both WM and GM. Compared to other methods [1, 3, 7], the $T_2$ relaxation time of the restricted pool protons $(T_{2,r})$ can not be determined by bSSFP-based qMT imaging and is treated as a fixed model parameter. The effect of this fixed parameter on MT parameter estimation has been studied [21]. Whereas $F$ is strongly sensitive to changes in $T_{2,r}$, $k_f$ shows only limited variation leading to higher stability and smoothness of $k_f$ maps. This is in contrast to observations by Yarnykh et al. [14], where $k_f$ appeared to be more sensitive to variations in fixed parameters. Another point that has to be considered using bSSFP is the strong off-resonance sensitivity. It has been shown that field variations of less than $20\,\mathrm{Hz}$ are achieved from a manual shim within the brain and that the impact on the bSSFP signal analysis is very limited [21].

The possible benefits and diagnostic potential of qMT as compared to standard MRI need further analysis and investigation. Initial results on patients using an optimized bSSFP-protocol with an acquisition time of less than 15 minutes indicate that qMT is applicable in the clinical routine. Since for patients only the affected brain structures have to be analyzed, postprocessing is limited. First results on reproducibility [21] brain tumors [31] and stroke [32] seem to be very promising.

In summary, this study shows that qMT evaluation with bSSFP is possible in even very small structures due to its high resolution in clinically feasible acquisition times. The analysed qMT-data obtained in this study with high SNR might serve as a reference baseline data set for future qMT characterization of pathologies of the brain. The high diversity of qMT parameter values in WM and GM tissue challenges the impact of MT assessment via qualitative MTR, indicating that qMT might be the more accurate method for MT assessment in altered brain tissue.

### 6.1.5  Conclusion

This study provides high-resolution 3D normative qMT-data in clinically feasible acquisition times and might thus be an adequate candidate for qMT analysis in the clinical environment. The differences between studies can be partly attributed to the reduced partial volume effects as achieved with bSSFP. Regional variations in relaxation times $(T_1, T_2)$ and MT estimates $(F, k_f)$ demonstrate the complexity of brain tissue composition and the singularity of each parameter, indicating that qMT might be a more accurate method for MT assessment in altered brain tissue than simple qualitative MTR.

## 6.2  Analysis of Brain Tumors and Metastases by Quantitative MT Imaging with BSSFP: Initial Experiences

### 6.2.1  Introduction

Conventional MRI is highly sensitive for the detection of abnormalities of the CNS (central nervous system), but lacks of specificity for their pathological substrates. For instance, conventional sequences do not allow an evaluation of the extent of lesioned tissue appearing normal on conventional MRI [33]. Magnetization transfer ratio (MTR) imaging techniques have been shown to be useful for the characterization of brain tissue [34], e. g. for the evaluation of WM (white matter) diseases as well as in differentiating low-grade from high-grade gliomas and benign from malignant tumors. For metastatic disease, MTR-values of brain lesions indicate structural changes beyond the extent of the lesions seen on standard MR images [35].

In contrast to the rather semi-quantitative MTR methods, quantitative MT (qMT) imaging yields information about the exchange rate between free and bound protons ($k_f$), the fraction of restricted protons ($F$) and relaxation times of the free protons ($T_1$, $T_2$) [3, 11]. For qMT imaging, a balanced steady state free precession (bSSFP) sequence sensitized to MT effects is used [18, 21] providing high-resolution whole brain qMT parameter maps within 10 minutes [36]. The efficacy of qMTI for characterization of benign and malignant brain tumors and metastases is analyzed.
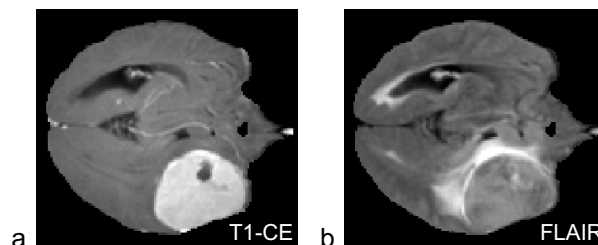


Figure 6.4: Patient with a meningeoma. (a) The axial $T_1$-CE image shows a well demarcated CE tumor in the temporal lobe of the left hemisphere, whereas (b) the axial FLAIR image illustrates the peritumoral edema.

### 6.2.2  Methods

Eleven healthy volunteers (mean age: 60, (7f, 4m)) were investigated on a clinical 1.5 T MR scanner (Avanto, Siemens Healthcare, Erlangen, Germany). Pathologies included 4 glioblastoma multiforme (GBM), 4 meningeomas and 3 metas-

tases. Besides qMT imaging, a conventional protocol was run, including DWI, $T_2$w, $T_1$w -/+ contrast enhancing (CE) sequences. A multislice (16 slices, 5 mm slice thickness) $B_1$ field map sequence was acquired for the assessment of flip angle deviations. Relaxation times of the free pool $T_1$ and $T_2$ were calculated from two spoiled gradient echo (SPGR) sequences (TR/TE = 9.8 ms/4.77 ms, bandwidth = 140 Hz/Pixel, $\alpha_1 = 3°$ and $\alpha_2 = 17°$) according to the DESPOT1 method and from two bSSFP sequences (TR = 4.55 ms, bandwidth = 790 Hz/Pixel, $\alpha_1$ = 15° and $\alpha_2 = 35°$) according to the DESPOT2 method [20]. The MT-bSSFP equation [21] was fitted pixelwise to a set of 8 bSSFP sequences ($\alpha = 35°$, bandwidth = 790 Hz/Pixel) with varying RF pulse durations TRF ($TR_1/T_{RF,1}$ = 2.68 ms/0.23 ms, ..., $TR_8/T_{RF,8}$ = 4.55 ms/2.1 ms) yielding $F$ and $k_f$ [36]. The qMT protocol was completed within 10 minutes, yielding images of the brain with 1.3 mm isotropic resolution. Evaluation of qMT data sets (MTR, $T_1$, $T_2$, $F$, $k_f$) with ROIs placed within the CE portion of the lesions (Fig. 6.4 a), the surrounding edema (Fig. 6.4 b) and the non-affected brain tissue of the contralateral hemisphere was performed using MATLAB (The MathWorks, Inc., Natick, MA, USA). Exemplary quantitative maps including a ROI for the CE-part of a menigeoma are displayed in Fig. 6.5.
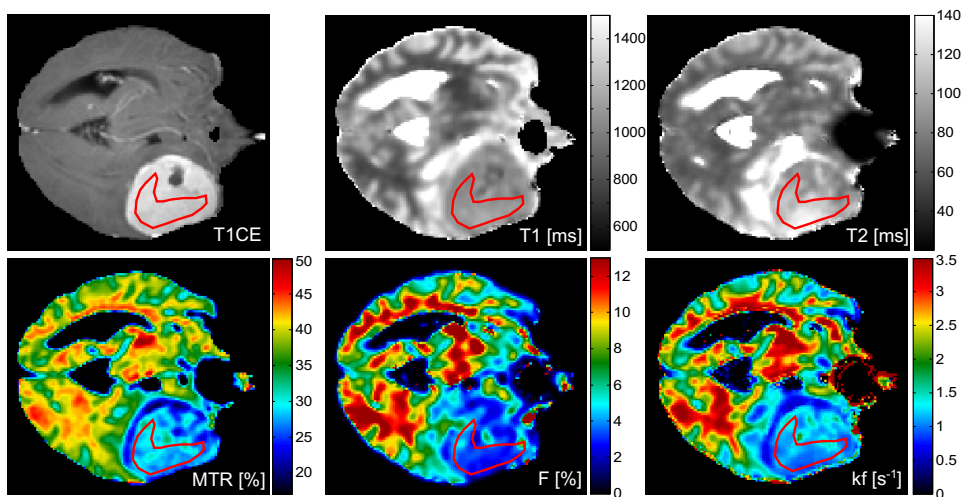


Figure 6.5: Exemplary hand-delineated region of interest placed in the CE-part of the meningeoma shown in Fig. 6.4. The Mean values for $T_1$, $T_2$, MTR, $F$, and $k_f$ within the ROI were calculated.

### 6.2.3 Results and Discussion

Mean MT parameter values for regions of interest (ROI) within different lesions and non-affected brain tissue are summarized in Table 6.2.

Table 6.2: MT parameter estimates (mean and standard deviation SD) within the contrast-enhancing area, the surrounding edema and the healthy appearing tissue for the different brain lesions investigated. Abbreviations: CE-port. = CE-portion, GBM = glioblastoma multiforme, Meni. = Meningeomas, Meta. = Metastases, Healthy t. = Healthy tissue.

| | | $T_1$ [ms] | $T_2$ [ms] | MTR [%] | $k_f$ [s$^{-1}$] | $F$ [%] |
|---|---|---|---|---|---|---|
| CE-port. | GBM | $1736 \pm 87$ | $141 \pm 14$ | $22.4 \pm 2.4$ | $0.6 \pm 0.1$ | $2.7 \pm 1.2$ |
| | Meni. | $1228 \pm 55$ | $110 \pm 9$ | $23.5 \pm 1.1$ | $1.2 \pm 0.6$ | $2.6 \pm 0.7$ |
| | Meta. | $1613 \pm 56$ | $135 \pm 7$ | $27.2 \pm 1.9$ | $0.8 \pm 0.1$ | $3.1 \pm 0.9$ |
| Edema | GBM | $1312 \pm 94$ | $157 \pm 14$ | $31.2 \pm 1.9$ | $1.0 \pm 0.4$ | $4.8 \pm 1.0$ |
| | Meni. | $1642 \pm 149$ | $206 \pm 18$ | $26.9 \pm 2.3$ | $0.8 \pm 0.3$ | $4.0 \pm 1.3$ |
| | Meta. | $1351 \pm 46$ | $123 \pm 7$ | $34.8 \pm 1.8$ | $1.3 \pm 0.2$ | $5.9 \pm 1.1$ |
| Healthy t. | GBM | $768 \pm 50$ | $63 \pm 6$ | $42.3 \pm 2.8$ | $3.5 \pm 0.4$ | $13.2 \pm 2.8$ |
| | Meni. | $889 \pm 112$ | $67 \pm 7$ | $41.3 \pm 3.5$ | $3.1 \pm 0.8$ | $11.7 \pm 3.3$ |

For damaged brain tissue, MTR is increased in normal appearing tissue (as compared to the non-affected contralateral side), whereas values for $F$ and $k_f$ are significantly lower and relaxation times significantly higher in tumors and metastases. Moreover, it is found that MTR-values are in general increased within the perifocal edema as compared to the CE-areas, whereas $F$ showed markedly increased values in the edema despite similar $k_f$. Several divergences are observed between different pathologies:

1. CE-areas: Maximal $F$ values are observed in metastases, whereas $k_f$ is maximal in meningeomas. $T_1$ and $T_2$ are decreased for meningeomas as compared to GBM and metastases.

2. Edema: Increased $k_f$ and $F$ values are found for metastases in comparison with the other lesions investigated, whereas $T_1$ and $T_2$ are increased for meningeomas as compared to GBM and metastases.

3. Despite similar MTR values for CE-areas in GBM and meningeomas, $k_f$ is twice as high with markedly lowered relaxation times in meningeomas as compared to GBM, regardless of similar $F$ values.

Differences in MT-values for the CE-regions and the surrounding edema in different brain pathologies might be attributed to differences in edema stages (acute vs. chronic) and edema intensity, possibly in combination with myelin loss. These changes might reflect the complexity of the damaged tissue between the different pathologies. Our results showed differences in qMT parameters despite similar MTR-values between GBM and meningeomas, indicating that MTR is less specific than assessment of quantitative parameters, as $F$ and $k_f$. This reflects the superiority of qMT-analysis providing quantitative information in comparison to the rather qualitative nature of MTR.

### 6.2.4 Conclusion

Magnetization transfer can provide tissue information not discernible on conventional MRI and might thus be a useful tool for the differentiation of brain pathologies. For brain tumors, contrast enhancing tissue and surrounding edema appear similar on conventional MRI and MTR images but show marked differences in $F$, $k_f$ and relaxation times. Quantitative MR imaging might thus substantially improve imaging specificity and might play an additive role for diagnostic evaluation of neurological conditions and for monitoring of treatment efficacy.

## 6.3 Quantitative Magnetization Transfer Imaging in Acute Stroke: A Follow Up Study Correlating Quantitative MRI with Respect of Severity of Stroke

### 6.3.1 Introduction

Magnetization transfer (MT) imaging can potentially serve as a marker for loss of tissue integrity [37]. Increased pathologic specificity is expected from quantitative MT imaging (qMTI) as compared to assessment of the semi-quantitative MT ratio (MTR). However, limited resolution or long acquisition times have so far impeded qMTI in severe acute stroke. Quantitative MTI applying balanced steady state free precession (bSSFP) sequences has overcome these problems [18, 21] and yields the bound pool fraction $F$, the exchange rate $k_f$, relaxation times of the free pool $T_1$ and $T_2$ in addition to the MTR. We present the results of two patients suffering from middle cerebral artery stroke with different progression of symptoms over three consecutive MRIs within the first 10 days.

### 6.3.2 Methods

Imaging was performed on a clinical $1.5\,\mathrm{T}$ Siemens Avanto scanner. Patient 1 (female, age 88y) and patient 2 (male, age 60y) underwent three consecutive cranial MRI exams: First MRI (MRI1) 6 h, second MRI (MRI2) 3-4 d and third MRI (MRI3) 9-10 d after symptoms' onset. The clinical protocol included DWI, $T_2$w, FLAIR, $T_2^*$w and TOF-MRA. Quantitative MTI included a $B_1$ map, two RF spoiled gradient echo sequences with variable flip angles for $T_1$ determination [20], 2 bSSFP sequences with variable flip angles for $T_2$ determination [20] and 7 bSSFP sequences using different RF pulse durations ($\mathrm{T_{RF}} = 230\,\mu\mathrm{s} - 2100\,\mu\mathrm{s}$) to yield $F$ and $k_f$ [36]. Data acquisition time for the whole qMTI protocol was 10 minutes. Images were registered spatially prior to data analysis using FSL (FSL Tool, Oxford, UK). A region of interest (ROI2, Fig. 6.6) of the diffusion restricted area and another ROI in the contralateral normal appearing parenchyma (ROI1, Fig. 6.6) were drawn manually in MRI1 of each patient. Mean values and standard deviations within the ROIs were calculated for each of the five quantitative parameters. Results from ROI1 were scaled relative to MRI1 (100%) to test reproducibility of the method. To illustrate progression of qMTI, values from ROI2 were scaled relative to values from ROI1 (100%) on the corresponding day.

### 6.3.3 Results

Figure 6.6 displays the DWI and exemplary maps of MTR, $F$ and $k_f$. Values from ROI1 for the first time point are given in Table 6.3.

---

This section has been presented as: F. Jax, M. Gloor, O. Bieri, M. Garcia, S. Engelter, F. Fluri, K. Scheffler, E.-W. Radue, and S. Wetzel. Quantitative Magnetization Transfer Imaging in Acute Stroke: A Follow Up Study Correlating Quantitative MRI with Respect of Severity of Stroke. Proceedings of the Joint Annual Meeting ISMRM-ESMRMB, Stockholm, 2010.
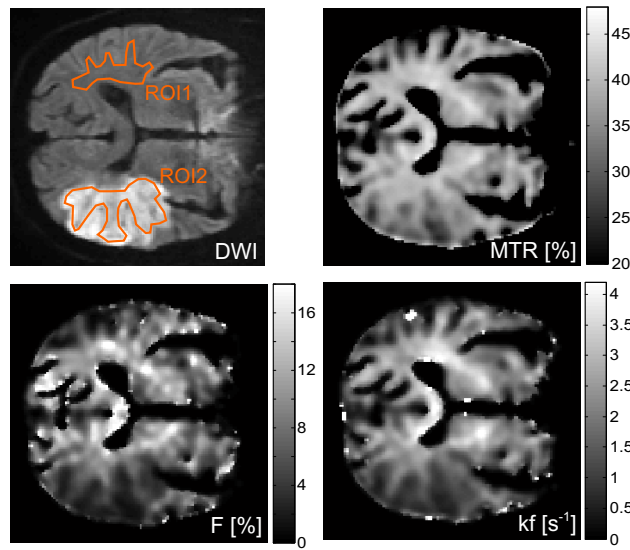
Figure 6.6: Exemplary DWI, MTR, $F$ and $k_f$ maps of patient 2. Regions of interest in contralateral normal appearing parenchyma (ROI1) and diffusion restricted region (ROI2) are marked on the DWI.

Table 6.3: Mean values and standard deviation of quantitative parameters in ROI1 for the first time point.

|        | $F$ [%]       | $k_f$[s$^{-1}$] | $T_1$ [ms]  | $T_2$ [ms] | MTR [%]        |
|--------|---------------|-----------------|-------------|------------|----------------|
| Pat.1  | $12.1 \pm 3.5$ | $2.9 \pm 0.4$   | $882 \pm 49$ | $72 \pm 5$ | $39.9 \pm 1.6$ |
| Pat.2  | $13.0 \pm 3.1$ | $3.2 \pm 0.5$   | $824 \pm 72$ | $67 \pm 7$ | $41.6 \pm 1.5$ |

Results in healthy appearing tissue remained constant over time (Fig. 6.7 a, c). In MRI1 both patients showed a pathologic increase in $T_1$ and $T_2$, a pathologic decrease in $F$ and $k_f$ and a minimal decrease in MTR (Fig. 6.7 b, d). For patient 1, who presented with worsening symptoms, an aggravation of qMTI values in MRI2 and MRI3 are observable (Fig. 6.7 b), while in patient 2, who was recovering, qMTI values showed a normalisation (Fig. 6.7 d). In contrast to the quantitative parameters, the MTR changed only slightly (80-100% relative to the contralateral hemisphere) and did not suggest different progressions in the two patients.

## 6.3.4   Discussion and Conclusion

Characterization of acute cerebral ischemia with respect of severity is of major clinical relevance. We present first qMTI results in cerebral ischemia based on a bSSFP protocol. Quantitative MT parameters might deliver advanced information about tissue integrity. They seem to be superior to simple MTR measurements and possibly allow for early statement of prognosis and efficacy of therapeutic methods.
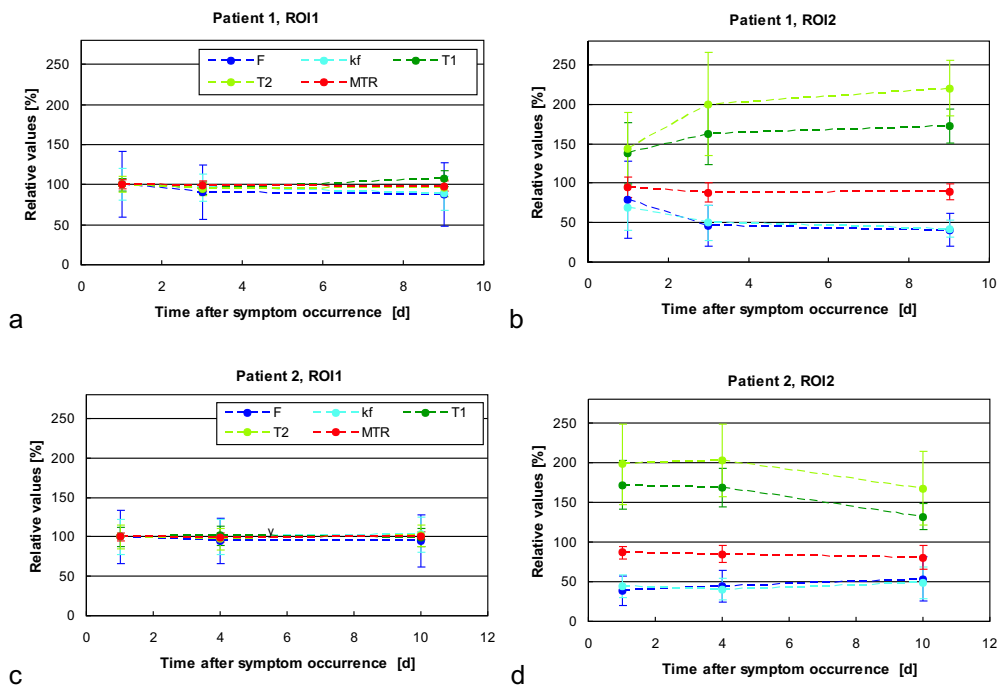
Figure 6.7: Mean values and standard deviation of quantitative parameters in ROI1 in relation to the first time point (100%) for patient 1 (a) and patient 2 (c). Values of ischemic tissue (ROI2) in relation to values of the contralateral hemisphere (100%) for the corresponding time point for patient 1 (b) and patient 2 (d).

# References

[1] M. Cercignani, M. R. Symms, K. Schmierer, P. A. Boulby, D. J. Tozer, M. Ron, P. S. Tofts, and G. J. Barker. Three-Dimensional Quantitative Magnetisation Transfer Imaging of the Human Brain. *Neuroimage*, 27(2): 436–41, 2005.

[2] R. M. Henkelman, X. Huang, Q. S. Xiang, G. J. Stanisz, S. D. Swanson, and M. J. Bronskill. Quantitative Interpretation of Magnetization Transfer. *Magn Reson Med*, 29(6):759–66, 1993.

[3] J. G. Sled and G. B. Pike. Quantitative Imaging of Magnetization Transfer Exchange and Relaxation Properties in Vivo Using MRI. *Magn Reson Med*, 46(5):923–31, 2001.

[4] S. D. Wolff and R. S. Balaban. Magnetization Transfer Contrast (MTC) and Tissue Water Proton Relaxation in Vivo. *Magn Reson Med*, 10(1):135–44, 1989.

[5] A. Okumura, K. Takenaka, Y. Nishimura, Y. Asano, N. Sakai, K. Kuwata, and S. Era. The Characterization of Human Brain Tumor Using Magnetization Transfer Technique in Magnetic Resonance Imaging. *Neurol Res*, 21 (3):250–4, 1999.

[6] F. Fazekas, S. Ropele, C. Enzinger, F. Gorani, A. Seewann, K. Petrovic, and R. Schmidt. MTI of White Matter Hyperintensities. *Brain*, 128(Pt 12): 2926–32, 2005.

[7] A. Ramani, C. Dalton, D. H. Miller, P. S. Tofts, and G. J. Barker. Precise Estimate of Fundamental in-Vivo MT Parameters in Human Brain in Clinically Feasible Times. *Magn Reson Imaging*, 20(10):721–31, 2002.

[8] D. Tozer, A. Ramani, G. J. Barker, G. R. Davies, D. H. Miller, and P. S. Tofts. Quantitative Magnetization Transfer Mapping of Bound Protons in Multiple Sclerosis. *Magn Reson Med*, 50(1):83–91, 2003.

[9] X. Ou and D. F. Gochberg. MT Effects and T1 Quantification in Single-Slice Spoiled Gradient Echo Imaging. *Magn Reson Med*, 59(4):835–45, 2008.

[10] P. Tofts. *Quantitative MRI of the Brain*. Wiley, 2003.

[11] J. G. Sled, I. Levesque, A. C. Santos, S. J. Francis, S. Narayanan, S. D. Brass, D. L. Arnold, and G. B. Pike. Regional Variations in Normal Brain Shown by Quantitative Magnetization Transfer Imaging. *Magn Reson Med*, 51(2):299–303, 2004.

[12] M. Filippi. Magnetization Transfer Imaging to Monitor the Evolution of Multiple Sclerosis. *Ital J Neurol Sci*, 20(5 Suppl):S232–40, 1999.

[13] V. L. Yarnykh and C. Yuan. Cross-Relaxation Imaging Reveals Detailed Anatomy of White Matter Fiber Tracts in the Human Brain. *Neuroimage*, 23(1):409–24, 2004.

[14] V. L. Yarnykh. Pulsed Z-Spectroscopic Imaging of Cross-Relaxation Parameters in Tissues for Human MRI: Theory and Clinical Applications. *Magn Reson Med*, 47(5):929–39, 2002.

[15] G. R. Davies, D. J. Tozer, M. Cercignani, A. Ramani, C. M. Dalton, A. J. Thompson, G. J. Barker, P. S. Tofts, and D. H. Miller. Estimation of the Macromolecular Proton Fraction and Bound Pool T2 in Multiple Sclerosis. *Mult Scler*, 10(6):607–13, 2004.

[16] D. F. Gochberg and J. C. Gore. Quantitative Magnetization Transfer Imaging Via Selective Inversion Recovery with Short Repetition Times. *Magn Reson Med*, 57(2):437–41, 2007.

[17] O. Bieri and K. Scheffler. On the Origin of Apparent Low Tissue Signals in Balanced SSFP. *Magn Reson Med*, 56(5):1067–74, 2006.

[18] O. Bieri and K. Scheffler. Optimized Balanced Steady-State Free Precession Magnetization Transfer Imaging. *Magn Reson Med*, 58(3):511–8, 2007.

[19] J. Homer and J.K. Roberts. Conditions for the Driven Equilibrium Single Pulse Observation of Spin-Lattice Relaxation Times. *J Magn Reson*, 74: 424–432, 1987.

[20] S. C. Deoni, T. M. Peters, and B. K. Rutt. High-Resolution T1 and T2 Mapping of the Brain in a Clinically Acceptable Time with DESPOT1 and DESPOT2. *Magn Reson Med*, 53(1):237–41, 2005.

[21] M. Gloor, K. Scheffler, and O. Bieri. Quantitative Magnetization Transfer Imaging Using Balanced SSFP. *Magn Reson Med*, 60(3):691–700, 2008.

[22] S. M. Smith, M. Jenkinson, M. W. Woolrich, C. F. Beckmann, T. E. Behrens, H. Johansen-Berg, P. R. Bannister, M. De Luca, I. Drobnjak, D. E. Flitney, R. K. Niazy, J. Saunders, J. Vickers, Y. Zhang, N. De Stefano, J. M. Brady, and P. M. Matthews. Advances in Functional and Structural MR Image Analysis and Implementation as FSL. *Neuroimage*, 23 Suppl 1:S208–19, 2004.

[23] R. W. Cox. AFNI: Software for Analysis and Visualization of Functional Magnetic Resonance Neuroimages. *Comput Biomed Res*, 29(3):162–73, 1996.

[24] G. J. Stanisz, E. E. Odrobina, J. Pun, M. Escaravage, S. J. Graham, M. J. Bronskill, and R. M. Henkelman. T1, T2 Relaxation and Magnetization Transfer in Tissue at 3T. *Magn Reson Med*, 54(3):507–12, 2005.

[25] A. MacKay, C. Laule, I. Vavasour, T. Bjarnason, S. Kolind, and B. Madler. Insights into Brain Microstructure from the T2 Distribution. *Magn Reson Imaging*, 24(4):515–25, 2006.

[26] C. Laule, I. M. Vavasour, S. H. Kolind, D. K. Li, T. L. Traboulsee, G. R. Moore, and A. L. MacKay. Magnetic Resonance Imaging of Myelin. *Neurotherapeutics*, 4(3):460–84, 2007.

[27] K. P. Whittall, A. L. MacKay, D. A. Graeb, R. A. Nugent, D. K. Li, and D. W. Paty. In Vivo Measurement of T2 Distributions and Water Contents in Normal Human Brain. *Magn Reson Med*, 37(1):34–43, 1997.

[28] J. Oh, E. T. Han, D. Pelletier, and S. J. Nelson. Measurement of in Vivo Multi-Component T2 Relaxation Times for Brain Tissue Using Multi-Slice T2 Prep at 1.5 and 3 T. *Magn Reson Imaging*, 24(1):33–43, 2006.

[29] S. M. Meyers, C. Laule, I. M. Vavasour, S. H. Kolind, B. Madler, R. Tam, A. L. Traboulsee, J. Lee, D. K. Li, and A. L. MacKay. Reproducibility of Myelin Water Fraction Analysis: A Comparison of Region of Interest and Voxel-Based Analysis Methods. *Magn Reson Imaging*, 27(8):1096–103, 2009.

[30] R. C. Mehta, G. B. Pike, and D. R. Enzmann. Magnetization Transfer MR of the Normal Adult Brain. *AJNR Am J Neuroradiol*, 16(10):2085–91, 1995.

[31] M. Garcia, M. Gloor, C. Stippich, F. Jax, K. Scheffler, and O. Bieri. Analysis of Brain Tumors and Metastases by Quantitative MT Imaging with BSSFP: Initial Experiences. *In: Proceedings of the 18th Annual Meeting of ISMRM, Stockholm, Sweden*, 2010.

[32] F. Jax, M. Gloor, O. Bieri, M. Garcia, S. Engelter, F. Fluri, K. Scheffler, E.-W. Radue, and S. G. Wetzel. Quantitative Magnetization Transfer Imaging in Acute Stroke: A Follow up Study Correlating Quantitative MRI with Respect of Severity of Stroke. *In: Proceedings of the 18th Annual Meeting of ISMRM, Stockholm, Sweden*, 2010.

[33] M. Filippi and M. A. Rocca. Magnetization Transfer Magnetic Resonance Imaging of the Brain, Spinal Cord, and Optic Nerve. *Neurotherapeutics*, 4 (3):401–13, 2007.

[34] M. H. Pui and Y. Wang. Diffusion and Magnetization Transfer MRI of Brain Infarct, Infection, and Tumor in Children. *Clin Imaging*, 29(3):162–71, 2005.

[35] R. I. Grossman, J. M. Gomori, K. N. Ramer, F. J. Lexa, and M. D. Schnall. Magnetization Transfer: Theory and Clinical Applications in Neuroradiology. *Radiographics*, 14(2):279–90, 1994.

[36] M. Gloor, K. Scheffler, and O. Bieri. Accelerated Quantitative Magnetization Transfer Imaging Using Balanced SSFP. *In: Proc 25th Meeting ESMRMB 2008, Valencia*, 2008.

[37] T. Tourdias, V. Dousset, I. Sibon, E. Pele, P. Menegon, J. Asselineau, C. Pachai, F. Rouanet, P. Robinson, G. Chene, and J. M. Orgogozo. Magnetization Transfer Imaging Shows Tissue Abnormalities in the Reversible Penumbra. *Stroke*, 38(12):3165–71, 2007.

# Chapter 7

# Summary and Outlook

Principally, magnetization transfer can be assessed in two ways. The first way is to describe the whole MT phenomenon by a single semi-quantitative value, the MTR. This can conventionally be done in less than 10 minutes, and the calculation is straightforward. Therefore, the method has been widely applied in various pathologies. Although MTR values clearly add information to diagnostic imaging, especially in multiple sclerosis patients, several potential issues have to be considered. Firstly, its contrast reflects a combination of sequence, relaxation, and MT parameters and may be difficult to interpret. Secondly, reproducibility of MTR using different scanners and sequences is not guaranteed. Proposed corrections add to the measuring and evaluation time.

The second way of MT assessment is quantitative MT imaging. Thereby, a whole series of data is measured in order to extract quantitative MT parameters from a multi-compartment model fit. Conventional MT-weighted SPGR methods require about 30-60 minutes scan time for high-resolution whole brain coverage. Furthermore, data analysis is rather complex. On the other hand, this approach yields unambiguous tissue parameters and allows for a more sensitive and specific assessment of biological changes, e. g. in multiple sclerosis, tumor, and ischemia patients.

## 7.1    Summary

The main goal of this thesis was to develop, evaluate, and apply MT imaging methods based on fast SSFP sequences. SSFP sequences benefit from an inherent MT sensitivity in addition to their short acquisition times and high SNR. So far, they have been used to acquire MTR maps by combining an MT weighted (short RF pulse and TR) and a non-MT weighted (long RF pulse and TR) image [1, 2]. From this starting point, the following questions were posed and corresponding answers were worked out in this thesis:

- **Chapter 2**: Is it possible to utilize the inherent MT sensitivity of balanced SSFP sequences for qMT imaging? Based on an underlying two-pool model, a bSSFP signal equation was derived to include the observed MT effects. Model parameters could then be derived by fitting this new equation to a series of bSSFP acquisitions with varying pulse durations and varying flip angles. Maps of the relaxation times, the pool size ratio, and the forward exchange rate were derived in human brain with a high isotropic resolution within 15 minutes. A correction for $B_1$-field inhomogeneities was done. Issues arising from the off-resonance sensitivity of bSSFP and from the absorption lineshape properties at on-resonance were discussed. Results corresponded well with literature values [3].

- **Chapter 3**: Are there ways to reduce acquisition time and to address banding artifacts and finite RF pulse effects in bSSFP-based qMT? It was shown that parameter estimation is also possible without sampling the flip angle dependency of the bSSFP signal curve [4]. The acquisition time can be reduced to 10 minutes by reducing the sampled points and adding a

$T_2$ measurement. This allows for a banding-artifact reduction by phase-cycled acquisition, which would not be possible for varied flip angles [5]. Furthermore, a slight modification of the two-pool bSSFP signal equation corrects effects from the assumption of instantaneous RF pulses [6].

- **Chapter 4**: Can qMT imaging also be adapted to nb-SSFP? Nonbalanced SSFP is not off-resonance sensitive and therefore well suited for targets with high susceptibility variations such as the musculoskeletal system. A new signal equation was derived describing the nb-SSFP signal with MT effects. Again, sampling of the signal curve at different pulse durations and flip angles enables a calculation of qMT parameters. This was demonstrated in vivo in human patellar cartilage and human femoral muscle. It is discussed how flow and motion sensitivity limit the applicability of this method [7].

- **Chapter 5**: How reproducible are MTR measurements with balanced SSFP? Simulations of the two-pool bSSFP signal equation predict a maximum and almost constant MTR value in the range of flip angles from 30° to 50°. In this range, $B_1$ sensitivity is expected to be very limited. In vivo measurements on nine healthy volunteers using two types of 1.5 T clinical systems were performed. Two volunteers were measured at 6 different sites. The results promise low variability of bSSFP-MTR for a protocol with an optimal flip angle. Whole brain MTR mapping is achieved within only 1:19 minutes [8].

- **Chapter 6**: Is it possible to apply bSSFP-MT imaging in a clinical setting? In a first step, a reference data set of normal appearing brain structures was analyzed. With this data set, regional variations in relaxation times and MT parameters were identified and compared to literature [9]. In a second step, bSSFP-based qMT imaging was applied in tumor [10] and ischemia [11] patients. Quantitative parameters revealed differences in various tumor regions, where no contrast is seen on conventional MRI and MTR images. In a time series of qMT acquisitions after cerebral stroke, qMT parameters showed pronounced variations, although MTR values remained almost constant.

In conclusion, new fast qMT methods were introduced and analyzed with the potential to be widely applicable in clinical research.

## 7.2 Outlook

- Extensive testing of bSSFP-based MT imaging [3] has already been done in brain tissue of healthy volunteers [9]. Therefore, the future work will be focused on establishing the methods proposed in this thesis in the **clinical environment**. First measurements in tumor [10] and stroke [11] patients show that fast MT imaging can be added to a routine protocol. Results suggest that MT provides tissue information not discernible on conventional MRI. To which extent diagnosis will benefit from the MT parameter maps

is still subject of research. Future studies address questions like whether early detection of pathologic tissue changes, better discrimination between differently affected tissue, and sensitive monitoring of treatment response is possible. Besides the ongoing investigations on tumor and stroke patients, another study with MS patients is planned.

- In the **musculoskeletal system**, the proposed techniques have not been tested that widely. MTR and qMT maps of cartilage have been acquired using nb-SSFP [7, 12]. Especially for qMT, problems occur from the strong motion sensitivity of nb-SSFP. Here, multiple bSSFP acquisitions with different RF phase increments to eliminate banding artifacts could be analyzed to yield optimal qMT and MTR images.

- Nonbalanced-SSFP high-resolution MTR maps of human patellar cartilage have been acquired at $3\,\text{T}$ and $7\,\text{T}$ [12]. If MT imaging with bSSFP is desired at **high field strengths**, issues will arise from the off-resonance sensitivity. An optimal recombination of phase-cycled images will have to be found for MTR (as demonstrated in Chapter 5) and for qMT imaging. An interesting application of high-field qMT using bSSFP could be the characterization of cartilage repair tissue.

- Magnetization in bSSFP imaging only reaches the steady-state after a certain transition period. An inversion recovery (IR) TrueFISP sequence, which combines the $\alpha/2$ pulse with an inversion pulse, has been proposed [13] and used for fast $T_1$ quantification [14]. The signal during the initial phase of an IR TrueFISP sequence shows a monoexponential behavior characterized by the apparent relaxation time $T_1^*$ depending on $T_1$, $T_2$, and the flip angle [15]. Analytical expressions were found to derive $T_1$, $T_2$, and spin density from this signal time course and measurements were performed in human brain [16]. It has recently been shown that the presence of **MT effects in IR TrueFISP** experiments with short RF pulses leads to considerable deviations in calculated $T_1$ and $T_2$ values [17, 18]. Here, short RF pulses saturate the magnetization of restricted pool protons. Subsequent exchange of these protons with liquid pool protons leads to a signal reduction. In future work, an analytical expression of the two-pool IR TrueFISP signal is aspired taking MT effects into account. This may enable derivation of qMT parameters from only two acquisitions, an IR TrueFISP with long and one with short RF pulses.

- Generally, SSFP-based MT imaging is based upon a modification of RF pulse durations and thus a modification of the RF pulse bandwidth. This modification enables the detection of bound protons not only via magnetization transfer, but also via chemical exchange. Via a variation of the pulse duration, the saturation of low concentration solute protons can be manipulated. An object of research is to find out whether the sensitivity of SSFP to this process is high enough or can be enhanced to perform **CEST imaging with SSFP** sequences.

# References

[1] O. Bieri and K. Scheffler. On the Origin of Apparent Low Tissue Signals in Balanced SSFP. *Magn Reson Med*, 56(5):1067–74, 2006.

[2] O. Bieri and K. Scheffler. Optimized Balanced Steady-State Free Precession Magnetization Transfer Imaging. *Magn Reson Med*, 58(3):511–8, 2007.

[3] M. Gloor, K. Scheffler, and O. Bieri. Quantitative Magnetization Transfer Imaging Using Balanced SSFP. *Magn Reson Med*, 60(3):691–700, 2008.

[4] M. Gloor, K. Scheffler, and O. Bieri. Quantitative Magnetization Transfer Imaging of the Brain within 10 Minutes. *In: Proceedings of the ISMRM White Matter Workshop, Krakow*, 2008.

[5] M. Gloor, K. Scheffler, and O. Bieri. Accelerated Quantitative Magnetization Transfer Imaging Using Balanced SSFP. *In: Proc 25th Meeting ESMRMB, Valencia*, 2008.

[6] M. Gloor, K. Scheffler, and O. Bieri. Finite RF Pulse Effects on Quantitative Magnetization Transfer Imaging Using Balanced SSFP. *In: Proceedings of the 18th Annual Meeting of ISMRM, Stockholm, Sweden*, 2010.

[7] M. Gloor, K. Scheffler, and O. Bieri. Nonbalanced SSFP-Based Quantitative Magnetization Transfer Imaging. *Magn Reson Med*, 64(1):149–56, 2010.

[8] M. Gloor, K. Scheffler, and O. Bieri. Intra- and Inter-Scanner Variability of Magnetization Transfer Ratio Using Balanced SSFP. *In: Proceedings of the 17th Annual Meeting of ISMRM, Honolulu, USA*, 2009.

[9] M. Garcia, M. Gloor, S. G. Wetzel, E. W. Radue, K. Scheffler, and O. Bieri. Characterization of Normal Appearing Brain Structures Using High-Resolution Quantitative Magnetization Transfer Steady-State Free Precession Imaging. *Neuroimage*, 52(2):532–7, 2010.

[10] M. Garcia, M. Gloor, C. Stippich, F. Jax, K. Scheffler, and O. Bieri. Analysis of Brain Tumors and Metastases by Quantitative Mt Imaging with BSSFP: Initial Experiences. *In: Proceedings of the 18th Annual Meeting of ISMRM, Stockholm, Sweden*, 2010.

[11] F. Jax, M. Gloor, O. Bieri, M. Garcia, S. Engelter, F. Fluri, K. Scheffler, E.-W. Radue, and S. G. Wetzel. Quantitative Magnetization Transfer Imaging in Acute Stroke: A Follow up Study Correlating Quantitative MRI with Respect of Severity of Stroke. *In: Proceedings of the 18th Annual Meeting of ISMRM, Stockholm, Sweden*, 2010.

[12] Oliver Bieri, Tallas C Mamisch, Siegfried Trattnig, and Klaus Scheffler. Steady state free precession magnetization transfer imaging. *Magn Reson Med*, 60(5):1261–1266, Nov 2008. doi: 10.1002/mrm.21781. URL http://dx.doi.org/10.1002/mrm.21781.

[13] M. Deimling and O. Heid. Magnetization Prepared True FISP Imaging. *In: Proc 2nd Annual Meeting ISMRM, San Francisco*, 1994.

[14] K. Scheffler and J. Hennig. T(1) Quantification with Inversion Recovery TrueFISP. *Magn Reson Med*, 45(4):720–3, 2001.

[15] K. Scheffler. On the Transient Phase of Balanced SSFP Sequences. *Magn Reson Med*, 49(4):781–3, 2003.

[16] P. Schmitt, M. A. Griswold, P. M. Jakob, M. Kotas, V. Gulani, M. Flentje, and A. Haase. Inversion Recovery TrueFISP: Quantification of T(1), T(2), and Spin Density. *Magn Reson Med*, 51(4):661–7, 2004.

[17] J.O. Blumhagen, F. Santini, O. Weber, K. Scheffler, and O. Bieri. Impact of Magnetization Transfer on Relaxometry Using Transient Steady-State Free Precession Imaging. *In: Proc 17th Annual Meeting ISMRM, Honolulu*, 2009.

[18] P. Ehses, V. Gulani, S. Yutzy, N. Seiberlich, P. M. Jakob, and M. A. Griswold. Single-Shot Proton Density, T1 and T2 Quantification with Radial IR TrueFISP: Effect of Magnetization Transfer and Long RF Pulses. *In: Proc 18th Annual Meeting ISMRM, Stockholm*, 2010.

# Acknowledgment

I would like to thank

...  my advisor Oliver Bieri, who supported me with countless discussions and inspiring ideas and always had time to answer my questions.

...  Klaus Scheffler for providing his knowledge and assistance and showing enthusiastic interest in my work.

...  my colleagues and friends from the Radiological Physics group in Basel, who created an animate working atmosphere discussing, talking, and drinking coffee and tea.

...  Meritxell Garcia and Felix Jax, whose enthusiasm to apply the new techniques on patients has been very motivating.

...  Stefan Ropele, Michaela Söllinger, and Christian Langkammer for the interesting collaboration and their hospitality during my stay in Graz.

...  everyone who has volunteered to be measured again and again.

...  the Swiss National Science Foundation for the financial support during this Thesis.

...  my family, especially my parents, and my friends, who have always supported me in what I do.

...  Jonas for being there for me at any time.

# Curriculum Vitae

## Personal Data

| | |
|---|---|
| Name | Monika Gloor |
| Date of Birth | 28 December 1981 |
| Place of Birth | Brugg, CH |

## Education

| | |
|---|---|
| Sept. 2007 - Sept. 2010 | Ph.D. Thesis, University of Basel. Supervisors: Dr. Oliver Bieri, Prof. Dr. Klaus Scheffler. Field: Biophysics. |
| Oct. 2005 - July 2007 | Master of Science in Physics, University of Basel. |
| Oct. 2001 - Sept. 2004 | Bachelor of Science in Physics, University of Basel. |
| Aug. 1997 - June 2001 | Grammar school (Kantonsschule), Aarau, CH. Mathematical-scientific orientation (Typus C). Diploma (Maturität) qualifying for university admittance. |

My academic teachers were Prof. B. Binggeli, Prof. C. Bruder, Prof. R. Buser, PD Dr. A. Bussmann-Holder, Prof. O. Gerhard, Dr. E. Kolbe, Prof. B. Krusche, Prof. E. Meyer, PD Dr. H. Mühry, PD Dr. T. Rauscher, Prof. C. Schönenberger, Prof. I. Sick, Prof. G. Tamman, Prof. L. Tauscher, Prof. F.-K. Thielmann, Prof. D. Trautmann in physics and astronomy, and Prof. C. Bandle, Prof. M. Grote, Prof. H.-C. Im Hof, Prof. H. Kraft, Dr. C. Luchsinger, Dr. H. Walser in mathematics.